Fluorescence studies of aldol catalysis and vapor plotting of chemically graded films

by

Judith Bautista Gomez

B.S., Park University, 2015

AN ABSTRACT OF A DISSERTATION

submitted in partial fulfillment of the requirements for the degree

DOCTOR OF PHILOSOPHY

Department of Chemistry
College of Arts and Sciences

KANSAS STATE UNIVERSITY
Manhattan, Kansas

2020

Abstract

Aldol reactions are the most versatile of organic reactions and are widely used synthetic routes to carbon-carbon bond formation via the coupling of ketones and aldehydes. The synthesis of pharmaceuticals, industrial feedstocks, commodity chemicals, and biomass-derived renewable liquid fuels frequently involve aldol reactions. These reactions are mainly catalyzed by strong bases (i.e. hydroxides), which are corrosive, not easily recovered, and not re-usable, leading to excess waste. Due to these difficulties, heterogeneous catalysts have gained interest among researchers in efforts to develop clean and economical processes. A better understanding of how the chemical and structural properties of heterogeneous catalysts lead to aldol product formation will enable their use in eco-friendly industrial processes.

This dissertation describes work directed towards an improved understanding of heterogeneous aldol reaction catalysts. As part of this work, the synthesis of a new Nile Red derivative incorporating a reactive aldehyde moiety (NR-Al) to follow aldol reactions is described. The dye was used to follow aldol reactions catalyzed by mesoporous and thin film materials. Ensemble and single molecule fluorescence spectroscopic methods were employed to characterize catalyst activity. The unique properties of NR-Al enabled, for the first time, preliminary studies of individual aldol reaction events occurring in real time at the single molecule level. The results presented in this dissertation will facilitate a broad range of both ensemble and single molecule spectroscopic investigations of heterogeneous catalysis in aldol reactions in the future.

The work in this dissertation involved three distinct studies.

In the first study, NR-Al was synthesized and characterized by High Performance Liquid Chromatography-Mass Spectrometry (HPLC-MS) and proton and carbon Nuclear Magnetic Resonance spectroscopy (^{1}H and ^{13}C NMR). The dye was employed to follow aldol reactions *in*

situ. A heterogeneous acid-base bifunctional catalyst of magnesium-zirconium-cesium supported on fumed silica (Mg-Zr-Cs/SiO_2) was employed, as was a strong base catalyst of magnesium-oxide (MgO); fumed silica (SiO_2) was employed as a control. Acetone and acetophenone were employed for crossed-aldol reactions with NR-Al at room temperature. The fluorescence spectral shifts observed from NR-Al during these reactions revealed whether each stopped at the alcohol addition product alone or instead formed both the aldol addition and olefin condensation products. Aldol product formation was verified by HPLC-MS and confirmed that the basic MgO catalyst only catalyzed primarily addition product formation, while the acid-base bifunctional catalyst, Mg-Zr-Cs/SiO_2, proceeded to olefin product formation. A mechanism that was based on the observed results and related literature was proposed to explain these observations. Olefin product formation in the case of Mg-Zr-Cs/SiO_2 was concluded to result from cooperativity between weak acid and base sites on the catalyst.

In the second study, NR-Al-doped catalyst films obtained by a sol-gel process using tetramethylorthosilicate (Mg-Zr-Cs/TMOS) were employed for aldol catalysis. Spectroscopic ellipsometry (SE) and X-ray Photoelectron Spectroscopy (XPS) were used to verify that a thin film was deposited, and that the active cesium component was well dispersed within the film. Widefield fluorescence microscopy and single molecule spectroscopy imaging and tracking methods were employed to show, for the first time, that NR-Al and the products of its aldol reactions with acetone and acetophenone are sufficiently fluorescent to be detected at the single molecule level. Preliminary studies showed that it may be possible to detect individual aldol reaction events from acetone vapor condensing and reacting with a NR-Al-doped catalyst film in real time.

In the third study, a direct-write method based on vapor phase plotting of organosilane precursors was developed and demonstrated. This method allowed for patterned uniform or gradient chemical films to be prepared over selected substrate regions, without modifying neighboring areas. Plotting parameters such as ambient relative humidity, chemical concentration, raster scanning speed, and capillary-substrate separation were all found to influence surface coverage and plotting resolution. The optimized plotting parameters were employed for initial demonstrations in which chemical pads and gradients were plotted using n-octyltrichlorosilane and 3-cyanopropyltrichlorosilane in separate experiments. The chemical pads and gradients were characterized by Water Contact Angle (WCA), SE, and by XPS. In this initial work, millimeter scale spatial resolution was achieved using glass capillaries with millimeter inner diameters. With certain modifications to the current system, this vapor phase plotting method can likely be used in the production of patterned coatings for biological, optical, and microelectronic devices, as well as in the preparation of catalysts for aldol reactions.

Fluorescence studies of aldol catalysis and vapor plotting of chemically graded films

by

Judith Bautista Gomez

B.S., Park University, 2015

A DISSERTATION

submitted in partial fulfillment of the requirements for the degree

DOCTOR OF PHILOSOPHY

Department of Chemistry
College of Arts and Sciences

KANSAS STATE UNIVERSITY
Manhattan, Kansas

2020

Approved by:

Major Professor
Dr. Daniel A. Higgins

Copyright

Abstract

Aldol reactions are the most versatile of organic reactions and are widely used synthetic routes to carbon-carbon bond formation via the coupling of ketones and aldehydes. The synthesis of pharmaceuticals, industrial feedstocks, commodity chemicals, and biomass-derived renewable liquid fuels frequently involve aldol reactions. These reactions are mainly catalyzed by strong bases (i.e. hydroxides), which are corrosive, not easily recovered, and not re-usable, leading to excess waste. Due to these difficulties, heterogeneous catalysts have gained interest among researchers in efforts to develop clean and economical processes. A better understanding of how the chemical and structural properties of heterogeneous catalysts lead to aldol product formation will enable their use in eco-friendly industrial processes.

This dissertation describes work directed towards an improved understanding of heterogeneous aldol reaction catalysts. As part of this work, the synthesis of a new Nile Red derivative incorporating a reactive aldehyde moiety (NR-Al) to follow aldol reactions is described. The dye was used to follow aldol reactions catalyzed by mesoporous and thin film materials. Ensemble and single molecule fluorescence spectroscopic methods were employed to characterize catalyst activity. The unique properties of NR-Al enabled, for the first time, preliminary studies of individual aldol reaction events occurring in real time at the single molecule level. The results presented in this dissertation will facilitate a broad range of both ensemble and single molecule spectroscopic investigations of heterogeneous catalysis in aldol reactions in the future.

The work in this dissertation involved three distinct studies.

In the first study, NR-Al was synthesized and characterized by High Performance Liquid Chromatography-Mass Spectrometry (HPLC-MS) and proton and carbon Nuclear Magnetic Resonance spectroscopy (^{1}H and ^{13}C NMR). The dye was employed to follow aldol reactions *in*

situ. A heterogeneous acid-base bifunctional catalyst of magnesium-zirconium-cesium supported on fumed silica (Mg-Zr-Cs/SiO_2) was employed, as was a strong base catalyst of magnesium-oxide (MgO); fumed silica (SiO_2) was employed as a control. Acetone and acetophenone were employed for crossed-aldol reactions with NR-Al at room temperature. The fluorescence spectral shifts observed from NR-Al during these reactions revealed whether each stopped at the alcohol addition product alone or instead formed both the aldol addition and olefin condensation products. Aldol product formation was verified by HPLC-MS and confirmed that the basic MgO catalyst only catalyzed primarily addition product formation, while the acid-base bifunctional catalyst, Mg-Zr-Cs/SiO_2, proceeded to olefin product formation. A mechanism that was based on the observed results and related literature was proposed to explain these observations. Olefin product formation in the case of Mg-Zr-Cs/SiO_2 was concluded to result from cooperativity between weak acid and base sites on the catalyst.

In the second study, NR-Al-doped catalyst films obtained by a sol-gel process using tetramethylorthosilicate (Mg-Zr-Cs/TMOS) were employed for aldol catalysis. Spectroscopic ellipsometry (SE) and X-ray Photoelectron Spectroscopy (XPS) were used to verify that a thin film was deposited, and that the active cesium component was well dispersed within the film. Widefield fluorescence microscopy and single molecule spectroscopy imaging and tracking methods were employed to show, for the first time, that NR-Al and the products of its aldol reactions with acetone and acetophenone are sufficiently fluorescent to be detected at the single molecule level. Preliminary studies showed that it may be possible to detect individual aldol reaction events from acetone vapor condensing and reacting with a NR-Al-doped catalyst film in real time.

In the third study, a direct-write method based on vapor phase plotting of organosilane precursors was developed and demonstrated. This method allowed for patterned uniform or gradient chemical films to be prepared over selected substrate regions, without modifying neighboring areas. Plotting parameters such as ambient relative humidity, chemical concentration, raster scanning speed, and capillary-substrate separation were all found to influence surface coverage and plotting resolution. The optimized plotting parameters were employed for initial demonstrations in which chemical pads and gradients were plotted using n-octyltrichlorosilane and 3-cyanopropyltrichlorosilane in separate experiments. The chemical pads and gradients were characterized by Water Contact Angle (WCA), SE, and by XPS. In this initial work, millimeter scale spatial resolution was achieved using glass capillaries with millimeter inner diameters. With certain modifications to the current system, this vapor phase plotting method can likely be used in the production of patterned coatings for biological, optical, and microelectronic devices, as well as in the preparation of catalysts for aldol reactions.

Table of Contents

List of Figures

List of Tables

Acknowledgements

I would like to thank my major advisor, Dr. Daniel Higgins for all his support during my graduate studies. I especially thank him for opening the door to his lab in Summer 2015 so that my curious mind could think about real-world issues and how to employ research to contribute new understanding to the scientific field. I am grateful for his continuing guidance throughout my 5 years of PhD studies, for challenging me with a variety of projects, for revising my seminar papers, pre-liminary examination, manuscripts and this dissertation, and finally, for his great mentorship and encouragement.

I would also like to thank the collaborators involved in the projects presented in this dissertation. Thank you, Dr. Keith Hohn, Dr. Stefan Bossmann, Dr. Ryan Rafferty, and Dr. Maryanne Collinson, for sharing your scientific expertise and suggestions on my research work. I thank Dr. Keith Hohn, Dr. Stefan Bossmann, and Dr. Christopher Culbertson for serving in my supervisory committee and I thank Dr. Brian Lubbers for being the chairperson for my final PhD examination.

I would like to acknowledge the staff in the Chemistry department at K-State, Ron Jackson, Tobe Eggers, and Jim Hodgson for designing and troubleshooting critical components needed in my studies. I also acknowledge the research funding support from National Science Foundation that allowed me to spend more time thinking about my projects and developing new experiments.

I am thankful for the collaborators that helped me with various parts of my research. Dr. Man Zhang is thanked for proposing an initial reaction mechanism to synthesize the dye employed in my first two projects. Abdulhafiz Usman is thanked for synthesizing one of the catalysts employed in my first project and for doing most of the catalyst characterization. Dr. Anna Forzano is thanked for taking XPS measurements of the chemical gradients prepared in my third project. I

also thank my former lab mates, Dr. Dipak Giri, Dr. Hao Xu, Dr. Zi Li, and Dr. Ruwandi Kumarasinghe for valuable academic and friendly discussions. I especially thank Dr. Li for helping me learn and troubleshoot various components of the widefield microscope.

I would also like to thank my former Park University research advisor and mentor, Dr. Gregory Claycomb – former wildcat, for first introducing me to research. I thank him for his valuable advice and for encouraging me to go to graduate school. I am sincerely grateful that he took the time to drive me to Manhattan, KS 5 years ago and gave me a tour around the Little Apple and around K-State while sharing his graduate experience. I would not have made it this far without his encouragement.

Finally, I thank my loving family for encouraging me throughout the ups and downs in my graduate studies and keeping me accountable to reach the finish line. I thank my loving parents Jose Bautista and Judith Gomez. I also thank my brothers and sisters Julio, Antonio, Jesica, and Julie for the great memories growing up.

Dedication

This work is dedicated to my Mami Judith Gomez for always believing in me. For making sure I kept up with my academics and for pushing me to study math and science, especially during the summers growing up when I just wanted to explore outdoors with my siblings and friends. For holding me to high standards because she knew my academic abilities. I also thank her for understanding when I was busy with academic work and studying for exams and for not piling on me other obligations. I especially thank her for raising me to be the strong woman I am today.

I also dedicate this work to my seven-year old sister, Julie. This is proof that you can accomplish whatever you set your mind to. I hope that this can encourage you to reach for the stars.

Preface

"Science means constantly walking a tightrope between blind faith and curiosity;

Between expertise and creativity;

Between bias and openness;

Between experience and epiphany;

Between ambition and passion;

Between arrogance and conviction;

--- In short,

Between an old today and a new tomorrow."

- Henrich Rohrer

Acronyms and Definitions

NH_3	ammonia
BJH	Barrett, Joyner, Halenda theory
BET	Brunauer, Emmet, Teller theory
$Ca(OH)_2$	calcium hydroxide
CO_2	carbon dioxide
^{13}C NMR	carbon-13 nuclear magnetic resonance spectroscopy
Cs	cesium
CCD	charged-coupled device camera
C.I.	confidence interval
DNA	deoxyribonucleic acid
DMF	dimethyl formamide
DMSO	dimethyl sulfoxide
E	emission ratio
EDS	energy dispersive x-ray spectroscopy
EI-MS	electron ionization mass spectrometry
ESI-MS	electrospray ionization mass spectrometry
SiO_2	fumed silica
HPLC	high performance liquid chromatography
HPLC-MS	high performance liquid chromatography-mass spectrometry
ICP-OES	inductively coupled plasma-optical emission spectroscopy
LAH	lithium aluminum hydride
Mg	magnesium

MgO	magnesium oxide
Mg-Zr-Cs/SiO_2	magnesium-zirconium-cesium/fumed silica
Mg-Zr-Cs/TMOS	magnesium-zirconium-cesium/tetramethylorthosilicate
MeOH	methanol
NR	nile red
NR-Al	nile red aldehyde
NA	numerical aperture
Navg	numerical average
OLED	organic light emitting diode
OTFT	organic thin film transistor
^{1}H NMR	proton-1 nuclear magnetic resonance spectroscopy
PCC	pyridinium chlorochromate
RH	relative humidity
SBA-15	Santa Barbara amorphous silica-15
SEM	scanning electron microscopy
SAM	self-assembled monolayer
SMS	single molecule spectroscopy
SMT	single molecule tracking
NaOH	sodium hydroxide
SE	spectroscopic ellipsometry
SA	surface area
TPD	temperature programmed desorption
TBAOH	tetrabutylammonium hydroxide

THF	tetrahydrofuran
TEM	transmission electron microscopy
2D	two-dimensional
WCA	water contact angle
XRD	x-ray diffraction
XPS	x-ray photoelectron spectroscopy
Zr	zirconium

Chapter 1 - Introduction

1.1 Aldol Reactions

The aldol reaction was introduced by Charles Wurtz, who first prepared the β-hydroxy aldehyde from acetaldehyde in 1872.[1] Aldol reactions are among the most versatile of organic reactions,[2] with over 240,000 entries in SciFinder. These reactions employ two carbonyl compounds that act as an electrophile and as a nucleophile. The reactions may employ two ketones, two aldehydes, or in the case of a crossed-aldol reaction, the reactants are typically an aldehyde and a ketone. The reaction of these active species, with the aid of a catalyst, results in the formation of a carbon-carbon single bond (aldol addition product/alcohol), or upon condensation, a carbon-carbon double bond (aldol condensation product/ α,β-unsaturated ketone),[2] **Figure 1.1** shows the products of a crossed-aldol reaction between acetone and benzaldehyde. The self-condensation of acetone is minimized because the aldehyde is a better electrophile than the ketone.[2]

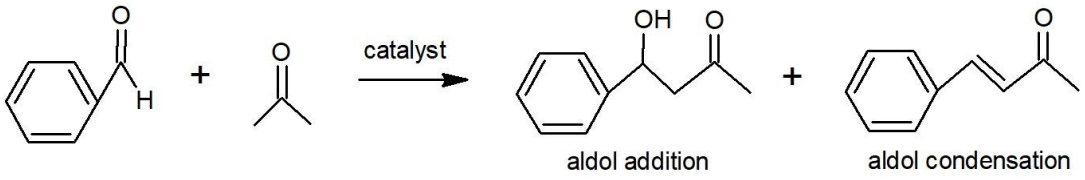

Figure 1.1 Aldol reaction between acetone and benzaldehyde in the presence of a catalyst.

There are many variants, including the Claisen, Diekmann, Henry, Knoevenagel, and Guerbert condensations.[2] Aldol reactions and their variants are the backbone of organic synthesis because of their ability to construct larger molecules from smaller ones,[3-6] or to effect cyclization.[7, 8] They are also common in biology, where aldolase, citrate synthase, and other enzymes catalyze aldol reactions in the metabolism.[9] For example, the citric acid cycle (Kreb's cycle) begins with

an aldol reaction catalyzed by aldolase where acetyl coenzyme A (CoA) condenses with oxaloacetate to produce Citryl CoA. Subsequent hydrolysis of Citryl CoA drives the synthesis of citrate, which is part of a series of chemical reactions within aerobic organisms to produce energy from carbohydrates, fats and proteins.[10] In glucogenesis (i.e. sugar-building) biochemical pathway, glyceraldehyde-3-phosphate (GAP) and dihydroxyacetone phosphate (DHAP) condense together to form fructose 1,6-bisphosphate via an aldol reaction.[11] The cleavage of the 1,6 phosphate diester of fructose in glycolysis (sugar-burning) pathway occurs by retro-aldol reaction.[12] In addition, the condensation products (i.e. chalcones) of aldol reactions have many medicinal and pharmaceutical properties that make them excellent template molecules for antimicrobials, anti-inflammatories, antibacterial, and potential anti-cancer drugs.[13] Aldol reactions are also utilized for the synthesis of fine chemicals used in the production of industrial feedstocks, commodity chemicals, and biomass-derived renewable liquid fuels.[14-16] For example, a common industrial process involves the synthesis of α, β-ionone from the reaction of citral and acetone. The α-ionone is used as an aromatic component in fragrances while β-ionone is employed for the synthesis of vitamin A.[17] Jasminaldehyde is also a traditional product used in fragrances as it provides a violet-like scent. It is formed by the aldol condensation of heptanal with benzaldehyde.[18] The chromophores of aromatic aldols such as δ-damascone and propiophenones have also been studied as they can be tuned to selectively release a desired fragrance over time.[19] Other aldol reactions employed in industry include those of 2-ethyl-hexanol, acetone and Guerbert alcohols. The aldol product (2-ethyl-hexanol) from condensation of butanal is used to synthesize di-ethylhexyphthalate, which is used as a plasticizer for PVC. The self-condensation product of acetone (mesityl oxide) is used for the synthesis of methyl isobutyl ketone (MIBK), which is widely used as a solvent of cellulose and resin-based coatings to make paper, plastics, and paints. Guerbert alcohols are oxidized to

aldehyde products that self-condense to form aldol products that are used to make primary dimer alcohols, which are used in cosmetics and textiles, and as lubricants and surfactants.[15]

Aldol reactions can be base catalyzed, or acid catalyzed; activation of the reactive molecules occurs by a different mechanism in each case, as shown in **Figure 1.2**. The base catalyzed aldol reaction occurs is 5 steps **(A)**: the base deprotonates the carbonyl group at the α position to form an enolate (1), the enolate serves as a nucleophile and attacks an aldehyde to form a carbon-carbon bond (2), the resulting alkoxide ion is equilibrated by protonation (3) to form the aldol addition product, the elimination of water proceeds by a second enolization (4), and hydroxide elimination to form a carbon-carbon double bond (5).[2] The acid catalyzed aldol reaction occurs in 5 steps **(B)**: the acid activates the carbonyl carbon by donating a proton (1), the conjugate base of the acid deprotonates the carbonyl group at the α position to form an enol (2), the enol attacks the carbonyl group of the first intermediate (3), the carbocation formed is stabilized by deprotonation (4), followed by the loss of water (5).[2] Although the elimination step (5) seems somewhat unlikely, given that the conditions are slightly acidic, and water is not a great base, this elimination mechanism is generally accepted for simplicity.[20, 21]

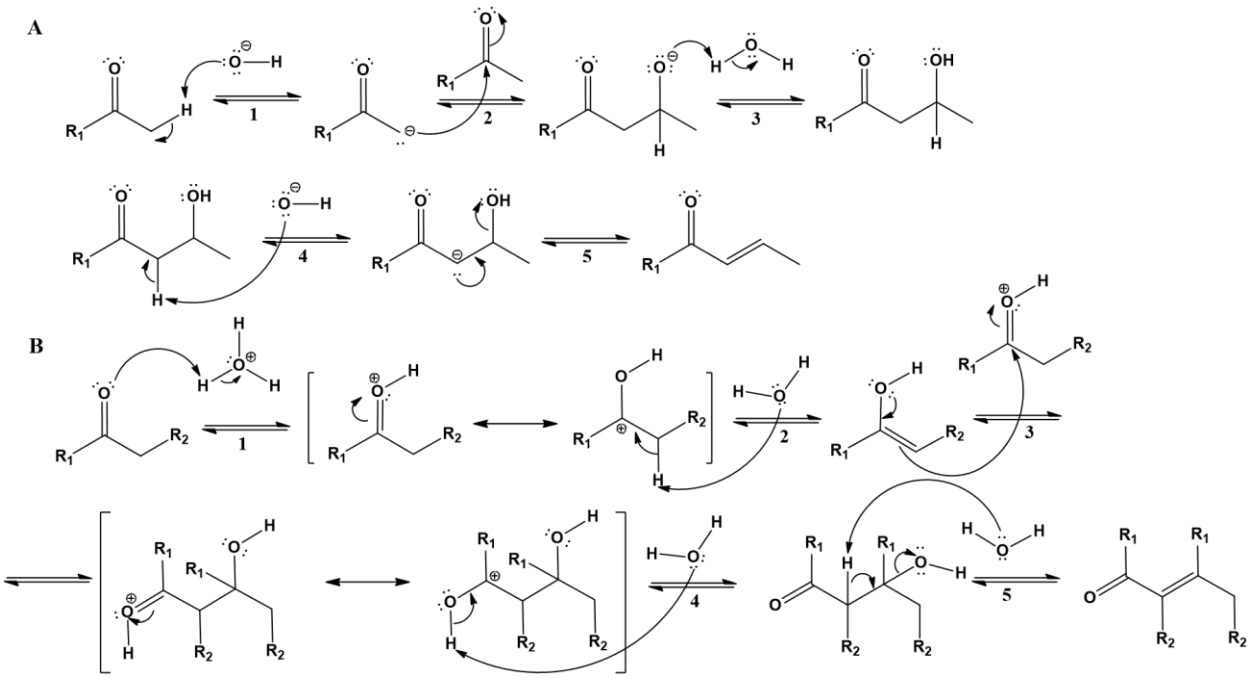

Figure 1.2 Base catalyzed **(A)**, and acid catalyzed **(B)** aldol condensation reactions.[2]

Aldol reactions are most often catalyzed by homogenous catalysts comprising aqueous hydroxide solutions.[15] In fact, it has been estimated that over 1.5 million tons of the chemicals produced worldwide from aldol reactions and their derivatives employ homogenous NaOH and $Ca(OH)_2$ catalysts.[22] These homogenous catalysts are corrosive, not easily removed from the reaction mixture and are not re-usable, producing excess waste and increasing capital cost. The Research Triangle Institute estimated that 30% of the selling price of the products of industrial condensation reactions is due to the need for purification, recovery and waste management; for every 10 tons of product formed, 1 ton of homogenous hydroxide-based catalyst were spent.[23] Due to these difficulties, heterogeneous catalysts have gained interest among researchers in efforts to develop clean and economical processes.[24] Another advantage of using heterogeneous catalysts is that the surface of the catalyst support (i.e. amorphous and mesoporous silica) can be tunable with different active sites to enhance its catalytic activity.[25, 26] Furthermore, various pore sizes

introduced by the silica support have enabled structure-dependent product formation.[27-29] For example, a nitrogen substituted silicon-alumina catalyst (Nit-NaY) with 7.2 Å pore size was employed for selectivity towards monomer product in the reaction of furfural with acetone. The pore size was big enough to accommodate the monomer product but too small to allow rapid diffusion of the dimer product. The monomer product is used in production of wood-polymer composites while the dimer product is key in biorefinery to produce diesel and jet fuel.[30]

There are several reports of liquid-phase organic reactions catalyzed by inorganic solid catalysts.[31-33] Izumi et al. reported that CaO and MgO catalyzed the regio- and chemo-selective ring opening of epoxides with cyanotrimethylsilane at room temperature much more efficiently than homogenous catalysts.[32] Zhang et al. reported the aldol reaction of acetone on several alkaline earth oxides at 0°C and found that the base-catalyzed reaction was more efficiently promoted on stronger basic sites, with BaO being the better promoter. They also found that a small amount of pre-adsorbed water (0.12 mmol per 50 mg catalyst) increased the activity and selectivity to diacetone alcohol when MgO was employed and proposed that the basic OH^- ions retained on the catalyst surface or formed by dehydration of diacetone alcohol are the active sites for aldol addition.[31] Furthermore, Corma and Iborra reviewed recent work towards the optimization of alkali metals and alkaline earth metal oxides for catalysis of a variety of organic transformations including isomerization, carbon-carbon and carbon-oxygen bond formations, and hydrogen transfer reactions.[33]

Regarding aldol reactions, it has also been reported that there exists a cooperative effect between the acidic and basic sites of bifunctional silica-based catalysts for the enhanced conversion of aldol products compared to their individual catalytic sites.[25, 26, 34-36] For example, Zeidan et al. synthesized a SBA-15 support incorporating sulfonic acid and primary amine for the

aldol reaction of acetone with 4-nitrobenzaldehyde. The activity of the catalyst was 1.5 times higher than either of the components alone.[37, 38] Lewis et al. employed transition metals on silica supports for crossed aldol reactions of aromatic aldehydes with acetone. It was found that acid-base pairs in the silicon-oxide-metal framework promoted soft enolization through α-proton abstraction, and that the catalysts maintained catalytic activity in the presence of as much as 10 wt.% water.[39] Yadav and Aduri employed a Mg-Al mixed oxide supported on mesoporous silica for the production of jasminaldehyde. The fresh catalyst was 86% selective to jasminaldehyde after a 4 h reaction and 82% after the second regeneration of the catalyst by heat treatment.[40] Yan et al. employed cesium (Cs) supported SBA-15 catalysts for the preparation of methyl acrylate. A catalyst loading of 5 wt.% Cs achieved the highest conversion and selectivity for methyl acrylate, ~50% and 95% respectively.[41] The catalyst was regenerated 9 times with no loss in catalytic activity, which the authors attributed to the suitable strength of weak-acid-base properties rooted in the Si-O-Cs species on the surface of the silica support.[41] Li et al. presented a more thorough study of Cs-supported SBA-15 catalysts with zirconium (Zr) and iron (Fe) surface modifiers, where a combination of the three metals Zr-Fe-Cs on the SBA-15 support improved the selectivity for methyl methacrylate by 12% compared to the Cs-SBA-15 alone.[42] The enhanced selectivity was attributed to the increase in Bronsted-acid sites from the Fe-silicate structure,[43] which led to the facilitation of the aldol reaction by cooperative effects between the Bronsted-acid sites and base sites[44] as well as the retardation of surface area loss due to zirconium.[45]

The above studies have shown the promise of heterogeneous catalysts for carrying out aldol reactions. Gaining a further understanding of how the chemical and structural properties of heterogeneous catalysts lead to aldol product formation will enable their use to drive eco-friendly industrial processes. In this dissertation, fluorescence-based methods were employed to follow

aldol reactions to get important initial catalyst activity by employing a fluorescence sensitive molecular probe.

1.2 Fluorogenic Molecular Probes for Aldol Catalysis

Fluorogenic molecules that afford fluorescent products have been widely employed to monitor the progress of chemical reactions.[46-48] This is typically achieved by ensemble fluorescence measurements where a growth in fluorescence occurs as the reaction proceeds *in situ*. Fluorogenic probes are widely used in high-throughput screening and rapid characterization of catalysts at the ensemble level.[49-51] When highly fluorescent reactants and products are involved, the process can be followed at the single molecule/ single turnover level. For example, Kumar et al. employed the acid catalyzed oligomerization of furfuryl alcohol to probe the catalytic activity of mesoporous alumina-silica catalysts with varying surface defects.[52] Later, Ristanovic et al. showed that different product intermediates are formed in the surface defects of alumina-silica catalysts by employing the acid catalyzed oligomerization of styrene, which produces several carbocationic species.[53] Recently, researchers in the Weckhuysen group employed the localized fluorescence emission of the products formed from the acid catalyzed oligomerization of thiophene to map the catalytic activity of industrially important catalyst particles in real time.[54]

As mentioned above, aldol reactions are important carbon-carbon bond forming reactions in synthetic organic chemistry.[21] Even though these reactions are widely used in industrial settings, factors about how the catalyst employed affects catalysis of aldol reactions have not yet been completely elucidated. Since the focus of this dissertation are heterogeneous catalysts, only methods to study their catalytic properties will be considered. The acidic and basic properties of the catalyst can be assessed *ex situ* via solid-state NMR,[55] X-ray absorption spectroscopy,[56]

temperature-programmed desorption, and infra-red spectroscopy of numerous probe molecules.[57] However, these approaches give little information about the *in situ* acidic and basic properties of the catalyst, which are certain to change depending on the solvent employed and the temperature at which the reaction is run. Therefore, new approaches that allow for better screening of catalyst activity are important for the development of aldol catalysts. As discussed above, single molecule spectroscopy (SMS) can be a valuable method to elucidating the activity of the catalyst. In order to employ SMS methods in the investigations of aldol reactions, it is imperative that a reactive fluorescent dye be used.

Although fluorogenic probes are now used to follow aldol reactions at the ensemble level,[58-60] no studies have been reported at the single molecule level, to date. The lack of single molecule studies may be due to the absence of suitable dyes designed to undergo aldol reactions while also remaining sufficiently fluorescent for detection at the single molecule level. In this regard, a highly fluorescent dye, Nile Red (NR) promises to solve this challenge as it has been previously employed in numerous single molecule detection, spectroscopy, and tracking studies. For example, Bongiovanni et al. employed NR to simultaneously record its spatial position and emission spectrum to super-resolve biological structures.[61] The Higgins group has extensively employed NR to characterize the properties and dynamics of thin film materials derived from sol-gel deposition. Their studies have taken advantage of the solvatochromic properties of NR[62] to measure the polarity of micro-environments in various materials including in plasmid DNA,[63] and one-dimensional organosilane chemical gradients.[64] They have also studied the diffusion of NR within organically modified silicate films to show that film heterogeneity occurs on sub-100-nm length scales and likely results from the presence of inorganic-rich and organic-rich domains.[65] Later, they employed silica thin film gradients to show, for the first time, that two subpopulations

of mobile and immobile NR molecules reside on the gradient and silica sublayer respectively, showing the importance of surface heterogeneity for stationary phase gradients and combinatorial systems.[66]

In this dissertation, the synthesis and use of a new derivative of Nile Red, incorporating a reactive aldehyde moiety (NR-Al) is reported. The NR-Al probe is employed in solution-phase ensemble and single molecule spectroscopic studies of the heterogeneous catalysis of crossed aldol reactions. These studies are the first in the literature to employ a NR derivative as a molecular probe for aldol reactions.

1.3 Chemically Graded/Patterned Films

Chemically graded films incorporate small regions modified by different functional groups or by mixtures of different functional groups. They exhibit a continuous, gradual change in the chemical properties along the gradient.[67-70] The need for combinatorial systems that speed experimental throughput, by incorporating different analytes is manifested in various research areas ranging from materials science to biology. For example, Inagi employed gradient polymer surfaces to run chemical reactions of the conducting polymers on a bipolar electrode.[71] Jayaraman et al. employed a platinum catalyst gradient on an indium-tin-oxide substrate for electro-oxidation reactions relevant to the fuel cell anode.[72] Furthermore, Fasolka et al. reported on combinatorial gradient library approaches to assess the mechanical properties and adhesion of surfaces, interfaces and films.[73]

The Collinson and Higgins groups employed stationary phase gradients for the chemical separation of over the counter drugs[74] and water and fat-soluble vitamins.[75] Chemical gradients have also been used to drive the motions of cells.[76, 77] Elwing et al. employed a wettability gradient

to study the molecule-surface interactions of human fibrinogen, γ-globulin, and lysozyme on silicon plates.[76] Giri et al. also employed organosilane based wettability gradients to elongate and align double stranded λ-DNA for potential applications in DNA barcoding and studies of DNA-protein interations.[77] Later, Li et al. employed an aminosilane gradient surface to probe the local dielectric constant of plasmid DNA in different microenvironments. The researchers showed how the dielectric constant within double stranded DNA is impacted by changes in the solution ionic strength, providing new knowledge on an important parameter that affects DNA interactions with other proteins, drugs, and surfaces.[63] Surface chemical gradients are also being explored for tissue engineering applications. For example, Smith et al. studied the migration of human microvascular endothelial cells on fibronectin gradients with different slopes.[78] Furthermore, new strategies for incorporating graded physical and chemical gradients are being explored with the promise to regenerate heterogeneous tissues and tissue interfaces.[79]

Top-down and bottom-up material fabrication approaches are common methods employed in the production of chemical gradients. In top-down approaches, different lithography methods are employed to generate the pattern/shape of the gradient on a pre-coated substrate material. The substrate is then chemically etched[80] or exposed to a UV-plasma[81] to render the final pattern on the surface. In bottom-up approaches, chemical precursors (i.e. monomers, oligomers, polymers) are gradually deposited on the substrate surface from the vapor phase or from the liquid phase (controlled rate immersion, inkjet printing). Natural diffusion in the vapor phase was first employed to make a chemical gradient by Chaudhary et al.[82] These researchers showed that gradients can be readily made by simply exposing the substrate (i.e. silicon wafer) to a reservoir containing the chemical precursors (i.e. organochlorosilanes). The chemical gradient is generated in < 10 min by placing the substrate 2 mm from the reservoir and allowing the silane vapor to

diffuse in a directional manner from the substrate side near the reservoir towards the opposite edge. In this way, the edge closest to the reservoir is covered with the highest density of the organic modifier. Chemical modification gradually decreases across the substrate (to the opposite edge).[82] Later, researchers employed a contact printing technique using elastomeric stamps to deposit octadecyltrichlorosilane by varying the time of contact on the substrate. With this approach they were able to generate micrometer-scale chemical gradients with a gradient steepness 1-3 orders of magnitude higher than the traditional vapor diffusion method.[83] In a more sophisticated method, commercial ink-jet printers were employed to deposit alkanethiols onto gold substrates to create binary chemical gradients and patterns of tertiary functionality.[84]

While photolithography[85] and contact printing[83] afford control over the gradient profile and can be used to make patterned films, changing the gradient characteristics or film pattern requires the fabrication of a new mask or stamp. Although both dip-coating[86-88] and controlled-rate infusion[89, 90] methods allow the gradient profile to be manipulated, neither allows for the deposition of patterned films. Ink jet printing[84] is a direct-write method that provides the flexibility required to produce gradients of arbitrary shape, location, and profile, but it requires careful optimization of the ink properties (e.g., surface tension, viscosity and solvent volatility) to achieve proper jetting.[91, 92] Furthermore, the printing of reactive materials by ink jet methods frequently leads to clogging of the print nozzles. Since ink jet printing relies on the deposition of liquid droplets on solid surfaces, de-wetting of the substrate and de-mixing of the ink solutions can also be problematic. As an alternative to these methods, the work in this dissertation focused on the development of vapor phase plotting of organosilanes for making patterned and chemically graded self-assembled (SAM gradient) films. This method has the potential to plot organic acid-base bifunctional catalyst thin films for catalysis studies of aldol and other organic reactions. As

described in **Section 1.1**, literature studies show that there is cooperativity between acid-base bifunctional heterogeneous catalysts that lead to the formation of the final aldol condensation product. Plotting opposed chemical gradients of acidic and basic functionalities will allow to elucidate how proximal the acidic and basic sites need to be for effective cooperativity. This will provide information on critical spatial parameters to be satisfied to synthesize enhanced catalysts for aldol reactions. Another advantage of using the vapor phase plotter in the preparation of catalyst templates is that complete control over the density of catalytic sites on the substrate will be afforded. Here, employing chemical gradients of gradually varying chemical densities will reduce preparation time and allow for optimization of the catalyst density (i.e. loading) in a more efficient manner.

1.4 Objectives and Overview of the Present Research

For the research described in this dissertation, a primary objective was to synthesize a highly fluorescent dye that is still fluorescent enough upon undergoing an aldol reaction so that the reaction may be followed at the single molecule level. This would allow *in-situ* characterization of the intrinsically variable catalytic sites within heterogeneous catalysts. The information gathered is a step towards fully understanding the nanoscale interactions between the reactants and catalytic sites so that sustainable catalysts to be design and used in aldol reactions. **Chapter 3** describes the complete synthesis of NR-Al, a new dye designed and used for the purpose of studying aldol reactions at the single molecule level. **Chapter 4** demonstrates the utility of this dye to follow aldol reactions *in-situ* at the ensemble level. **Chapter 5** demonstrates, for the first time, the fluorescence emission of NR-Al and products of the aldol reaction on catalyst thin films at the single molecule level. This chapter also describes work towards *ex-situ* and *in-situ* aldol

reactions on catalyst thin films. The work in this dissertation focuses on crossed-aldol reactions between a ketone and an aldehyde reactant. The ketone reactants employed here are acetone and acetophenone, while the NR-Al acts as the reactive aldehyde.

Since the aldol reaction forms two products, the aldol addition and aldol condensation products, and it has been shown that a cooperativity of acidic and basic sites enhance aldol product formation, another objective is to employ heterogeneous acid-base bifunctional catalysts to study how different catalytic sites influence product formation. In **Chapter 4**, the heterogeneous catalysts employed were a magnesium-zirconium-cesium doped silica material (Mg-Zr-Cs/SiO_2), and a commercial magnesium oxide (MgO). Fumed silica (SiO_2) was employed as a control. The products of aldol reactions were characterized by fluorescence and by high performance liquid chromatography (HPLC) and HPLC-mass spectrometry (HPLC-MS).

Chapter 5 describes preliminary work towards following aldol reaction events at the single molecule level catalyzed by thin films of inorganic silica materials. The films employed here were composed of a sol-gel derived Mg-Zr-Cs/TMOS material. The fluorescence emission of the products of *ex-situ* aldol reactions was measured and compared to that of the unreacted NR-Al. This chapter also describes work towards following aldol reactions occurring on the catalyst film in real time. A common technique used to follow single molecule fluorescence, widefield microscopy, was employed for these experiments; **Chapter 2** describes this technique in detail.

Lastly, the importance of methods able to pattern specific areas of a substrate with minimal to no perturbation of the surrounding areas was discussed in **Section 1.3**. Such methods are valuable when designing catalysts having various acidic and basic site densities as well as tuning the strength of the active sites by incorporation of different organic precursors to provide selectivity for the desired reaction products. In this dissertation, a new patterning method based on

vapor phase plotting of organosilane precursors is introduced. The method is described in detail in **Chapter 6**. Two types of organosilane precursors were employed: n-octyltrichlorosilane and 3-cyanopropyltrichlorosilane. Thin film chemical gradients and square patterns were plotted from the aforementioned vapor precursors. Common techniques to characterize thin chemical films were employed for the characterization such as water contact angle (WCA) measurements, spectroscopic ellipsometry, and X-ray photoelectron spectroscopy (XPS). The latter was also employed for an estimation of the spatial resolution of this method. The vapor phase plotting method presented in this dissertation can potentially plot thin films of organic acid-base bifunctional gradients to study aldol catalysis at the nanoscale. A primary advantage of this application is that no pre-made masks are required to pattern the substrates. Also, chemical gradients with different precursors and different densities of those precursors would be possible to make at once, reducing preparation time and allowing the study of more complex catalyst systems.

This dissertation concludes with a summary of what has been accomplished and addresses new questions that arose as well as proposed studies and future directions, **Chapter 7**. Cited references are listed in **Chapter 8** and Appendixes (A-D) are given at the end; the Appendixes provide additional information related to the studies presented in Chapters 3-6.

Chapter 2 - Materials Preparation and Characterization

2.1 Preparation of Heterogeneous Catalysts

The use of wet chemistry methods, such as precipitation, coprecipitation, hydrothermal synthesis or the sol-gel process, for the preparation of heterogeneous catalysts is well known.[93] These methods produce solids with large specific surface areas and high porosity in the meso- and macro-pore ranges. [94] In each case, a solid network is formed from solution via hydrolysis, condensation, and drying of molecular precursors in solution, **Figure 2.1**.[93, 95] In this dissertation, a sol-gel process was used for the preparation of inorganic heterogeneous catalysts. The catalytic properties of the materials thus obtained were then used in ensemble aldol reactions, **Chapter 4**, and as inorganic-silica thin catalyst films in studies at the single molecule level, **Chapter 5**.

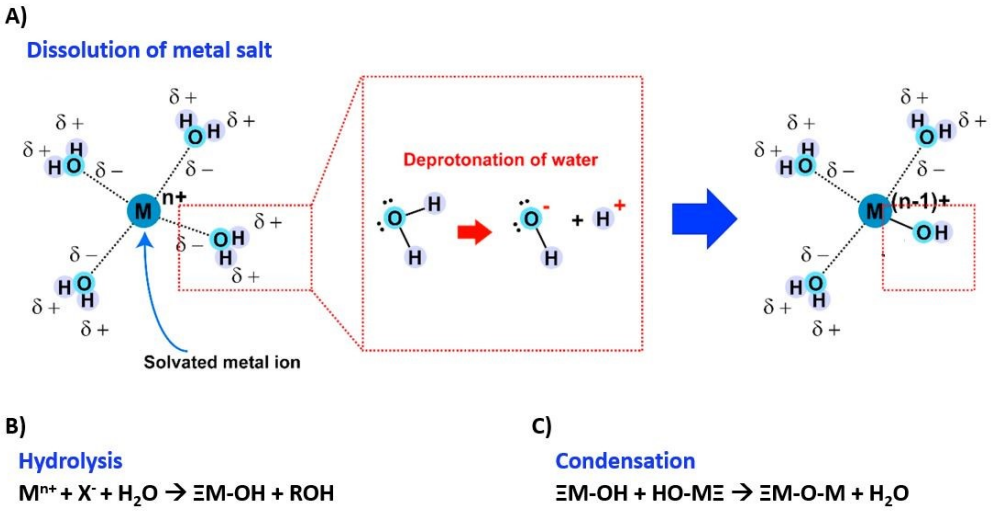

Figure 2.1 Sol-gel chemistry in metal oxide materials. **(A)** A schematic of the reaction between metal ions and water molecules to form metal hydroxides. After water molecules are deprotonated, metal and hydroxide ions are bound to each other by electrostatic interaction. Representative chemical reactions are shown for **(B)** hydrolysis and **(C)** condensation. Reprinted with permission. **Copyright © 2017 Elsevier B.V. All rights reserved.**[96]

2.1.1 A Sol-gel Method for Heterogeneous Mg-Zr-Cs/SiO_2 Catalysts

Abdulhafiz Usman, Dept. of Chemical Engineering, synthesized the Mg-Zr-Cs/SiO_2 catalyst employed in **Chapter 4**. Fumed silica (Sigma-Aldrich) was calcined in flowing air at 500 °C for 3h in a furnace (Barnstead F1500). The silica was then impregnated with stock solutions of aqueous $Mg(NO_3)_2 \cdot 6H_2O$ (0.5 M), $ZrO(NO_3)_2 \cdot xH2O$ (0.1 M) and $CsNO_3$ (0.5 M) (Sigma-Aldrich) to yield catalyst particles having magnesium, zirconium, and cesium theoretical contents of 0.025 wt.%, 0.033 wt.% and 13 wt.%, respectively. The aqueous mixture was subsequently immersed in an ultrasound bath and sonicated at 40 °C for 24 h, followed by drying in an oven overnight at 90 °C. The catalyst was further calcined in flowing air at 500 °C for 3 h and used within 3 days. The catalyst was stored in a desiccator prior to use.

2.1.2 A Sol-gel Method for Mg-Zr-Cs/TMOS Catalyst Films

Abdulhafiz Usman developed the sol-gel recipe. I employed the developed recipe to prepare the Mg-Zr-Cs/TMOS catalyst films used in **Chapter 5**. The same metal nitrate stock solutions described above were employed in preparation of the sol used to prepare catalyst films. The sol was comprised of tetramethoxysilane (TMOS, 98%), ethanol (HPLC grade), water (HPLC grade) and 0.1 M HCl in molar ratios of 1:100:12.8:0.018 (TMOS:ethanol:water:0.1M HCl). In preparation of this sol, the components were first added to a clean glass vial in the following order: TMOS, ethanol, water. Afterward, the sol was stirred for 30 sec, then the nitrate solutions were added so that the theoretical content for Mg, Zr, and Cs were 0.025 wt.%, 0.033 wt.% and 6 wt.% respectively. The sol was subsequently stirred for an additional 30 sec and 0.1 M HCl was added. The sol was then stirred for another 2 h and aged for 24 h in a desiccator prior to use. Each catalyst film was formed by spin coating (Specialty Coating Systems, Inc., P-6000) a 150 μL volume of

the sol onto the substrate (25 X 25 mm glass cover slips, or silicon) at 2500 rpm for 30 sec. The catalyst films were aged for an additional 24 h in a desiccator and calcined in flowing air at 500 °C for 3 h. Once the furnace (Barnstead F1500) had cooled down to room temperature, the films were removed, stored in a desiccator and used within 1 day. Finally, the catalyst-coated substrates were exposed to an air plasma for 2 min prior to use.

2.2 Characterization of Heterogeneous Catalysts

The need for catalyst characterization, both structurally and compositionally is of utmost importance in order to better understand their functionality and specifically how the active sites within the catalyst influence a reaction. Insights into their structural/chemical properties will help the synthesis of sustainable catalysts for their use in academia and, perhaps more importantly, industrial settings as is discussed in **Chapter 1**. Various literature reviews have been published reporting a compilation of common techniques for *ex-situ* catalyst characterization.[97-100] In this dissertation, some of the common techniques discussed in the above reviews were employed for the characterization of the catalysts and the silica controls employed in **Chapter 5**. Structural characterization employed X-ray diffraction (XRD), transmission electron microscopy (TEM), scanning electron microscopy (SEM), and surface area measurements by BET. Chemical characterization employed energy dispersive X-ray spectroscopy (EDS), inductively coupled plasma-optical emission spectroscopy (ICP-OES), X-ray photoelectron spectroscopy (XPS), and temperature-programmed desorption (TPD) of CO_2 and NH_3.

2.2.1 X-ray diffraction (XRD)

X-ray diffraction (XRD) is an analytical technique employed for phase identification of crystalline materials and can provide information on unit cell dimensions. X-rays are generated by a cathode ray tube, filtered to produce monochromatic radiation, collimated and directed toward the sample. A diffracted ray, which satisfies Bragg's Law, is obtained from the interaction between the incident rays and the sample, as given in **Equation 2.1**.[101]

$$n\lambda = 2d \sin\theta \qquad \textbf{(Equation 2.1)}$$

The above equation relates the wavelength of incident light (λ), the angle of incidence (θ), and the lattice spacing of the crystal (d); where (n) is an integer and represents the order of diffraction. By scanning the sample through a range of 2θ angles, all possible diffraction directions of the lattice are attained. The material is then identified by converting the diffraction peaks to d-spacings and comparing those with standard reference patterns.

Herein, XRD patterns of the as-synthesized Mg-Zr-Cs/SiO_2, the commercially available MgO (Nanoscale Materials), and fumed silica (Sigma-Aldrich) were obtained by Abdulhafiz Usman using a desktop X-ray diffractometer (Rigaku Miniflex II).

2.2.2 Transmission Electron Microscopy (TEM) & Scanning Electron Microscopy (SEM)

TEM and SEM are widely used as they are capable of imaging at a significantly higher resolution than light microscopes. Both techniques employ a beam of electrons to form an image of the material being examined; the resulting image is dependent upon how the beam of electrons

interacts with the material. In TEM, the specimen is usually less than 100 nm thick or is suspended on a grid. The transmitted beam of electrons from the sample is highly dependent on its properties (i.e. density, composition) and is focused by the objective lens into an image on a fluorescent screen or a CCD camera.[102]

In SEM, the electron beam is raster scanned on the sample surface, allowing the electrons to interact with atoms on the sample. The beam is scanned across the sample as the intensity of the detected signal is recorded to produce an image of the sample. Simultaneous SEM/EDS systems analyze the elemental composition of the sample. When the sample in the SEM is hit with high energy electrons, the EDS detector collects the X-rays produced from the sample. Characteristic X-rays from the difference in energy between the higher energy shell and lower energy shell within the sample provide information on its elemental composition. The main difference between SEM and TEM is that TEM provides information about the two-dimensional internal structure of the sample whereas SEM provides a three-dimensional image of the surface morphology as well as elemental analysis.[102]

Herein, TEM images were acquired by Abdulhafiz Usman. TEM images were acquired using a FEI Tecnai G2 Spirit BioTWIN microscope operating at 120 kV. The samples were prepared by dispersing them in ethanol, sonicating them, and then depositing them on a microgrid before imaging. SEM images were obtained using a Hitachi S-3500N microscope with an operating voltage of 20 kV. EDS was employed for elemental analysis using an Oxford detector (< 135 eV). The catalyst samples were sputter coated with palladium before imaging.

2.2.3 BET Surface Area and BJH Pore Size Distribution

The Brunauer, Emmet and Teller (BET) theory is commonly employed to measure the surface area of solid or porous materials. This theory evaluates the level of gas adsorption on a material surface to determine its specific surface area in units of area per mass of sample (m^2/g). Experimentally, the physical adsorption of an inert gas (i.e. nitrogen, argon) onto the surface of the sample at cryogenic temperatures is measured as a function of the pressure of the adsorbing gas. As the relative pressure is increased, the gas molecules form a monolayer on the material, and the number of adsorbed molecules can be calculated from the volume adsorbed. Since the cross-sectional area of the gas adsorbed is known, the area of the accessible surface can be calculated from a mathematical model described by the BET formula, as given in **Equation 2.2**.[103]

$$\frac{P}{V_\alpha(P_0-P)} = \frac{1}{V_m C} + \frac{C-1}{V_m C}\left(\frac{P}{P_0}\right) \qquad \textbf{(Equation 2.2)}$$

The above equation is employed to determine the number of molecules required to form a monolayer, V_m, of adsorbed gas onto a solid surface. This mathematical formula describes the relationship between the number of gas molecules adsorbed (V_α) at a given relative pressure (P/P_0), and the volume of gas molecules forming a monolayer (V_m); where C is the BET constant and is related to the heat of adsorption. The BET equation describes the linear relationship between $P/V_\alpha(P_0/P)$ and P/P_0. The surface area, SA, is calculated from the slope and intercept according to **Equation 2.3**, where CSA is the cross-sectional area of the adsorbate gas.[103]

$$\text{SA} = \frac{1}{slope+intercept} * \text{CSA} \qquad \textbf{(Equation 2.3)}$$

The Barrett, Joyner, and Halenda (BJH) theory is a common method for calculating pore size distributions from experimental isotherms using the Kelvin model of pore filling. The pore size distribution can be determined based on the external pressure required to force the gas into a pore against the opposing force of the gas (i.e. surface tension). **Equation 2.4** shows the parameters involved in the Kelvin model; where P is the actual vapor pressure, P_{sat} is the saturated vapor pressure when the surface is flat, γ is the liquid/vapor surface tension, V_M is the molar volume of the adsorbate, R is the gas constant, r is the radius of the adsorbate, and T is the temperature. This model only applies to the mesopore and small macropore size range.[104]

$$\ln \frac{P}{P_{sat}} = \frac{2\gamma V_M}{rRT} \qquad \textbf{(Equation 2.4)}$$

BET surface area and pore size distribution measurements were acquired by Murilo Toledo, Chemical and Petroleum Engineering, University of Kansas. Measurements were done on a Micromeritics ASAP 2020 Surface Area and Porosity Analyzer. Samples were first dehydrated in a 1430 series VWR vacuum oven for 24 h at 150 ºC at a pressure of < 77 Torr. To avoid undesirable interactions with atmospheric moisture, samples were kept in a humidity-free environment in a Sanplatec Dry Keeper Auto Desiccator Cabinet. Prior to surface area and porosity measurements, all samples went through an outgassing step for 12 h at 350 ºC under vacuum. Nitrogen sorption isotherms were collected at 77 K over a relative pressure range of 0.05 to 0.995; measured every 120 min. Mesopore-size distribution was evaluated by the nitrogen desorption isotherm and by the BJH method.[104] Total surface area was calculated by the BET method.[103] Total pore volume was determined by the amount of nitrogen adsorbed at a relative pressure of 0.99.

2.2.4 Inductively Coupled Plasma (ICP) Spectroscopy

Inductively coupled plasma optical emission spectrometry (ICP-OES) is a common analytical technique employed for the detection of chemical elements. The plasma is a high temperature source of ionized gas (i.e. argon), which ionizes the sample of interest, and produces electronically excited atoms and ions. Relaxation of these atoms and ions produces radiation at wavelengths characteristic of the element involved, which is used for elemental analysis. A spectrograph and a detector array such as a CCD camera, are employed to record the plasma emission spectrum and thus identify the elements present in the sample. The emission intensity can then be analyzed to quantify the elemental composition of the sample while employing standards with known concentrations.[105]

In this dissertation, the elemental composition of the catalysts was determined using a Varian 720-ES ICP-OES. Samples were digested in nitric acid for this analysis.

2.2.5 X-ray Photoelectron Spectroscopy (XPS)

XPS is a powerful and widely used technique to characterize the surface elemental composition of a material. The method works by irradiating a sample with a beam of X-rays of known energy ($h\nu$), which results in the ejection of electrons from specific orbitals (core-shell electrons). The kinetic energy (KE) of the ejected electrons is then measured by an electron analyzer to determine their binding energy (BE). The BE depends on the element detected, the orbitals from which the electrons are emitted, and the chemical environment. The electron analyzer measures the intensity of the ejected electrons as function of BE, where each prominent peak corresponds to electron emission from the core electronic orbitals of atoms of a specific element, and the area under the peak corresponds to the amount of such element present on the sample.

Characteristic shifts in an atom's BE depend on its chemical environment and allow detailed information to be obtained about the material's surface chemistry. **Equation 2.5** shows how the BE is calculated, where ϕ_{spec} is the work function of the spectrometer employed.[106]

$$BE = h\nu - KE - \phi_{spec} \quad \textbf{(Equation 2.5)}$$

Herein, XPS data of the catalysts were acquired by Dr. Bala Balasubramanian at the Nebraska Nanoscale Facility: National Nanotechnology Coordinated Infrastructure and the Nebraska Center for Materials and Nanoscience. A Thermo Scientific K-alpha$^+$ XPS with a monochromatic Al Kα X-ray source (1486.6 eV) was employede. XPS spectra were acquired using a 400 μm spot size, 50.0 eV pass energy, and 0.100 eV step size. The binding energies were corrected for charge shifts using the C (1s) peak of adventitious carbon at 284.8 eV as a reference.[41] Deconvolution of the XPS data was done using OriginPro software

2.2.6 Temperature Programed Desorption (TPD)

TPD involves the observation of gas molecules desorbed from a sample surface as the temperature is increased to obtain information about the nature of the binding sites on the surface (i.e. strength) as well as the amount. Gas molecules such as CO_2 and NH_3 are typically employed to probe basic and acidic surface sites respectively by absorbing on such sites. The amount of gas molecules absorbed gives a measure of the density of the chemical environment of the material being probed (i.e. basicity, acidity). The temperature required to get the gas molecules to desorb from the material's basic or acidic surface sites gives a measure of their strength. Higher desorption temperatures indicate a stronger binding site (i.e. increased acidity or basicity).[107]

In this dissertation, the acid-base properties of heterogeneous catalysts were determined by TPD of CO_2 and NH_3, employing an Altamira Instruments AMI-200. For CO_2 TPD, 150 mg of catalyst was placed in a quartz tube and treated in helium flow at 450 °C for 1 h, with a heating rate of 10 °C/min. After cooling to 50 °C, a 10% CO_2-He mixture was passed over the samples for 30 min followed by a purge with pure helium until the baseline became stable. Desorption of CO_2 was accomplished by exposing the sample to a helium flow while heating to 500°C at 10°C/min. The same process was employed for NH_3 TPD using a 1% NH_3-He mixture. The desorption profile for both gases was recorded using a thermal conductivity detector.

2.3 Fluorescence Spectroscopy

Fluorescence spectroscopy is a highly sensitive analytical method employed to analyze the fluorescence properties of a fluorogenic sample, including its concentration. This method is widely used because it is fast, simple, inexpensive and the sample can be directly analyzed in solution. The principle is that when a photon of light of appropriate energy is absorbed by organic fluorophores, the subsequent emission of light (fluorescence) is obtained due to the electronic transition between the excited and ground states, as depicted in the Jablonski diagram, **Figure 2.2**. Groups that are responsible for absorption are called chromophores and are often isolated double bonds or conjugated rings. Bathochromic and hypsochromic shifts correspond to shifts in the wavelength of absorption of chromophores to longer or shorter wavelengths, respectively. Conjugation (i.e. C=C-C=C, C=C-C=O, Ph-C=C) typically leads to an increase in molar absorptivity and to a bathochromic shift. Furthermore, the attachment of an auxophore (i.e. -OH, $-NH_2$, -OR, -NHR, -Br) to a chromophore also leads to a bathochromic shift. This occurs due to sharing of the non-bonding pair(s) of electrons on the auxophore with the chromophore, which

leads to an extended conjugation to lower the energy of the π^* orbital associated with the chromophore, and thus to a bathochromic shift.[108] In **Chapters 4** and **5,** fluorescence spectroscopy was employed as a simple means to detect the different products obtained from NR-Al aldol reactions with acetone or acetophenone.

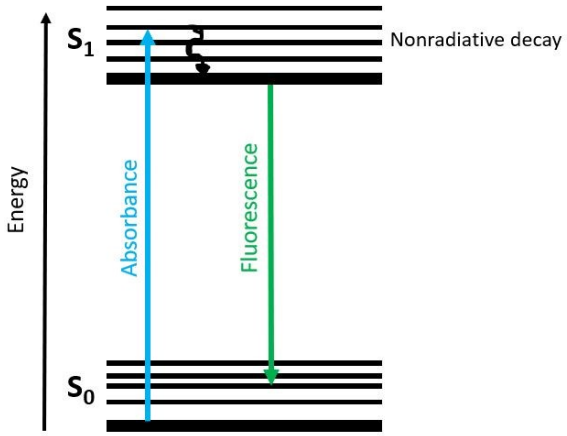

Figure 2.2 Jablonski diagram showing the principle of fluorescence. S_0 is the ground singlet state, S_1 is the first excited single state. The black lines between the electronic states represent their vibrational sub-levels. For simplicity, rotational states, spins and phosphorescence through intersystem crossing are not shown.

2.3.1 Widefield Fluorescence Microscopy

Since a typical fluorescence measurement is done at the ensemble level, only the average value of the parameter under study is obtained and critical information found at the nanoscale may be masked or lost. This becomes particularly important when studying materials with intrinsically varying properties such as heterogeneous catalysts, where the average experimental value may not represent the most active catalytic sites. This has led scientists to search for methods where single catalytic sites and single reaction turnover events can be studied individually at the single molecule level. Among these methods is single molecule/particle tracking (SMT, SPT) as it provides spatio-

temporal resolution in the nanometer-millisecond domains. The spatio-temporal resolution of SMT methods has aided in providing evidence of temporal and spatial heterogeneity of nanostructures and heterogeneous catalysts in different environments.[52-54, 109]

Figure 2.3 shows a schematic diagram of the epi-illumination mode wide-field microscope employed in typical SMT experiments. The material under study is doped with nanomolar or sub-nanomolar concentrations of fluorophores. In this set up, the laser beam is reflected off a dichroic mirror and focused on the back aperture of the microscope objective. The fluorescence produced by the fluorogenic molecules on the sample is collected by same microscope objective and is directed through the dichroic mirror. An additional filter removes residual excitation light and the fluorescence is detected by a CCD camera.

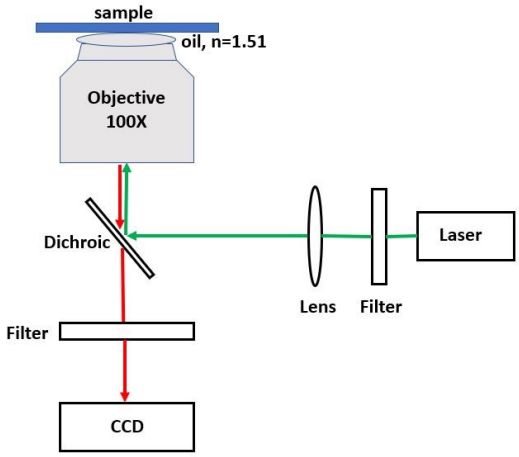

Figure 2.3 Widefield microscope setup for fluorescence measurements.

In SMT measurements, a high numerical aperture (NA) objective lens is employed to ensure that the maximum possible amount of emitted fluorescence is collected, thus improving the signal to noise ratio, while also yielding the best possible spatial resolution. **Equation 2.7** shows

the parameters involved in NA, where n is the refractive index of the imaging medium and θ is the maximum collection angle of the objective,

$$NA = n \times \sin\theta \qquad \textbf{(Equation 2.7)}$$

As spatial resolution is inversely proportional to NA, higher resolution may be achieved by employing an objective lens with larger NA. The collection efficiency of the objective also scales as the square of NA, so a large NA also greatly improves the signal detected, **Equation 2.8**.[109] S_s is the signal from a single molecule emitter, C and F are the detection and collection efficiencies of light, ϕ_F is the fluorescence quantum yield, P_p is the incident optical power, σ is the optical cross section, τ is the time over which the signal has been detected, and 0.885 is the estimated value for a microscope set up employing several optic lenses for fluorescence collection. Typical objectives employed in SMT experiments are oil immersion objectives with NA as high as 1.49 in which the oil imaging medium has n = 1.51.

$$S_s = 0.855CF\phi_F P_p \sigma\tau \left(\frac{NA}{\lambda}\right)^2 \qquad \textbf{Equation 2.8}$$

A major improvement in optical microscopic techniques is the introduction of super resolution microscopy where the optical diffraction-limited resolution is surpassed.[110, 111] The diffraction limit is defined by Abbe's law,[112] **Equation 2.9**, where the lateral resolution, R, in the x and y directions of the image plane is limited to about half the wavelength of light, λ. Therefore, even for state-of-the-art microscope objectives with high NA (i.e. 1.3-1.6), the spatial resolution of optical imaging is limited to ~ 200 nm for visible light of 500 nm wavelength. This means that

two sources of light need to be separated by at least 200 nm to be distinguished (resolved) from one another as individual spots.

$$R = \frac{\lambda}{2NA} \qquad \textbf{Equation 2.9}$$

Today, super resolution single molecule microscopies such as stimulated emission depletion (STED),[111] photoactivated localization microscopy (PALM),[113] stochastic optical reconstruction microscopy (STORM),[114] among others are employed as they allow a spatial resolution far below that of the diffraction limit to be obtained. A common approach to achieve this is to precisely and accurately localize the point spread function (PSF) of the single molecule emitter by fitting its intensity distribution to a 2D Gaussian function,[115] **Equation 2.10**. I_0 represents the peak intensity (amplitude) of the fitting, x_0 and y_0 are the central x and y positions of the fit, and σ_x and σ_y are the standard deviations in the x and y directions. The central positions (x_0, y_0) give the precise location of the single molecule emitter, while the amplitude provides the peak intensity of the fluorophore.

$$I(x, y) = I_0 \exp\left[-\left(\frac{(x-x_0)^2}{2\sigma_x^2} + \frac{(y-y_0)^2}{2\sigma_y^2}\right)\right] \qquad \textbf{Equation 2.10}$$

Furthermore, the localization precision, σ, can be improved with more photons, N, collected,[116] **Equation 2.11**. Thus for 100 photons detected for a single molecule employing objective lenses with high NA (1.3-1.6), and an emission wavelength of 500 nm, the localization precision is ~ 20 nm or ten times better than expected from the diffraction limited resolution.

$$\sigma \approx \frac{R}{\sqrt{N}}$$ **Equation 2.11**

Super resolution single molecule microscopies enable tracking the dynamics of individual fluorophores in different materials across video frames in real time. These methods provide detailed information about time-dependent translational motions of the molecules as well as adsorption, partitioning, and chemical reaction events. In this dissertation, widefield fluorescence microscopy and SMT methods were employed to detect single molecules of NR-Al and aldol products doped on thin catalyst films as well as to follow catalysis of individual NR-Al aldol reactions with acetone vapor in real time.

2.3.2 Two-Channel Spectroscopic Imaging

The wide-field microscope setup employed in **Chapter 5** is depicted in **Figure 2.4.**

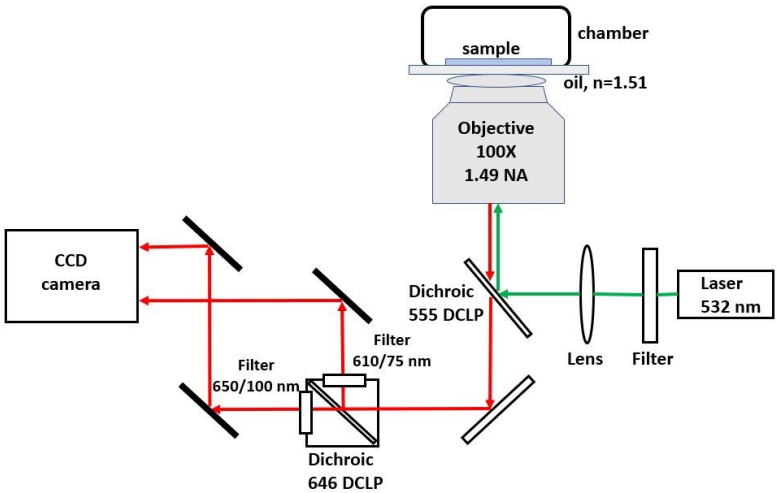

Figure 2.4 Widefield microscope setup for two-channel spectroscopic imaging.

A 532 nm laser delivering 0.6 ± 0.1 mW of optical power to the sample was employed to excite Nile Red, Nile Red Aldehyde (NR-Al), and the products of the aldol reactions. The excitation light was passed through various optical components (i.e. mirrors, filters, polarizers) and a spinning optical diffuser prior to directing it into the microscope. The light was reflected from a dichroic beam splitter (Chroma 555 DCLP), and subsequently focused into the back aperture of a 1.49 NA 100X oil immersion objective (Nikon, Apo-TIRF). The illuminated area in the sample was ~ 14 μm x 14 μm. The fluorescence emission from the fluorogenic molecules was collected using the same objective, in an epi-illumination geometry. The residual excitation light was separated from the fluorescence by passing it through the same dichroic beam splitter and a 570 nm long-pass interference filter (Chroma ET570). The fluorescence was then directed into an image splitter (Cairn Research OptoSplit II) and passed through a second beam splitter (Chroma 646 DCLP) and two bandpass filters (610/75 nm and 650/100 nm) in the reflected and transmitted channels, respectively. This allowed for two spectral images with spectral bands spanning 610 ± 38 nm and 674 ± 26 nm to be viewed. The fluorescence light collected was detected by an electron multiplying (EM) CCD camera (Andor iXon DU-897) operating in conventional mode. All samples were imaged under nitrogen atmosphere, which was maintained by a custom-made chamber. Fluorescence videos 100 frames (0.5 sec/ frame) in length were acquired at different positions within a ~0.5 cm radius from the center of the sample.

The videos obtained were then analyzed using software written in-house in the LabView programming environment. The software corrected for image off-set and rotation resulting from the optical system; typical experiments employed rotations of ~ ±1°. The software located individual fluorescent spots in each frame and automatically located its pair in the second image. The spots were approximated by Gaussian intensity profiles, where fitting the spots to 2D Gaussian

functions allowed for the determination of their location and peak signal.[62, 115] The fluorescence spots located at the same position (within its Gaussian profile) across the video frames were linked to obtain their trajectories. Fluorescent spots with trajectories at least 7 video frames in length were analyzed to eliminate short-lived impurity spots. In the case of *in-situ* aldol reactions, fluorescent spots with trajectories at least 14 video frames in length were analyzed. The latter was due to experimental data suggesting that more can be learned from long-lived fluorescent spots that may better provide evidence of chemical reactions occurring in real time.

2.4 Vapor Phase Plotting of Chemical Gradients

In this dissertation, SAM films and gradients were prepared using a simple, inexpensive vapor phase plotter that was designed and constructed in-house. The critical working components of the vapor plotter include a precursor reservoir, a glass capillary for delivery of the precursor vapor to the substrate surface, and an X,Y plotter. **Figure 2.5** shows a schematic diagram and a photograph of the apparatus. Briefly, vapor plotting is accomplished by first loading the precursor reservoir with organosilane solution. An inert carrier gas is then used to sweep organosilane vapor from the reservoir into the capillary, which is connected to the reservoir via flexible tubing. The capillary is mounted to the X,Y-plotter, allowing for it to be raster scanned above the substrate surface. The working end of the capillary is positioned a few tens of micrometers above the substrate, allowing for local regions to be exposed to silane vapor in a controlled manner. The entire apparatus is housed within a sealed deposition chamber that allows for the ambient atmosphere to be controlled during plotting. The entire vapor phase plotting process is described in more detail in **Chapter 6**.

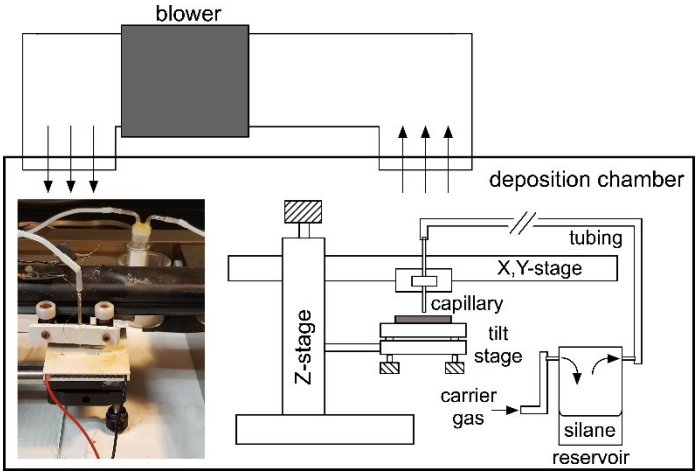

Figure 2.5 Deposition chamber for vapor phase plotting of SAM films and gradients. The inset shows a photograph of the capillary, substrate, reservoir and sample stage. Reprinted with permission. **Copyright © 2018 American Chemical Society.**[117]

2.4.1 Silica Base Layer

Microscope coverslips (Fisher Finest Premium, 25 mm x 25 mm) and cut, polished silicon wafers (University Wafer, boron doped, 10 mm x 20 mm) were used as substrates upon which the SAM films and gradients were deposited. Each substrate was cleaned prior to use by exposure to an air plasma for 5 min. As has been demonstrated previously, organosilane films are best formed on substrates already coated with a silica base layer.[90] The base layer provides a uniformly reactive surface with sufficient silanol sites to allow for efficient attachment of the organotrichlorosilanes.[118] Base layers were deposited from a sol comprised of tetramethoxysilane (TMOS), ethanol (200 proof), and 0.1 M HCl in volume fractions of 0.94:94.0:5.06 (TMOS:ethanol:0.1M HCl). In preparation of this sol, the components were first added to a clean glass vial. The sol was then stirred for 1 h and aged for another 23 h in a desiccator prior to use. Each base layer was formed by spin coating (Specialty Coating Systems, Inc., P-6000) a 150 µL volume of the sol onto the substrate at 5000 rpm for 30 s. Base layers prepared in this manner had thicknesses of 16 ± 5 nm on average, as determined by spectroscopic ellipsometry.

The base-layer-coated substrates were stored in a desiccator for at least 24 h prior to use and were subsequently exposed to an air plasma for 2 min prior to vapor plotting.

2.4.2 Vapor Phase Plotting of Chemical Gradients /Patterns

Self-assembled monolayer films and gradients were prepared from *n*-octyltrichlorosilane (97%) and 3-cyanopropyltrichlorosilane (97%) precursors. The organotrichlorosilanes were obtained from Sigma-Aldrich and were used as received. Each was dissolved in a solvent prior to being transferred to the reservoir. The solvents tested include toluene, *n*-heptane, and *n*-butanol.

2.5 Characterization of Chemical Gradients and Catalyst Thin Films

Film deposition and gradient formation were verified by sessile drop water contact angle (WCA) measurements, spectroscopic ellipsometry (SE), and by X-ray photoelectron spectroscopy (XPS) mapping. The same methods also allowed for the gradient profile to be recorded. Catalyst thin films were characterized by SE and XPS mapping.

2.5.1 Water Contact Angle (WCA) Measurements

Water contact angle measurements were employed as it is a facile and common technique for the characterization of the macroscopic wettability properties of thin films and surfaces. The apparatus employed was built in-house, with all the components fixed on an optical table, as shown in **Figure 2.6**. For WCA measurements, 0.1-0.5 μL droplets of pure water (18 MΩ·cm, B-pure, Barnstead) were placed on the SAM films at several locations, and at 2 mm intervals along each gradient length, with three replicate measurements at 1 mm spacings across the gradient width using a microliter syringe (Hamilton). The home-built instrument was equipped with a CCD

camera (ProVIDEO, CVC-140) and a zoom lens (Navitar) that were used to photograph the individual water droplets. A plugin for the freely available ImageJ software[119] was used to determine the contact angle from each photograph.

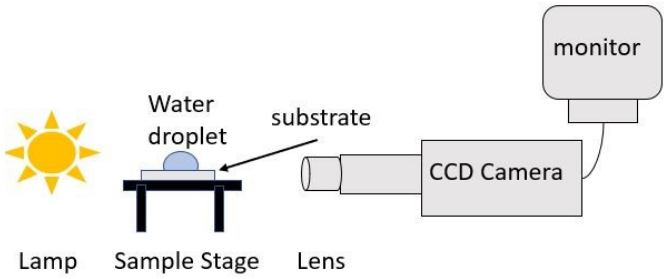

Figure 2.6 Home-built apparatus for WCA measurements.

2.5.2 Spectroscopic Ellipsometry (SE) Measurements

Spectroscopic ellipsometry is a non-contact, non-destructive optical technique that is widely used to characterize thin films and multi-layer semiconductor structures. In this dissertation, an α-SE spectroscopic ellipsometer (J.A. Woollam Co., Inc.) was employed to measure the thickness of the silica base layer and of the chemical gradient overlayer from samples deposited on silicon wafers. The use of silicon substrates ensured a strong optical reflection from the film-substrate interface, affording the measurement precision needed to determine the thickness of sub-monolayer films.

Ellipsometry measures the change of polarization of the light source after it reflects from the substrate surface. The change in polarization involves two parameters, the amplitude ratio tan(ψ), and a phase difference (Δ). The measurement involves the reflection of the linearly polarized light (across all visible wavelengths) from the sample substrate and the output polarization (s) is measured. Since the output response depends on optical properties of the

material such as thickness, monolayer and sub-monolayer chemical films on the substrates were readily measured. **Equation 2.6** shows the parameters involved in the change of polarization (ρ); where r_ρ and r_s represent the reflectivity of ρ and s polarizations.

$$\rho = \frac{r\rho}{rs} = \tan(\psi)\, e^{i\Delta} \qquad \textbf{(Equation 2.6)}$$

All ellipsometry raw data were globally fit to the "Si with Transparent Film" model available in the CompleteEASE software provided in the instrument. In all cases (both base layer and organosilane-coated base layer), the films were treated as a single layer on the substrate, because the refractive indexes of the films are all very similar, n = 1.457 (at 633 nm).[120] **Figure 2.7** shows ellipsometric data for the silica base layer **(A)**, and for the base layer after vapor phase plotting of octyltrichlorosilane **(B)**.

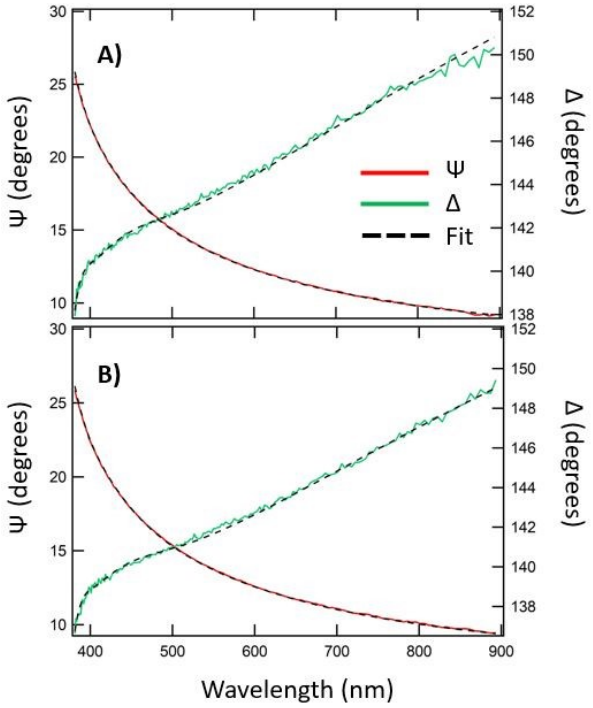

Figure 2.7 Spectroscopic ellipsometry data for **(A)** a thin base-layer on silicon and **(B)** the same film after vapor phase plotting of octyltrichlorosilane. The colored lines represent the raw data and the dashed lines are the fits of these data employing a model for a single transparent film on silicon. The Cauchy relationship was employed to model film dispersion. The parameters obtained from global fits to the data shown in **(A)** are: A= 1.486 ± 0.0090, B= -0.01545 ± 0.00233 μm^2, C= 0.00144 ±0.00025 μm^4, n = 1.4567, thickness= 12.60 ± 0.081 nm; in **(B)**: A= 1.508 ± 0.0087, B= -0.02559 ± 0.00225 μm^2, C= 0.00215 ± 0.000239 μm^4, n= 1.4577, thickness= 13.52 ± 0.080 nm. The mean square error in each measurement was 1.507 and 1.512, respectively. The difference between the two measured thicknesses, ~ 0.92 nm, gives the thickness of the deposited thin film organochlorosilane on the substrate.

To determine the organosilane layer thickness, the base-layer thickness was first measured prior to vapor plotting of the organotrichlorosilane. To avoid errors in the measured thickness caused by condensed water layers, all ellipsometric measurements were made under a dry nitrogen atmosphere inside a Plexiglas chamber. The chamber was purged with nitrogen for at least 30 min prior to each set of measurements, and the purge was maintained throughout each experiment. The base-layer thickness was measured at a series of positions separated by 2 mm spacings along the substrate. The SAM film was then deposited atop the base layer and the film thickness was

remeasured at each of the previous locations (to within ± 1 mm). The SAM film thickness was obtained as the difference between the full film thickness and that of the base layer.

To determine the thickness of the catalyst film, the surface layer of the silicon substrate was first measured at a series of positions separated at 2 mm intervals along and across the substrate. The silicon substrate was exposed to an air plasma for 5 min and the same precautions to avoid condensed water on the surface were employed as explained above. The catalyst film was deposited, and the film thickness measured at each of the previous locations (to within ± 1 mm). The catalyst film thickness was obtained as the difference between the full film thickness and that of the silicon surface.

2.5.3 X-ray Photoelectron Spectroscopy (XPS)

XPS was also employed to characterize the chemical gradients and catalyst films. The only difference is that a different instrument was employed. XPS measurements of the chemical gradients and catalyst films were acquired by Dr. Anna Forzano and Shelby Wheatherbee, respectively, Dept. of Chemistry, Virginia Commonwealth University. The working principle of XPS was described in **section 2.2.5**.

Chapter 3 - Synthesis of Aldol Reactive Nile Red Derivative

Distribution of Work

I synthesized the dye and did much of the characterization. Dr. Man Zhang provided her synthetic expertise in proposing a similar reaction mechanism to get the dye of interest.

3.1 Introduction

The need for assays that are relatively quick, robust and inexpensive is crucial when designing and optimizing catalyst materials. In this realm, molecular probes have been found suitable for following chemical reactions in real time to measure and rank catalytic activities at the ensemble level.[121, 122] Fluorogenic probes are now widely used in high-throughput screening and rapid characterization of catalysts by detecting a fluorescence growth during the reaction.[49-51] Fluorogenic probes have also been explored when assessing the catalytic activities of various catalysts under different conditions and in screening catalysts useful for synthetic organic chemistry.[123-125]

Aldol reactions are important carbon-carbon bond forming reactions in synthetic organic chemistry and employed in industrial reactions of feedstocks, commodity chemicals, and biomass-derived renewable liquid fuels.[14-16,21] The need for molecular probes to follow aldol reactions has attracted interest among researchers. For example, Guo and Tanaka synthesized a fluorogenic aldehyde bearing a 1,2,3-Triazole moiety for monitoring the progress of aldol reactions catalyzed by various amines. The Triazole moiety that connected a fluorescent and a non-fluorescent group led to fluorescence quenching of the fluorophore, however, the product of the aldol reaction was fluorescent.[59] Similarly, Katsuyama et al. synthesized fluorogenic probes where benzaldehydes

conjugated with aryl groups via a double or triple bond were non-fluorescent, but the product of aldol reaction was fluorescent in buffer solutions.[126] Other research groups focused on aldol reactions catalyzed by piperidine while employing coumarin chalcones incorporating either an aldehyde or ketone moiety. Here, reaction conditions employed polar solvents such as ethanol and acetonitrile and reaction mixtures were refluxed.[60, 127]

While the above studies are good demonstrations of fluorogenic probes used in aldol reactions, little information about the intrinsic-localized properties of catalysts is learned from bulk measurements. The above studies show that aldehyde probes "turn on" upon undergoing aldol reaction while coumarin dyes show unique spectral shifts upon aldol reaction. However, none of the dyes currently presented in the literature are well suited for single molecule spectroscopy (SMS) studies where high fluorescence is a requirement for detection and tracking. Furthermore, SMS studies are preferably performed at room temperature, a condition that is more manageable in optical microscopic experiments. Therefore, the need for a molecular probe for aldol reactions that is suitable for SMS is essential to study intrinsic-localized catalytic activity in heterogeneous catalysts. This information is important when designing and optimizing catalysts used in various industries (i.e. to make aldol products employed for commodity chemicals and biomass derived renewable liquid fuels).

In this chapter, the synthesis of a new derivative of Nile Red that incorporates a reactive aldehyde moiety (NR-Al) is described in detail. NR-Al was confirmed by ^{1}H and ^{13}C NMR, and high-resolution mass spectrometry. The reactive Nile Red derivative was selected because it is highly fluorescent and has been widely employed in single molecule detection, spectroscopy, and tracking studies.[128-130] This dye is useful in such studies because its emission spectrum exhibits an appreciable red shift in wavelength with increase in solvent polarity, thus making its chromophore

highly dependent on its surroundings. The red shift is explained by the stabilization of certain molecular motions that provide a pathway for fast non-radiative decay of the NR in its excited state.[131] Specifically, a twisted intramolecular charge transfer process between its diethylamino and quinoidal moieties is better stabilized by polar solvents than non-polar solvents. The stabilization lowers the energy of the excited state and shifts the emission to longer wavelengths with increasing solvent polarity,[131-133] **Figure 3.1**. In this dissertation, the highly fluorescent and bathochromic properties of the NR chromophore were employed as a simple means to detect different products obtained from NR-Al aldol reactions with acetone and acetophenone. In **Chapter 4**, NR-Al is employed to follow *in situ* aldol reactions catalyzed by heterogeneous catalysts and becomes an important component in gathering initial information about their catalytic activity. In **Chapter 5**, NR-Al and the products of aldol reactions are detected at the single molecule level for the first time. Pre-liminary studies towards *ex-situ* and *in-situ* aldol reactions on catalyst thin films is also reported.

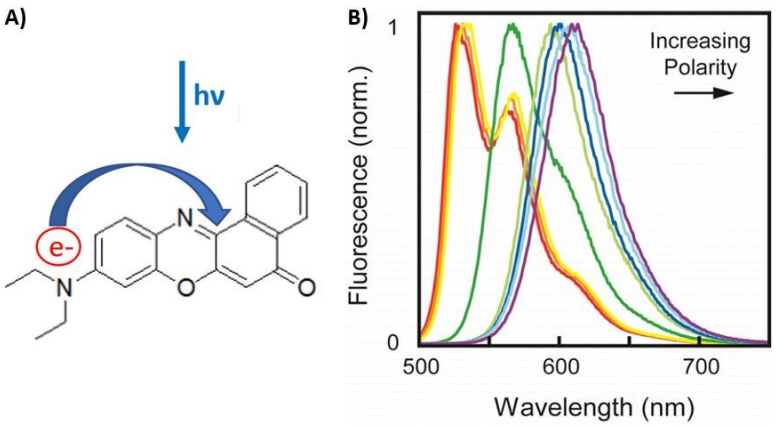

Figure 3.1 A) Nile Red molecular structure and intramolecular charge transfer process. **B)** Fluorescence spectra of NR in hexane (red), heptanes (orange), cyclohexane (yellow), toluene (dark green), chloroform (light green), dicloromethane (dark blue), acetone (light blue), and acetonitrile (dark purple) obtained with 488 nm excitation. Reprinted with permission. **Copyright © 2013, American Chemical Society.**[134]

3.2 Experimental Considerations

3.2.1 NR-Al Synthesis and Characterization

Reagents used in the synthesis of NR-Al were obtained from commercial sources unless otherwise specified and used without further purification. Analytical thin layer chromatography (TLC) was employed to track reaction progress using silica gel 60 F_{254} (Merck) TLC plates. Column chromatography was employed for product purification and employed silica gel 60 (230-400 mesh) as the stationary phase. ^{1}H and ^{13}C NMR spectra were acquired on either 600 MHz (Bruker Avance III HD) or 400 MHz (Bruker Avance NEO) spectrometers. Fourier transform infrared (FTIR) spectra were taken using disposable polyethylene IR cards (Aldrich) as the sample support. Spectra were recorded in transmission mode on a Cary 630 FTIR (Agilent). High-resolution mass spectra were obtained on a LCT Premier Mass Spectrometer (Waters) using electron impact ionization. Fluorescence spectra were acquired on a FluoroMax-2 spectrophotometer (Jobin Yvon Spex) using a Xenon lamp (150 W) as the light source.

3.3 Results and Discussion

3.3.1 Synthesis and Characterization of Nile Red-Al

Synthesis of the aldol-reactive derivative of Nile Red, 9-diethylamino-5-oxo-5H-benzo[α]phenoxazin-2-carboxaldehyde (NR-Al), required six steps and is based upon a previously reported synthesis of Nile Red.[135] A scheme of the steps employed is shown in **Figure 3.2**. ^{1}H and ^{13}C NMR and EI-MS can be found in **Appendix A**. EI-MS was acquired in the Analytical Core Laboratory, University of Kansas Medical Center.

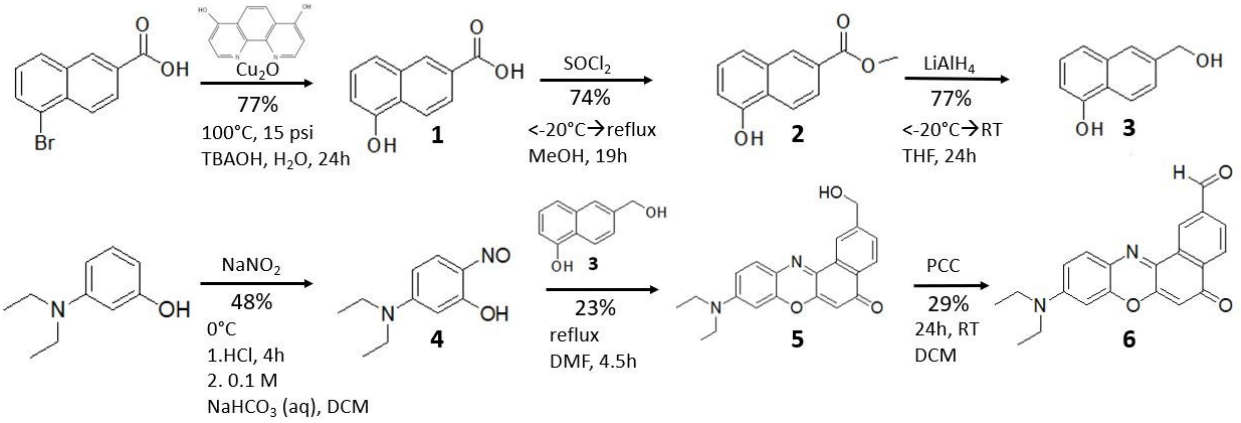

Figure 3.2 Scheme of synthesis of 9-diethylamino-5- oxo-5*H*-benzo[α]phenoxazin-2-carboxaldehyde (NR-Al), **6**. Product yields are given below each reaction arrow.

Synthesis of 5-hydroxy-2-naphthoic acid (**1**). The synthetic procedure reported by Wang et al. was modified to prepare **1**.[136] A 50 mL reactor (Parr 5500 series) equipped with a mechanical mixer was charged with 5-bromo-2-naphthoic acid (1 g, 3.98 mmol, Combi-Blocks, 98%), tetrabutylammonium hydroxide (19 mL, 40% in H_2O, Sigma-Aldrich), Cu_2O (0.028 g, 0.195 mmol, Alfa Aesar, 97%), 4,7-dihydroxy-1,10-phenanthroline (0.085 g, 0.401 mmol, Alfa Aesar), and deionized water (10 mL). The reactor was degassed with Argon for 5 min prior to pressurizing to 15 psi with Argon. The reaction temperature was gradually increased to 100°C and the starting materials allowed to react for 24 h. Afterward, the reaction was cooled to room temperature prior to venting to the atmosphere. The solution was then acidified to pH 2-3 with 2N HCl and extracted with ethyl acetate. The combined organic fractions were dried over anhydrous sodium sulfate and concentrated under vacuum. The crude product was further purified by column chromatography on silica gel using a 1:1 hexane:ethyl acetate to obtain compound **1** as an off-white solid (0.581 g) in 77% yield: ^{1}H NMR (400 MHz, DMSO-d6): δ = 13.02 (s, 1H), 10.33 (s, 1H), 8.51 (d, J = 2 Hz, 1H), 8.21 (d, J = 9 Hz, 1H), 7.92 (dd, J = 2 Hz, 1H), 7.53 (d, J = 8 Hz, 1H), 7.40 (t, J = 8 Hz, 1H),

7.01 (d, J = 7.5 Hz, 1H). ^{13}C NMR (400 MHz, DMSO-d6): δ = 168.00, 153.59, 134.01, 130.60, 128.66, 127.82, 126.80, 124.25, 122.94, 120.18, 110.77.

Synthesis of 5-hydroxy-2-naphthoic acid methyl ester (**2**). Compound **1**, was dissolved in methanol (30 mL, Fischer, ACS grade) and cooled to < -20 °C in a dry ice/isopropanol (IPA) bath for 10 min. Thionyl chloride (1.31 mL, 6.71 mmol, 3 eq, Aldrich, 97%) was then slowly added. The reaction was subsequently allowed to warm to room temperature and then was heated to reflux for 19h. Afterward, the solvent was removed by rotary evaporation. The product was dissolved in ethyl acetate (30 mL) and washed with brine (12 mL). The organic layer was collected and dried over anhydrous sodium sulfate and concentrated under vacuum. The crude product was further purified by column chromatography on silica gel using a 2:1 hexane:ethyl acetate to obtain **2** as a pale yellow solid (0.510 g) in 74% yield, post lyophilization (stored under Argon until use): ^{1}H NMR (400 MHz, DMSO-d6): δ = 10.39 (s, 1H), 8.53 (d, J = 2 Hz, 1H), 8.23 (d, J = 9 Hz, 1H), 7.92 (dd, J = 2 Hz, 1H), 7.56 (d, J = 8 Hz, 1H), 7.41 (t, J = 8 Hz, 1H), 7.02 (dd, J = 1 Hz, 1H), 3.91 (s, 3H). ^{13}C NMR (400 MHz, DMSO-d6): δ = 166.90, 153.60, 133.94, 130.62, 128.04, 127.49, 126.89, 123.85, 123.20, 120.24, 111.02, 52.67. MS calculated for $C_{12}H_{10}O_3$: 202.06299, found: 202.06294.

Synthesis of 5-(Hydroxymethyl)naphthalen-2-ol (**3**). To an Argon charged round bottom flask, equipped with an additional funnel was added **2** (510 mg, 2.52 mmol) and dry THF (25 mL, Acros). The solution was then cooled to -20 ºC for 10 min in a dry ice/IPA bath. A slurry of lithium aluminum hydride (LAH, 191 mg, 5.03 mmol, Alfa Aesar, 97%) in dry THF (15 mL) was subsequently added dropwise over a period of 40 min while maintaining a temperature < 0 °C. The mixture was then allowed to warm to RT and stirring continued overnight, under Argon. The reaction was quenched once reduction of the ester was observed by thin layer chromatography.

Quenching of the reaction was accomplished by first cooling to 5 °C using an ice water bath. For 1 mg of LAH used in the reaction, 1 µL of deionized water, 1 µL of 15% KOH (aq), and 3 µL of deionized water were added, in that order, to quench the reaction. Afterward, the reaction mixture was stirred for an additional 5 h. The crude product was then filtered, and the filtrate was concentrated under vacuum to give **3** as a sticky green solid (0.340 g) in 77% yield: ^{1}H NMR (600 MHz, DMSO-d6): δ = 10.52 (s, broad, 1H), 8.08 (d, J = 9 Hz, 1H), 7.71 (d, J = 1.5 Hz, 1H), 7.37 (dd, J = 2 Hz, 1H), 7.27 (m, 2H), 6.83 (dd, J = 2 Hz, 1H), 5.33 (s, broad, 1H), 4.64 (s, 2H). ^{13}C NMR (600 MHz, DMSO-d6): δ = 154.04, 140.63, 134.85, 127.01, 124.42, 124.21, 124.10, 122.41, 118.30, 108.14, 63.48. MS calculated for $C_{11}H_{10}O_2$: 174.06808, found: 174.06811.

Synthesis of 5-Diethylamino-2-nitrosophenol (**4**). The synthetic procedure reported by Ramm, et al. was followed in this process.[137] 3-Diethylaminophenol (6 g, 0.036 mol, Aldrich, 97%) was dissolved in an acidic solution obtained by mixing 13 mL of 12 N HCl and 8 mL water and was then cooled to 0 °C using an ice water bath. Next, a solution of $NaNO_2$ (2.5 g, 0.036 mol) in 18 mL water was added dropwise over a period of 1 h while keeping the reaction temperature between 0 and 5 °C. The resulting brown slurry was stirred for an additional 4 h and the crude product was collected by filtration, yielding the hydrochloride salt as a yellow precipitate. The hydrochloride salt was subsequently converted to the free amine by diluting in 300 mL 0.1 M aqueous $NaHCO_3$ and extracting with dichloromethane. The combined organic fractions were dried over anhydrous sodium sulfate and concentrated under vacuum to give **4** as a brick-red solid (3.405 g) in 48% yield: ^{1}H NMR (600 MHz, DMSO-d6): δ = 7.31 (d, J = 10 Hz, 1H), 6.91-6.89 (m, 1H), 5.75 (d, J = 2.5 Hz, 1H), 3.61 (m, 4H), 1.19 (t, J = 7 Hz, 6H). ^{13}C NMR (600 MHz, DMSO-d6): δ = 169.26, 157.58, 149.59, 134.88, 115.84, 95.51, 46.1, 14.5. IR (polyethylene/cm^{-1}: 1629, 1514. EI-MS calculated for $C_{10}H_{14}O_2N_2$: 194.10553, found: 194.10558.

Synthesis of 9-Diethylamino-2-hydroxymethyl-5H-benzo[a]phenoxazine-5-one (**5**) To a round bottom flasj was added **3** (0.340 g, 1.95 mmol), **4** (0.417 g, 2.15 mmol), and dry dimethylformamide (DMF) (45 mL). The flask was equipped with a condenser and the mixture was stirred at reflux for 4.5 h, under an Argon atmosphere. The solvent was removed with a stream of nitrogen and mild heating. The crude product was purified by column chromatography on silica gel, using a 1:2 hexane: ethyl acetate mobile phase to give **5** as a dark violet solid (0.160 g) in 23% yield. ^{1}H NMR (400 MHz, DMSO-d6): δ = 8.50 (s, 1H), 8.05 (d, J = 8.1 Hz, 1H), 7.60 (dd, J = 9.4, 2.4 Hz, 2H), 6.79 (dd, J = 9.1, 2.8 Hz, 1H), 6.61 (d, J = 2.7 Hz, 1H), 6.22 (s, 1H), 5.50 (t, J = 5.7 Hz, 1H), 4.71 (d, J = 5.6 Hz, 2H), 3.47 (q, J = 6.9 Hz, 4H), 1.15 (t, J = 7.0 Hz, 6H). ^{13}C NMR (400 MHz, DMSO-d6): δ = 182.33, 152.17, 151.15, 146.89, 146.76, 138.87, 131.94, 131.28, 128.32, 124.60, 125.41, 124.60, 121.04, 110.61, 104.91, 96.39, 63.10, 44.90, 12.91.

Synthesis of 9-Diethylamino-5-oxo-5H-benzo[a]phenoxazine-2-carboxaldehyde (**6**), NR-Al. Compound **5** (0.160 g, 0.458 mmol) was dissolved in dry dichloromethane (70 mL) in a round bottom flask. A magnetic stir bar was added and the solution was placed under an Argon atmosphere. Pyridinium chlorochromate (0.197 g, 0.916 mmol, Frontier, 98%) (PCC) was next added portion-wise over 1 h. The reaction mixture was stirred at room temperature overnight under Argon and quenched when thin layer chromatography showed complete oxidation of the alcohol. Excess PCC was quenched by slowly adding isopropanol (17 eq) and stirring for an additional 30 min. The solvent was removed by rotary evaporation and the resulting solid was dissolved in deionized water and extracted with ethyl acetate. The combined organic fractions were dried over anhydrous sodium sulfate and concentrated under vacuum. The crude product was purified by column chromatography on silica gel using 1:1 hexane:ethyl acetate as the mobile phase, giving **6** as a purple solid (0.041 g) in 29% yield: ^{1}H NMR (400 MHz, DMSO-d6): δ = 10.27 (s, 1H), 9.07

(dd, J = 2 Hz, 1H), 8.30 (d, J = 8 Hz, 1H), 8.15 (dd, J = 2 Hz, 1H), 7.71 (d, J = 9 Hz, 1H), 6.91 (dd, J = 3 Hz, 1H), 6.72 (d, J = 3 Hz, 1H), 6.39 (s, 1H), 3.54 (q, J = 7 Hz, 4H), 1.19 (t, J = 7 Hz, 3H). ^{13}C NMR (400 MHz, DMSO-d6): δ = 193.72, 181.51, 152.91, 151.79, 147.20, 138.15, 137.62, 134.74, 132.54, 131.70, 129.00, 126.54, 125.15, 111.35, 105.53, 96.49, 45.06, 29.48, 12.94. MS calculated for $C_{21}H_{18}O_3N_2$: 346.37922, found: 346.37920.

3.3.2 Molecular structure

The molecular structure of the newly synthesized NR-Al was confirmed by ^{1}H NMR, ^{13}C NMR and high-resolution mass spectrometry using instrumentation described previously (**section 3.2.1**). NMR's and MS can be found in **Appendix A**.

^{1}H NMR (400 MHz, DMSO-d6): δ = 10.27 (s, 1H), 9.07 (dd, J = 2 Hz, 1H), 8.30 (d, J = 8 Hz, 1H), 8.15 (dd, J = 2 Hz, 1H), 7.71 (d, J = 9 Hz, 1H), 6.91 (dd, J = 3 Hz, 1H), 6.72 (d, J = 3 Hz, 1H), 6.39 (s, 1H), 3.54 (q, J = 7 Hz, 4H), 1.19 (t, J = 7 Hz, 3H). ^{13}C NMR (400 MHz, DMSO-d6): δ = 193.72, 181.51, 152.91, 151.79, 147.20, 138.15, 137.62, 134.74, 132.54, 131.70, 129.00, 126.54, 125.15, 111.35, 105.53, 96.49, 45.06, 29.48, 12.94. MS calculated for $C_{21}H_{18}O_3N_2$: 346.37922, found: 346.37920.

3.3.3 NR-Al Fluorescence Spectra

Static fluorescence excitation and emission spectra of NR-Al (1 μM) in DMSO solution are shown in **Figure 3.3A**. The dye is most efficiently excited near 580 nm and emits most strongly near 645 nm. Static spectra of the synthesized NR-Al were compared to that of commercial Nile Red under identical experimental conditions, **Figure 3.3B**. The emission spectrum of the former is shifted ~ 18 nm to the red from the latter.

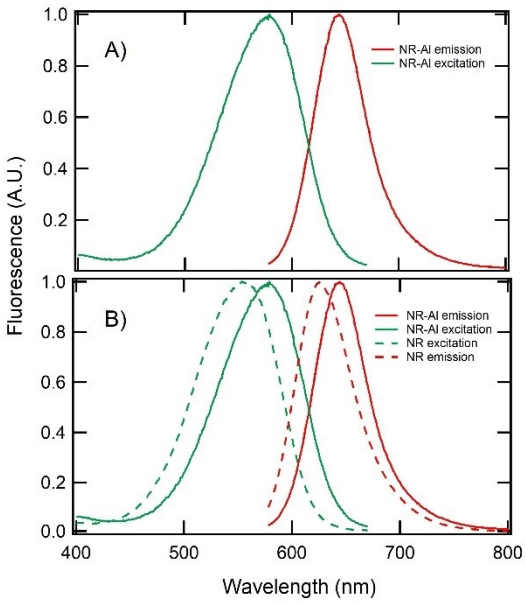

Figure 3.3 A) Normalized fluorescence excitation (green) and emission (red) spectra of 1 µM NR-Al in DMSO. **B)** Normalized fluorescence excitation (green) and emission (red) spectra of 1 µM Nile Red (NR) and 1 µM (NR-Al) in DMSO. The absorbance and emission spectra of the newly synthesized derivative of Nile Red are shifted ~24 nm and ~18 nm respectively to higher wavelengths compared to the commercial Nile Red**.**

3.4 Conclusion

A new reactive NR-Al molecular probe was synthesized in six steps based on the previous synthesis of Nile Red. ^{1}H and ^{13}C NMR's, and high-resolution mass spectrometry confirmed the molecular structure of the synthesized dye. The added aldehyde moiety on the Nile Red chromophore shifted the fluorescence emission spectrum ~18 nm to the red compared to commercial Nile Red in DMSO. This new form of NR will allow the probing of *in situ* aldol reactions via spectral changes in its fluorescence spectrum upon aldol reaction to obtain important initial catalytic activity of heterogeneous catalysts. NR-Al emission in the visible region (~645 nm) will enable and facilitate an array of single molecule studies of aldol reactions. Such studies are critical in understating structural and chemical differences of heterogeneous catalysts at nanoscales to advance their utility for industrially eco-friendly processes.

Chapter 4 - Fluorescence Spectroscopy Studies of Crossed Aldol Reactions: A Reactive Nile Red Dye Reveals Catalyst-Dependent Product Formation

manuscript drafted

Distribution of Work

I synthesized the dye used in these experiments and did much of the characterization. Dr. Man Zhang provided her synthetic expertise in proposing a similar reaction mechanism to get the dye of interest. Abdulhafiz Usman synthesized one of the catalysts used in these studies and did much of the catalyst characterization.

4.1 Introduction

Aldol reactions represent common and widely used synthetic routes to carbon-carbon bond formation via the coupling of, for example, an aldehyde and a ketone. The synthesis of pharmaceuticals, industrial feedstocks, commodity chemicals, and biomass-derived renewable liquid fuels frequently involve aldol reactions. These reactions are most often catalyzed by homogeneous catalysts comprising solutions of strong base (i.e., hydroxide)[15] or transition-metals.[138] However, homogeneous catalysts can be difficult to recover and reuse, producing excess waste and leading to increased cost. Heterogeneous catalysts are now being widely explored as a means to overcome these difficulties.[31] [32, 33]

Silica-based materials form an important class of porous solids now being investigated for use in heterogeneous catalysis of aldol reactions.[25, 139, 140] Catalytic sites are readily incorporated

into porous silica by addition of appropriate transition metals[35],[36] or acidic and basic moieties[37, 141, 142] during materials synthesis. For example, alkali or alkaline earth metals may be incorporated into the silica to form Brønsted base sites,[35, 36, 42] while the silanol groups intrinsic to the silica act as Brønsted acid sites.[26, 38] Bifunctional materials that incorporate both acid and base sites have been found to be particularly effective in catalyzing aldol condensation reactions.[34-36] The base sites appear to best catalyze the initial aldol addition step, forming an alcohol product, while a combination of base and weak acid sites in close proximity to each other catalyze the subsequent dehydration to obtain the final olefin product.[38, 41]

It is generally accepted that both the concentration and strength of acid and base sites associated with the heterogeneous catalyst define its activity.[143] These parameters are most commonly determined *ex situ* by methods such as temperature programmed desorption of ammonia and carbon dioxide.[144-147] The results of such studies afford little direct information on the *in situ* acidity and basicity of the catalytic sites, which are certain to vary with the solvent employed and the temperature at which the reaction is run, among other factors. Furthermore, the properties of the individual catalyst particles are expected to be intrinsically variable. To overcome some of the limitations of *ex situ* studies, fluorogenic reactions have been employed previously as a means to characterize catalyst activity *in situ* for a number of processes.[46-48] Many such studies have been performed by ensemble spectroscopic methods, but when highly fluorescent reactants and products are involved, the reactions can even be followed at the single molecule/single turnover level.[52-54, 148] While fluorescence has been used previously to follow aldol reactions,[58, 59] no such studies have been reported at the single molecule level to date. The dearth of single molecule studies likely stems from the lack of suitable dyes designed to undergo aldol reactions while also remaining sufficiently fluorescent for detection at the single molecule level.

This chapter demonstrates the use of NR-Al (synthesis reported in **Chapter 3**) in solution-phase ensemble spectroscopic studies of the heterogeneous catalysis of crossed aldol reactions. The Nile Red chromophore was selected for use because it is now widely employed in single molecule detection, spectroscopy, and tracking studies.[128-130] Because its lowest energy electronic transition involves an intramolecular charge transfer process,[149] its spectrum is highly dependent on its surroundings.[62] It was hypothesized that subtle changes to its structure occurring during an aldol reaction will also lead to detectable changes in its fluorescence spectrum. The performance of NR-Al was compared to that of a commercially available 3-perylenecarboxaldehyde. The heterogeneous catalyst employed was Mg-Zr-Cs doped silica (Mg-Zr-Cs/SiO_2) and its performance was compared to that of commercially available MgO. The activities of these two catalysts were compared to that of fumed silica. The occurrence of an aldol reaction was verified by high performance liquid chromatography (HPLC), and by HPLC-mass spectrometry (HPLC-MS). Changes in dye fluorescence observed during the reaction were recorded and used as a simple, real-time, *in situ* method for following reaction progress. The new NR-Al dye reported, and the results obtained in ensemble studies of aldol reactions will be useful to others seeking *in situ* methods to characterize the activity of heterogeneous catalysts. They will also facilitate future studies of catalyst activity at the single particle and single reaction event level via the implementation of single molecule spectroscopic methods.

4.2 Experimental Considerations

4.2.1 Materials

Except as indicated below, all solvents, starting materials, and reagents employed in the synthesis of NR-Al and Mg-Zr-Cs/SiO_2 were obtained from commercial sources and used as received.

4.2.2 Methods for Heterogeneous Catalysts

Preparation of Mg-Zr-Cs/SiO_2 catalyst. Fumed silica (Sigma-Aldrich, 99.8%) was calcined in flowing air at 500 °C for 3 h in a furnace (Barnstead F1500). The silica was then impregnated with aqueous solutions of $Mg(NO_3)_2 \cdot 6H_2O$, $ZrO(NO_3)_2 \cdot xH2O$ and $CsNO_3$ (Sigma-Aldrich) to yield particles incorporating theoretical loadings of magnesium, zirconium, and cesium at 0.025 wt.%, 0.033 wt.% and 13 wt.%, respectively. The aqueous mixture was subsequently immersed and sonicated at 40 °C for 24 h, followed by drying in an oven overnight at 90 °C. The catalyst was further calcined in flowing air at 500 °C for 3 h and was then stored in a desiccator for fewer than 3 days prior to use.

Catalyst structural characterization. X-Ray diffraction (XRD) patterns of the as-synthesized Mg-Zr-Cs/SiO_2, the commercially available MgO (Nanoscale Materials), and fumed silica were obtained using a desktop X-ray diffractometer (Rigaku Miniflex II). Transmission electron microscopy (TEM) images were acquired using a FEI Tecnai G2 Spirit BioTWIN microscope operating at 120 kV. Samples were prepared by dispersing them in ethanol, sonicating them, and then depositing them on a microgrid before imaging. Scanning electron microscopy

(SEM) images were obtained using a Hitachi S-3500N microscope operating at 20 kV. The catalyst samples were sputter coated with palladium before imaging.

BET surface area and pore size distribution measurements were made on a Micromeritics ASAP 2020 Surface Area and Porosity Analyzer. Samples were first dehydrated in a 1430 series VWR vacuum oven for 24 h at 150 ºC and < 77 Torr. To avoid undesirable interactions with atmospheric moisture, samples were kept in a humidity-free environment in a Sanplatec Dry Keeper Auto Desiccator Cabinet. Prior to surface area and porosity measurements, all samples went through an outgassing step for 12 h at 350 ºC under vacuum. Nitrogen sorption isotherms were collected at 77 K over a relative pressure range of 0.05 to 0.995 (p/p_0); measured every 120 min. Mesopore-size distribution was evaluated by the nitrogen desorption isotherm and by the BJH method.[150] Total surface area was calculated by the BET method.[103] Total pore volume was determined by the amount of nitrogen adsorbed at a relative pressure of 0.99 (p/p_0).

Catalyst chemical characterization. Elemental analysis was accomplished by energy-dispersive X-ray spectroscopy (EDS) employing an Oxford detector (< 135 eV). The elemental composition of the catalysts was also determined using a Varian 720-ES inductively coupled plasma-optical emission spectrometer (ICP-OES). Samples were digested in nitric acid for this analysis. X-ray photoelectron spectroscopy (XPS) data were acquired using a Thermo Scientific K-alpha$^+$ XPS with a monochromatic Al Kα X-ray source (1486.6 eV). XPS spectra were acquired using a 400 μm spot size, 50.0 eV pass energy, and 0.100 eV step size. The binding energies were corrected for charge shifts using the C (1s) peak of adventitious carbon at 284.8 eV as a reference.[41] Deconvolution of the XPS data was done using OriginPro software.

The acid-base properties of the catalysts were determined by temperature-programmed desorption (TPD) of CO_2 and NH_3 (Altamira Instruments AMI-200). For CO_2 TPD, 150 mg of

catalyst was placed in a quartz tube and treated in helium flow at 450 °C for 1 h, with a heating rate of 10 °C/min. After cooling to 50 °C, a 10% CO_2-He mixture was passed over the samples for 30 min followed by a purge with pure helium until the baseline became stable. Desorption of CO_2 was accomplished by exposing the sample to a helium flow while heating to 500 °C at a rate of 10 °C/min. The same process was employed for NH_3 TPD using a 1% NH_3-He mixture. The desorption profile for both gases was recorded using a thermal conductivity detector.

4.2.3 Methods for Aldol Reactions

General procedure for crossed aldol reactions. The experimental conditions for aldol reactions were obtained from Sakthivel et al.[151] A stock solution of NR-Al (7 mM) was prepared in DMSO (Fisher) and later used in the preparation of diluted solutions for aldol reactions. All experiments employed either ACS grade acetone (Fisher) or GC grade acetophenone (Sigma-Aldrich, > 99%) as the ketone. The ketones were each dissolved in DMSO in a 1:4 (v/v) ratio. Fluorescence measurements of the reaction kinetics employed low (1 μM) NR-Al concentrations, while HPLC and HPLC-MS analyses were performed for reactions using high (1 mM) NR-Al concentrations. The performance of the Mg-Zr-Cs/SiO_2 catalyst was compared to that of commercially available MgO, and fumed silica. The latter served as a control. Aldol reactions and controls employed a catalyst loading of 3.07 mg/mL and reaction volumes of either 3.250 mL or 1.625 mL. The reactions were stirred at room temperature for various times, as specified below. Aldol reactions are known to depend on temperature, but such effects were excluded from the present investigations. Therefore, heat transfer from the magnetic stir plate into the reaction mixture was prevented by placing an insulating material between the stir plate and the reaction cell.

Crude products from the aldol reactions employing 1 mM NR-Al were prepared for HPLC-MS characterization by adding one volume equivalent of saturated aqueous NH_4Cl to the mixture and then extracting 2-3 times with ethyl acetate (Fisher). The combined organic fractions were dried over anhydrous sodium sulfate (Fisher) and concentrated under vacuum. The products were dissolved in 3:2 (v/v) HPLC grade acetonitrile (Fisher) and HPLC grade water (Fisher) and analyzed using an Acquity Ultra Performance HPLC-MS (Waters). The HPLC mobile phase gradient employed a water-acetonitrile mixture and a C18 reversed phase silica column (Cortecs). Products eluting from the column were detected by their UV absorbance at 230-300 nm. MS detection employed an electrospray ionization source. An Ultimate 3000 HPLC (Thermo Fisher) with absorbance detection at 575 nm was employed for quantitative analysis of the aldol products. A water-acetonitrile mobile phase gradient and a C18 reversed phase silica column (Thermo Fisher) were also employed here.

Fluorescence studies of crossed aldol reactions. Fluorescence spectra were acquired on a FluoroMax-2 spectrophotometer (Jobin Yvon Spex) using a Xenon lamp (150 W) as the light source. Aldol reactions were run in a quartz fluorimeter cell (Starna Cells) with a 10 mm pathlength. The cell was sealed with a Teflon cap and parafilm to prevent solvent evaporation during the reaction. Excitation and emission spectra were acquired primarily from 1 μM NR-Al solutions. While spectra were also acquired from 1 mM NR-Al solutions, these were severely distorted by inner filter effects and were not used in any spectroscopic analyses. The emission spectrum of NR-Al was recorded from 578 to 800 nm, while exciting at 575 nm. The progress of the aldol reactions was monitored in real time by recording fluorescence spectra at various time intervals during the reaction.

As described in Supporting Information, the utility of the newly synthesized NR-Al dye in studies of crossed aldol reactions was compared to that of a commercially available 3-perylenecarboxaldehyde dye (TCI, > 95%). In this case, 1 μM 3-perylenecarboxaldehyde solutions were employed. The 3-perylenecarboxaldehyde emission spectrum was recorded from 470 to 800 nm, while exciting at 465 nm.

Synthesis of NR-Al. The full synthesis of the dye used in these studies was described in detail in **Chapter 3**.

4.3 Results and Discussion

4.3.1 Mg-Zr-Cs Doped Silica Catalyst

Catalyst structural characterization. The XRD patterns obtained from fumed silica, and the Mg-Zr-Cs/SiO_2 and MgO catalysts are shown in **Figure 4.1.** Broad peaks centered near 2 θ = 21° were observed for the Mg-Zr-Cs/SiO_2 catalyst and SiO_2, as is characteristic of silica-based materials;[36] the weaker broad peak of the former confirms that the silica structure has been modified by impregnation of the metal nitrates.[36, 42, 152] Hexagonal cesium nitrate was also observed in the Mg-Zr-Cs/SiO_2 pattern, as evidenced by the sharp peaks centered at 2 θ = 19.9, 28.2, 34.8, 40.3, 45.4 and 50°, while no magnesium nitrate or zirconium nitrate species were detected. The latter suggests these components are well dispersed in the silica matrix.[42] Sharp peaks at 2 θ = 42.8 and 62.1°, and weaker peaks at 2 θ = 37, 74.7 and 78.7° were observed in the MgO XRD pattern and were attributed to the presence of its cubic phase.[153]

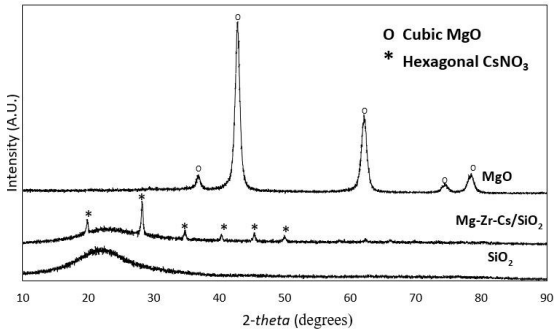

Figure 4.1 X-Ray diffraction patterns from fumed silica along with Mg-Zr-Cs/SiO_2 and MgO catalysts. Data acquired by Abdulhafiz Usman, Dept. of Chemical Engineering, Kansas State University.

SEM and TEM images of the catalysts are shown in **Figure 4.2**. SEM images of the MgO catalyst and fumed silica (**Figures 4.2A,C**) show agglomerated spherical particles of various sizes. When Mg, Zr, and Cs were loaded into the silica, the catalyst became more aggregated, as evidenced by the TEM image in **Figure 4.2F**. The surface area and porosity results for these materials are summarized in **Table 1**. The corresponding nitrogen sorption isotherms and pore size distributions are shown in **Figure 4.3**.

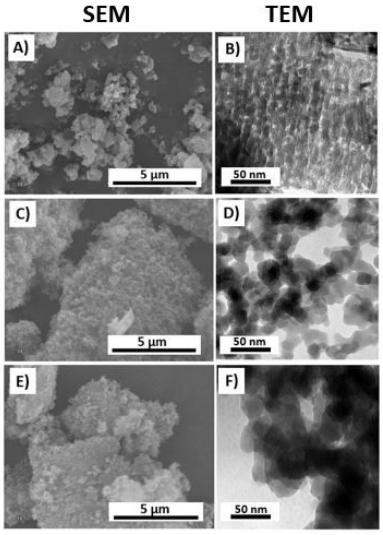

Figure 4.2 A), B) SEM and TEM images of commercial MgO catalyst particles. **C), D)** SEM and TEM images of SiO_2 particles. **E), F)** SEM and TEM images of Mg-Zr-Cs/SiO_2 particles. Data acquired by Abdulhafiz Usman, Dept. of Chemical Engineering, Kansas State University.

Table 1 Chemical and structural properties of the catalysts

Catalysts	Basic site density (μmol CO_2/g)	Acid site density (μmol NH_3/g)	Metal content (%)	Total Surface $Area_{BET}$ (m^2/g)	Average Pore $Diameter_{BJH}$ (nm)	Total Pore Volume (cm^3/g) at p/p_0=0.99
MgO	820	791	Mg=53	119.16	7.6	0.3170
SiO_2	0	0	-	193.85	11.8	0.4986
$MgZrCs/SiO_2$	252	143	Cs=13, Mg<0.1 Zr<0.1	87.42	29.5	0.9441

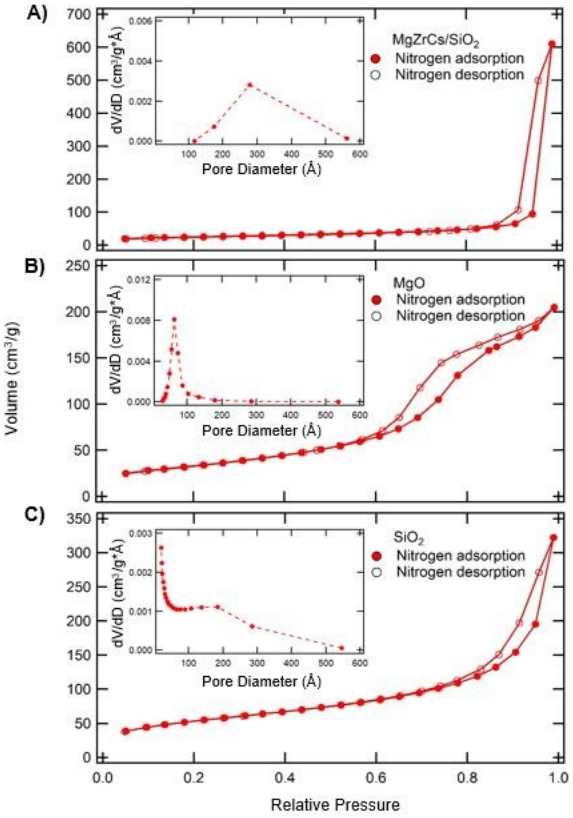

Figure 4.3 Nitrogen sorption isotherms of mesoporous Mg-Zr-Cs/SiO_2 **(A)**, MgO **(B)**, and SiO_2 **(C).** The insets correspond to the pore-size distribution calculated from the desorption isotherms. Data acquired by Murilo Toledo, Dept. of Chemical and Petroleum Engineering, University of Kansas.

Catalyst chemical composition. EDS did not detect Mg or Zr on the Mg-Zr-Cs/SiO_2 catalyst due to their low loadings of 0.025 wt.% and 0.033 wt.%, respectively, while a Cs content of 12.93 wt.% was measured, in agreement with the theoretical loading of 13 wt.%. ICP-OES

measurements detected all three metals. In this case, the metal contents were determined to be 0.021 ± 0.001 wt.% for Mg, 0.0051 ± 0.0003 wt.% for Zr, and 11.4 ± 0.4 wt.% for Cs. The error bars give the 95% confidence-intervals with n = 6 for Mg and Zr, and n = 9 in the case of Cs. While the values obtained for Cs and Mg were close to their theoretical loadings, Zr was lower than expected. This may be due to competition between the metals for active sites on the silica.[45] The Mg content in commercial MgO was 53.18 wt.%.

XPS spectra (**Figure 4.4**) show the Cs (3d) peaks for the Mg-Zr-Cs/SiO_2 catalyst, but Mg and Zr were not detected due to their low loadings. The Si (2p) peak is also observed for fumed silica, the Mg (1s) peak for MgO, and the O (1s) peak for both catalysts and pure silica. The binding energies for the active components in the catalysts were 724.6 eV - 742.7 eV for suboxides of Cs in Mg-Zr-Cs/SiO_2 and 1304.2 eV for Mg-O in MgO.

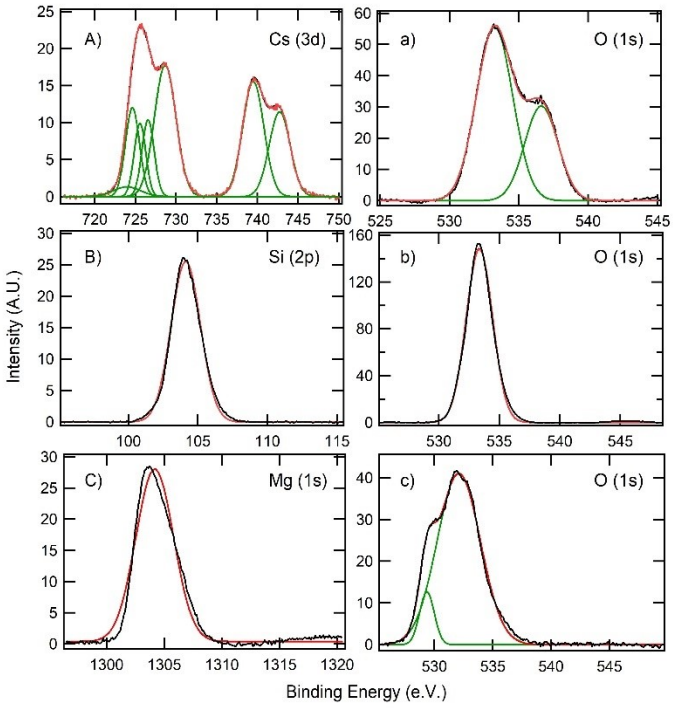

Figure 4.4 The XPS spectra of Mg-Zr-Cs/SiO_2 catalyst: The Cs (3d) peak (A), the 725.6 and 739.8 eV correspond to Cs $3d_{5/2}$ and Cs $3d_{3/2}$ from the Cs^+ ion.[154] The binding energies at 724.6 eV, 725.5

eV, can be attributed to Cs_2O_2,[155] and Cs_2O.[156] While those greater than 726 eV can be attributed to suboxides of Cs.[157] The O (1s) peak (a), the binding energy at 533.2 eV is due to Si-O (Si-O-Si, Si-O-H) from SiO_2 support.[158] The XPS spectra of SiO_2: The Si (2p) peak (B), the 104.1 eV is due to Si-O_2.[159] The O (1s) peak (b), the binding energy at 533.2 eV is due to Si-O (Si-O-Si, Si-O-H) form SiO_2 support.[158] The XPS spectra of MgO catalyst: The Mg (1s) peak (C), the binding energy at 1304.2 eV is due to Mg-O.[160] The O (1s) peak (c), the binding energy at 529.4 eV corresponds to the lattice oxygen O^{2-}. The higher binding energy at 532.0 eV can be attributed to adsorbed oxygen and/or weakly bound oxygen, or to surface hydroxyl species.[161, 162] Data acquired by Dr. Balamurugan Balasubramanian, Nebraska Nanoscale Facility: National Nanotechnology Coordinated Infrastructure and the Nebraska Center for Materials and Nanoscience, University of Nebraska-Lincoln.

The density of base and acid sites on the catalysts were quantified by stepwise temperature-programmed desorption (TPD) of CO_2 and NH_3. The results of these experiments are shown in Supporting Information (**Figure 4.5**). A higher desorption temperature indicates stronger basicity or acidity, while the area under each desorption peak is proportional to the number of active sites.[163] The desorption profile for the control, SiO_2, showed no base or acid sites while that of the Mg-Zr-Cs/SiO_2, and MgO catalysts were found to have base and acid sites of various strengths.

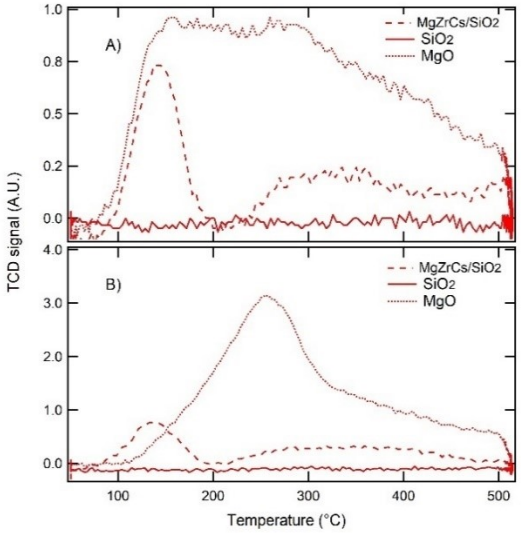

Figure 4.5 (A) CO_2 and **(B)** NH_3 temperature programmed desorption curves of Mg-Zr-Cs/SiO_2, SiO_2 and MgO catalysts. Higher desorption temperatures indicate stronger basicity or acidity while the area under the desorption peaks provides the number of active sites.[163] Data acquired by Abdulhafiz Usman, Dept. of Chemical Engineering, Kansas State University.

The CO_2 desorption profile for Mg-Zr-Cs/SiO_2 showed prominent peaks in the 75 - 175 °C range (weak base sites) and the 275 - 475 °C range (medium strength base sites), while for MgO, a broad CO_2 desorption peak in the 75 - 475 °C range (weak-medium base sites) was observed. The NH_3 desorption profile for Mg-Zr-Cs/SiO_2 also showed one peak in the 75 - 175 °C range (weak acid sites) and a second, broader peak in the 250 - 475 °C range (medium strength acid sites). The commercial MgO catalyst showed a prominent desorption peak in the 200 - 300 °C range, corresponding to medium strength acid sites. The corresponding base and acid site densities determined from **Figure 4.5** are shown in **Table 1**.

Elemental analyses and TPD data suggest that the metal nitrates in the Mg-Zr-Cs/SiO_2 catalyst aid in enhancing the base and acid properties of the silica support. The differences in strength and quantity of these sites within the catalyst led to differences in aldol product formation compared to the MgO catalyst, as will be discussed below.

4.3.2 Ensemble Fluorescence Studies of Aldol Reactions

***Aldol reactions*.** Aldol reactions may be catalyzed by either base or acid.[142, 164, 165] In this work, Mg-Zr-Cs/SiO_2 having substantial base and acid sites was employed to catalyze reactions of NR-Al (1 μM) in DMSO with acetone or acetophenone. The results obtained were compared to those of reactions catalyzed by commercially available MgO, while fumed silica served as a control. All reactions were conducted by stirring at room temperature.

Mg-Zr-Cs/SiO_2 was chosen due to the extensive literature showing that aldol reactions are significantly enhanced when bifunctional catalysts incorporating both weak acid and base sites are employed.[38, 41, 151] It is believed that basic sites catalyze the aldol addition step, forming an alcohol, while acidic sites catalyze subsequent condensation to form the olefin product, as shown in the

scheme in **Figure 4.6**. In Mg-Zr-Cs/SiO_2, the cesium nitrate is believed to provide the base sites and some acid sites, while SiOH groups on the silica likely provide additional acid functionality. The magnesium and zirconium aid in improving and maintaining the performance of the catalyst.[35, 45]

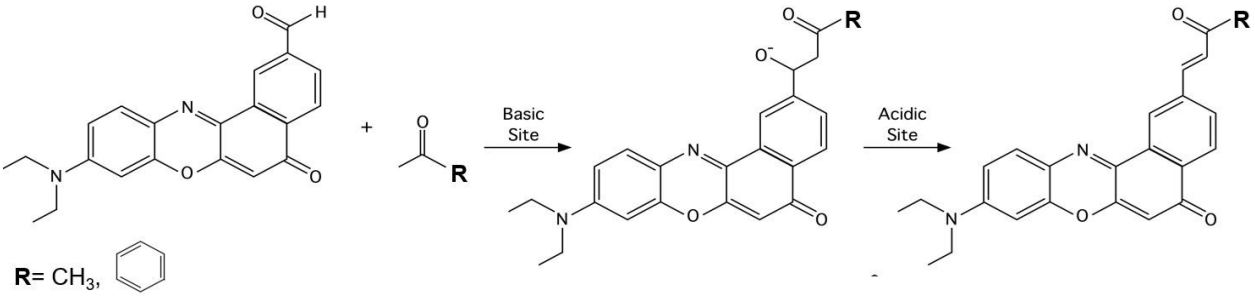

Figure 4.6 Scheme of base-catalyzed aldol addition reactions, followed by acid-catalyzed dehydration reactions to form the aldol condensation products for reactions of NR-Al **(6)** with ketones having **R** = methyl or phenyl.

The progress of crossed aldol reactions was monitored in real time by recording a series of fluorescence spectra at different time intervals. **Figure 4.7** depicts the fluorescence spectra obtained. These data show notable differences in how the spectra evolve in time when either Mg-Zr-Cs/SiO_2 or MgO was used as the catalyst.

When Mg-Zr-Cs/SiO_2 was employed, a progressive blue shift in the emission spectrum of the dye was observed as the reaction proceeded. Aldol reactions with acetone and acetophenone showed gradual blue shifts of 16 nm and 8 nm, respectively, over the time the data were acquired (see **Figures 4.7A, D**). The gradual shift in fluorescence exhibited by the dye is concluded to result from formation of two different products, the addition and condensation products, in the presence of residual starting material. Note that the reaction between NR-Al and acetone catalyzed by Mg-Zr-Cs/SiO_2 was faster than the others. The spectral shift to the blue appeared to be complete by 2 h in this case. In contrast, the reaction between NR-Al and acetophenone took at least 8 h for the

full spectral shift to develop. The differences in rates for aldol reactions using acetone and acetophenone is attributable to structural differences in these ketones. The reaction with acetone may be faster due to the presence of two alpha carbons, providing two acidic hydrogens that may make the first step of the reaction more kinetically favored. Alternatively, the incorporation of the phenyl group on the acetophenone precursor may make its reaction with NR-Al more sterically hindered and slower.

When MgO served as the catalyst, NR-Al reactions with both ketones led to the appearance of a new peak that grew in time as the reaction progressed, giving an apparent isoemissive point in the spectra (see **Figures 4.7B, E**). In both cases, the original fluorescence peak centered at ~ 642 nm subsided, while a new peak centered at ~ 615 nm grew over time. The appearance of two peaks and an isoemissive point are consistent with the presence of two different species in the reaction mixture, likely NR-Al and a new product. As in the case of reactions catalyzed by Mg-Zr-Cs/SiO_2, the reaction with acetone was quicker than when acetophenone was employed. Reaction mixtures with SiO_2 resulted in no apparent fluorescence shift, as shown in **Figures 4.7C, F**, suggesting no reaction occurred. This may be attributed to insufficient base or acid sites in the SiO_2 to catalyze the reaction.[44, 166] Note that the TPD analysis shown in **Figure 4.5** revealed no detectable base or acid sites on the silica.

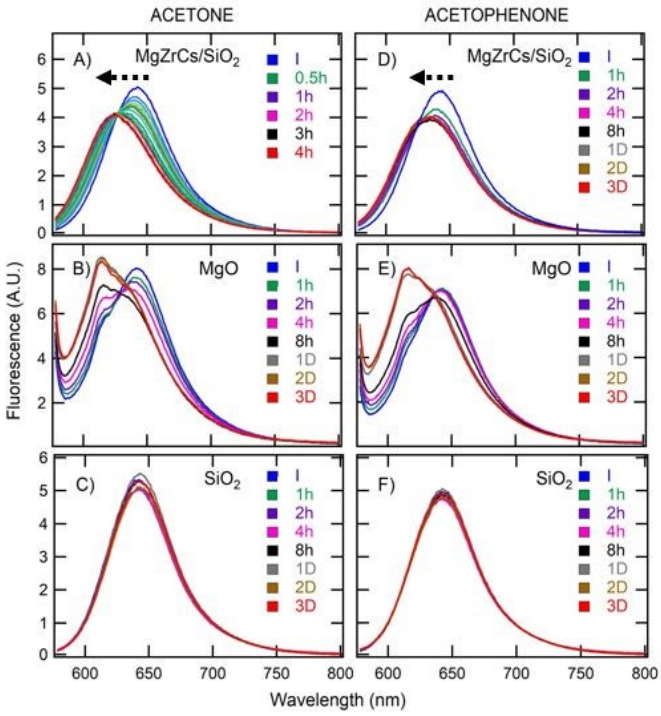

Figure 4.7 A) - C) Fluorescence from NR-Al as a function of time in the presence of the catalysts listed with acetone employed as the ketone. **D) - F)** Fluorescence from NR-Al as a function of time in the presence of the catalysts listed with acetophenone employed as the ketone. The fluorescence was excited at 575 nm in each case. DMSO was employed as the solvent. All reactions were stirred at room temperature**.**

4.3.3 HPLC and LC-MS Studies of Aldol Product Formation

The differences in spectral behavior for the Aldol reactions catalyzed by Mg-Zr-Cs/SiO_2 and MgO were attributed to the formation of different products. Analytical HPLC and HPLC-MS were employed to confirm that different products were formed in each case and to help identify these products. Representative chromatograms are provided in **Figure 4.8** and the mass spectra used to assign each peak to the different products are given in **Figure B.1.** As noted above, these reactions employed a higher concentration of NR-Al (1mM) to facilitate product recovery and detection. The aldol reactions in this case were run for an arbitrary time of 3 days (see *kinetic measurements* below for further discussion).

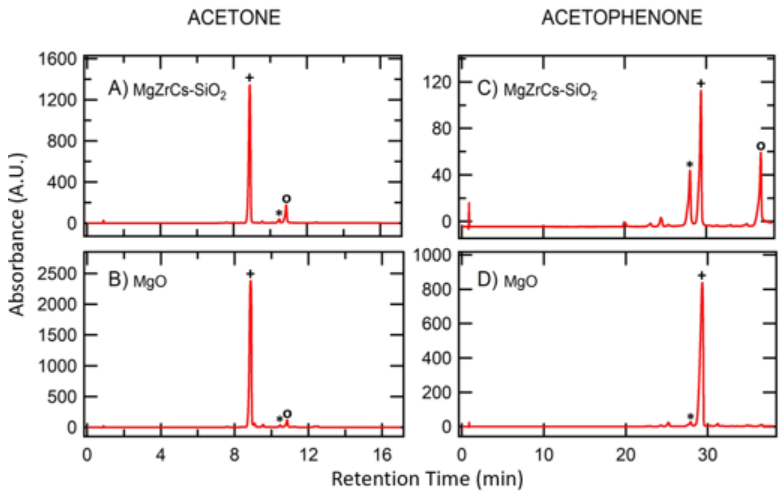

Figure 4.8 HPLC chromatograms (575 nm absorbance) of aldol products from 3-day reactions of NR-Al (1mM) with acetone **(A, B)**, and acetophenone **(C, D)** in the presence of Mg-Zr-Cs/SiO_2 or MgO at room temperature. The chromatograms show the un-reacted NR-Al (*), the aldol addition product (+), and the aldol condensation product (o). For **A, B,** the mobile phase gradient comprised H_2O and acetonitrile mixtures at 0.800 mL/min flow rate with the following compositions: 0-10 min: 95-40% H_2O; 10-15 min: 40-20% H_2O; 15-17 min: 20% H_2O. For **C, D** the mobile phase compositions were: 0-35 min: 95-45% H_2O; 35-36 min: 45-20% H_2O; 36-38 min: 20% H_2O. A Thermo Scientific Hypersil GOLD C18 column (100 X 3 mm^2, 3 µm particle size) was employed.

Chromatograms obtained from aldol reactions employing Mg-Zr-Cs/SiO_2 as the catalyst with acetone as the reactant were dominated by two peaks (see **Figure 4.8**). HPLC-MS data allowed these two peaks to be assigned to the addition and condensation products (see **Figure B.1.**). The aldol addition product for this reaction gave a peak at 405 atomic mass units (amu, m/z) in the MS data, as expected, while the aldol condensation product gave a peak at 387 amu, as expected. Note that the mass resolution in this instrument is ± 1 amu. Separations performed using starting material alone revealed that one of the minor peaks was produced by residual NR-Al. When acetophenone was employed as the reactant, the chromatograms obtained incorporated three peaks (see **Figure 4.8C**). HPLC-MS results (see **Figure B.1.**) allowed assignment of these peaks to the addition and condensation products, and residual NR-Al. The peak assigned to the aldol addition product gave a peak at 467 amu, while the condensation product produced a peak at 449

amu. In contrast, when MgO was employed as the catalyst, chromatograms obtained from both the acetone and acetophenone reaction mixtures were dominated by a single peak (see **Figures 4.8B, D**). HPLC-MS data obtained revealed these peaks were due to predominant formation of the addition products and very little of the condensation products. The acetone addition product gave a peak at 405 amu, with the aldol condensation product yielding a peak at 387 amu. With acetophenone, the aldol addition product gave peaks at 467 amu and 449 amu for the addition and condensation products, respectively. These results provide strong support for the conclusions drawn from the spectroscopic data. The relatively large amount of un-reacted NR-Al found in the reaction mixture with acetophenone when Mg-Zr-Cs/SiO_2 was employed as the catalyst provides support for the conclusion that the kinetics are slowed as a result of ketone structure. The much smaller NR-Al peak found when MgO was employed suggests it may be better than Mg-Zr-Cs/SiO_2 at catalyzing the first step of the aldol reaction, while the Mg-Zr-Cs/SiO_2 is better able to catalyze the subsequent condensation step. A more detailed discussion is given below.

It is believed that the HPLC and HPLC-MS results for aldol reactions run at the higher NR-Al concentration (1 mM) also reflect the products formed at the lower NR-Al concentration (1 μM) employed in the spectroscopic studies. Therefore, the isoemissive point observed in aldol reactions catalyzed by MgO are attributed to the presence of primarily the un-reacted NR-Al and the newly formed aldol addition product. Likewise, the gradual shift in the spectra observed from aldol reactions employing the Mg-Zr-Cs/SiO_2 catalyst (see **Figures 4.7A, C**) are attributed to the presence of time varying concentrations of un-reacted NR-Al, the aldol addition product, and the aldol condensation product.

4.3.4 Aldol Reaction Kinetics

The kinetics of the crossed aldol reactions were followed using the fluorescence data shown in **Figure 4.7**. For this purpose, the fluorescence signals in two spectral bands spanning 642 ± 5 nm and 615 ± 5 nm were obtained and plotted as a function of time. This method was chosen over the usual procedure of fitting the data to multiple Gaussian functions because the latter did not provide robust, easily interpreted results on the disappearance of NR-Al and the formation of products. **Figure 4.9** shows the results of this analysis. These data show a time-dependent decrease in the 642 nm band that is concluded to reflect consumption of NR-Al. Similarly, a time-dependent increase in the 615 nm band is observed that is interpreted to reflect appearance of the product(s). Note that control experiments employing fumed silica showed neither evidence for consumption of starting material nor appearance of product(s) (see **Figure 4.9C, E**).

The data in **Figures 4.7A, B** and **4.7D, E** were employed to determine the rate of disappearance of NR-Al and the rate of formation of aldol product(s). These rates were obtained by fitting the curves to single exponentials. The rates of disappearance of NR-Al in the reactions with acetone employing Mg-Zr-Cs/SiO_2 and MgO catalysts were determined to be 2.1 ± 0.2 h^{-1} and 0.4 ± 0.1 h^{-1}, respectively, while the rates of aldol product formation were found to be 3.0 ± 0.2 h^{-1} and 0.12 ± 0.02 h^{-1}, respectively. Similarly, the rates of disappearance of NR-Al in the reactions with acetophenone catalyzed by Mg-Zr-Cs/SiO_2 and MgO were 1.0 ± 0.1 h^{-1} and 0.08 ± 0.02 h^{-1}, respectively, while the rates of aldol product formation were 0.3 ± 0.1 h^{-1} and 0.08 ± 0.01 h^{-1}, respectively. Since the ketones were present at much higher concentrations than the NR-Al, these rates represent estimates of the pseudo-first-order rate constants for these reactions. It is noteworthy that HPLC-MS did not reveal significant self-condensation of acetone. The above

results show some complexities in interpreting the rates of aldol reactions using only fluorescence spectroscopy.

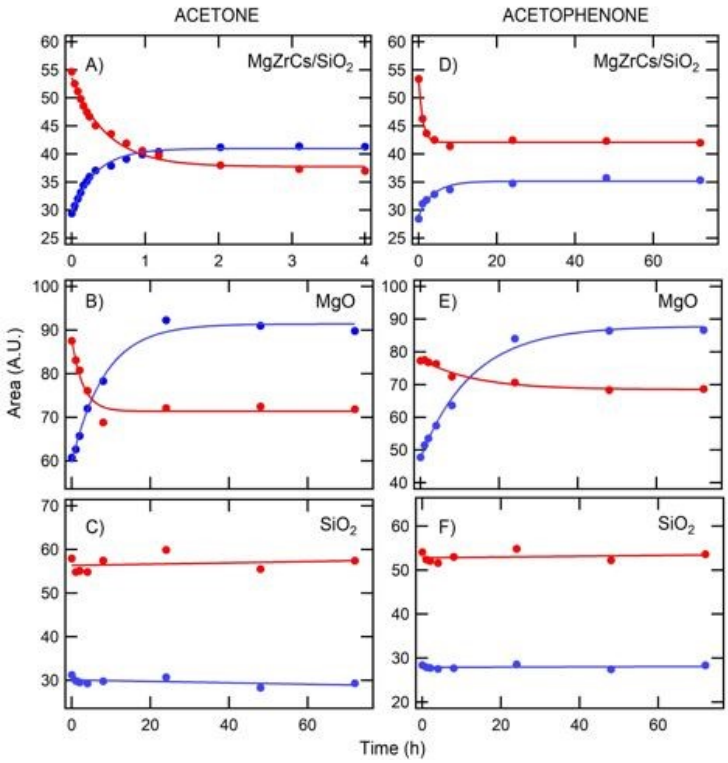

Figure 4.9 Fluorescence signals in bands spanning 642 ± 5 nm (red data points) and 615 ± 5 nm (blue data points) plotted as a function of time for crossed aldol reactions with acetone, **A)-C),** and acetophenone, **D)-F).** These data were obtained from Figure 4.8A-F. Data are given for reactions catalyzed by $MgZrCs/SiO_2$, **A), D),** as well as MgO, **B), E),** and the silica control, **C), F).** The solid lines have been added to better depict the trends in the data. Note that the NR-Al reaction with acetone catalyzed by $Mg\text{-}Zr\text{-}Cs/SiO_2$ is significantly faster than the others.

4.3.5 Catalyst Dependent Product Formation

The results given above show that the aldol reactions catalyzed by $Mg\text{-}Zr\text{-}Cs/SiO_2$ produced both addition products (alcohols) and condensation products (olefins). In contrast, those catalyzed by MgO produced primarily addition products and little condensation products. The fluorescence results shown in **Figure 4.7**, demonstrate that the nature of the NR-Al blue shift as the reaction progresses is diagnostic for catalyst activity. Catalysts that form a single product, the

alcohol, produce spectra incorporating an isoemissive point. Catalysts that produce both addition and condensation products yield fluorescence spectra that gradually shift to the blue. The observed differences in the two catalysts are attributed to differences in surface area, as well as differences in acid and base site densities and strengths. Since aldol condensation reactions involve two distinct reaction steps, these will be addressed separately below.

The likely mechanism for the addition reaction and the factors governing its rate will be discussed first. It is noteworthy that strong bases are by far the most common homogeneous catalysts used in aldol reactions.[15, 22, 23] Therefore, it is concluded that strong base sites on heterogeneous catalysts are likely to be important in initiating the reactions explored here. Indeed, the results shown in **Table 1** and in **Figure 4.5** demonstrate that MgO has a much greater density of base sites (820 vs 252 μmol CO_2/g in TPD experiments) and that the density of the stronger sites (CO_2 desorbed at 250 - 475 °C) is much greater than is the case for Mg-Zr-Cs/SiO_2 (326.7 vs. 86.6 μmol CO_2/g in TPD experiments) The strong base sites are best at abstracting acidic hydrogens on the alpha carbon(s) of the ketone. The nucleophilic enolate carbanion formed then attacks the electron-poor carbon of the aldehyde, forming the addition product. The literature on heterogeneous inorganic catalysts also suggests that the metal centers (M) can polarize the precursor carbonyls, increasing their reactivity.[34, 39] The greater density of strong base sites and the greater metal content of the MgO is thus consistent with the predominant formation of addition product.

The MgO catalyst was also found to have greater surface area than the Mg-Zr-Cs-SiO_2 materials (see **Table 1**). The greater base strength, greater base site density, and greater surface area of the MgO suggests product formation should be faster in reactions where it is employed as the catalyst. However, the results shown in **Figure 4.9** indicate these reactions are actually slower.

The apparently slower kinetics of the addition reaction in the case of MgO may be due to the reversibility of this reaction, with the retro-Aldol reaction also being relatively fast.

A common theme in the modern literature on heterogeneous aldol reactions is that bifunctional catalysts are best suited to formation of the condensation products.[26, 35, 39, 44] This prior work also demonstrates that weaker acid sites better catalyze condensation than do strong acid sites.[34, 38] Strong acid sites are believed to react with basic sites in close proximity, forming catalytically inactive ion pairs.[25, 37, 38] In contrast, weak acid sites are believed to remain active and can interact with the aldol addition products. The results shown in **Figure 4.5** demonstrate that Mg-Zr-Cs/SiO_2 incorporates more catalytically active weak acid sites (NH_3 desorbed at 75-175 °C) than does the MgO (NH_3 desorbed at 200-300°C). The improved catalytic activity of Mg-Zr-Cs/SiO_2 toward aldol condensation may be due to surface silanol groups intrinsic to the silica support as well as the presence of some water, which together facilitate proton exchange in the bifunctional catalyst.[38,41] These weak acid sites act to protonate the products of the addition reaction, catalyzing irreversible dehydration to form the condensation product (the olefin).[33, 39] It is this final step that is believed to lead to relatively fast and irreversible conversion of the addition reactants in the Mg-Zr-Cs/SiO_2 catalyzed reactions to condensation products.

While the model given above is most consistent with the present results, alternatives have also been discussed in the literature. For example, recent work claims that proton equilibration with the anion is fast and that addition product formation is the rate-limiting step.[167] While the addition reaction may be rate limiting, the present results are consistent with the conclusion that formation of the condensation product is critical to preventing the retro-aldol addition reaction from occurring. An alternative mechanism that has also been proposed is that the carbonyl on the aldehyde can be activated by protonation by the weak acid (Si-OH) sites. Nucleophilic attack of

the enolate formed by interaction of the ketone with the basic sites then forms the addition product which then loses water to yield the condensation product.[34] The authors state that by this acid-base cooperative mechanism, a strong base may be replaceable by a weaker base as long as the acid sites are strong enough to activate one of the reactants.[34] This mechanism does not provide a satisfactory explanation for the present results because the MgO catalyst, which contains stronger acid sites, forms little of the condensation products. The exact mechanism of aldol product formation in the present studies has not yet been fully elucidated and will require further work.

4.3.6 Comparison of NR-Al to a Commercially Available Dye

As a final demonstration of the utility of the NR-Al dye in fluorescence studies of aldol reactions, its performance was compared to that of commercially available 3-perylene-carboxaldehyde. These studies are described in **Appendix B**. In contrast to NR-Al, the commercial dye showed little or no change in its fluorescence emission spectrum as aldol products were formed, see **Figure B.4**. It should be noted that coumarin dyes incorporating either aldehyde or ketone moieties also show unique spectral shifts in response to aldol product formation.[60, 127] However, these dyes are not well suited to single molecule studies, and the reactions reported were also performed at higher temperatures. In contrast, the aldol reactions presented here employed the NR chromophore widely used in single molecule studies,[64-66] and were run at room temperature, a condition more amenable to optical microscopic experiments.

4.4 Conclusions

In summary, we have synthesized a new form of the Nile Red dye, NR-Al, incorporating a reactive aldehyde moiety to probe aldol reactions in real time through ensemble fluorescence measurements. Fluorescence from the dye exhibits an appreciable blue shift when aldol addition and condensation products are formed. Catalysts that lead to formation of the addition product yield time-variant NR-Al fluorescence spectra incorporating an isoemissive point, consistent with formation of a single product. When the condensation product is also formed, the fluorescence spectra instead exhibit a gradual shift to the blue, due to the presence of addition and condensation products, along with residual starting material. These observations allow for preliminary conclusions on catalyst activity to be drawn.

The NR-Al fluorescence results in model reactions showed that product formation was dependent upon the type of catalyst employed. These observations were confirmed by HPLC and HPLC-MS characterization of the reaction mixtures. Reactions catalyzed by MgO yielded predominantly aldol addition products, while those catalyzed by Mg-Zr-Cs/SiO_2 produced both addition (alcohol) and condensation (olefin) products. The Mg-Zr-Cs/SiO_2 was shown to be more catalytically active towards olefin formation than MgO according to both fluorescence studies of the reaction kinetics and HPLC data. Detailed analysis of the base and acid site densities and strengths demonstrated that the MgO catalyst contained the strong base sites necessary to catalyze the addition reaction, but that the acid sites also present were likely too strong to give the condensation product. In contrast, the Mg-Zr-Cs/SiO_2 catalyst was found to incorporate both the basic sites needed to initiate the addition reaction and weak acid sites of appropriate strength to drive dehydration and irreversible formation of the olefin. Fumed silica was employed as a control and showed no activity due to the absence of active basic and acidic sites. The newly synthesized

NR-Al was shown to be much more useful in following crossed aldol reactions than a commercially available 3-perylene carboxaldehyde, which showed little change in its fluorescence spectra during these reactions. The results presented here show that the NR-Al dye is an effective fluorescent probe for *in situ* studies of aldol reactions of heterogeneous catalysts at both the ensemble and single molecule levels.

Chapter 5 - Towards Single Molecule Studies of Aldol Reactions

unpublished

Distribution of Work

I synthesized the dye employed in these experiments, prepared all the catalyst films, carried out aldol reactions and did much of the characterization. Abdulhafiz Usman developed the Mg-Zr-Cs/TMOS sol-gel recipe employed for the fabrication of the catalyst films. Shelby Weatherbee acquired and analyzed XPS data.

5.1 Introduction

The performance of a catalyst is determined by its chemical composition, atomic-scale structure and accessibility of catalytic sites.[168] Various characterization techniques for elemental composition and structure of catalysts have been employed to better understand their catalytic activity. Nanometer scale structural information has been routinely acquired from electron microscopy,[169] scanning probe microscopy[170, 171] and X-ray microscopy,[172] among others. In contrast, chemical composition of the catalyst is mostly limited to bulk analyses via solid-state NMR,[55] temperature-programmed desorption,[107, 173] and at best, with sub-millimeter spatial resolution using infra-red spectroscopy of numerous probe molecules[57] or X-ray Photoelectron Spectroscopy (XPS).[174, 175] The limited resolution of current techniques for assessing chemical composition within catalysts hinders research towards correlating catalytic activity to the catalyst properties (i.e. chemical, structural), which are certain to vary at the nanoscale. Gathering this information is crucial in designing better catalysts employed in industrial reactions.

Fluorescence microscopy has emerged as an important analytical tool to allow the identification of chemical species at the sub-micron and nanometer (single molecule level) scale

in a non-invasive way.[176] The spatio-temporal resolution of fluorescence microscopy techniques allow researchers to determine the concentration and distribution of chemical species in a three dimensional structure,[177, 178] and to follow molecular transport,[179, 180] catalyst-substrate interactions and even conversion of single molecules (i.e. on enzyme active sites).[179, 181] Recently, fluorescence microscopy has also been introduced to the field of catalysis, which has led to the uncovering of diffusion pathways, adsorption and desorption events, and chemical conversions at the micron and nanometer scales.[176, 182]

Roeffaers et al. first monitored real-time transformations of single organic molecules catalyzed by crystals of layered double hydroxide (LDH). By employing a wide field microscope, these researchers were able to map the spatial distribution of catalytic activity over the entire crystal by counting single turnovers (i.e. the appearance of individual fluorescent product molecules).[183] Chen et al. first monitored the microkinetics of resazurin at single gold nanoparticles. Resazurin is non-fluorescent even when it first binds into the nanoparticle, but after some time (sec) the nanoparticle catalyzes product formation. The fluorescent product (i.e. resorufin) gives off a burst of fluorescence that can be detected until the molecule desorbs and diffuses away. When a second resazurin molecule adsorbs and is converted on the nanoparticle, a second fluorescent burst occurs until the product diffuses away, and so on. Researchers monitored the time "on" (when a single resazurin molecule binds to a gold particle and is converted into resorufin) and time "off" (the time between two fluorescent bursts/product conversion). From the "off" times, the kinetics of the combined adsorption and surface reaction processes were obtained, whereas the "on" times provided information on the time needed for the product molecule to desorb from the surface.[184] Since Roeffaers pioneered fluorescence microscopy for catalysis research, researchers have become interested in related methods to resolve the Bronsted acidic

nature of solid catalysts employed in the petrochemical industry by employing various fluorogenic probes (i.e. furfuryl alcohol, styrene, thiophene).[52-54, 185]

Aldol reactions are also commonly employed in various industries as they provide synthetic routes for pharmaceuticals[13] and fine chemicals used in the production of industrial feedstocks, commodity chemicals, and biomass-derived renewable liquid fuels.[14-16] Aldol reactions between ketones and aldehydes lead to the formation of aldol addition (alcohol) and aldol condensation (olefin) products. Although these reactions are mostly base catalyzed, by employing strong homogenous catalysts (i.e. hydroxides), recent literature suggests that cooperativity of basic and acidic sites on heterogeneous catalysts aid in the formation of aldol products.[36, 38, 41, 42, 140, 152] The use of microscopic techniques to determine chemical composition within catalysts will further the understanding of the nanoscale chemical interactions between the reactant molecules and the catalytic sites on the catalyst. This knowledge will aid in designing sustainable heterogeneous catalysts for eco-friendly processes that may be translated to wide industrial scale reactions.

In this chapter, wide field fluorescence microscopy along with a fluorescent molecular probe, Nile Red Aldehyde (NR-Al), is employed for single molecule studies of aldol reactions. This chapter describes two-color single molecule spectroscopic (SMS) imaging studies of aldol products on thin catalyst films. The catalyst films (Mg-Zr-Cs/TMOS) were obtained via a sol gel method and incorporate cesium as the basic active site and magnesium and zirconium as surface stabilizers, while silica gel serves as the support and as a source for Bronsted acidic sites.[26, 38, 140] Spectroscopic ellipsometry (SE) and X-ray Photoelectron Spectroscopy (XPS) were used to verify that a thin film was deposited and that the active cesium component was present within the film. The emission ratio of single molecules of the un-reacted NR-Al is compared to that of single molecules of aldol products from previously run bulk reactions with acetone and acetophenone.

The results show that NR-Al and aldol products are likely to be resolved at the single molecule level. This chapter also describes *ex situ* aldol reactions of NR-Al and acetone catalyzed by (Mg-Zr-Cs/TMOS) films at room temperature, and work towards *in situ* aldol reactions with the same precursors and catalyst films.

5.2 Experimental Considerations

5.2.1 Chemical and Materials

Metal nitrates, $Mg(NO_3)_2 \cdot 6H_2O$, $ZrO(NO_3)_2 \cdot xH2O$ and $CsNO_3$, and Tetramethylorthosilicate (TMOS, 98%) were purchased from Sigma Aldrich. Microscope coverslips (Fisher Finest Premium, 25 mm x 25 mm) and cut, polished silicon wafers (University Wafer, boron doped, 15 mm x 15 mm) were used as substrates for the catalyst films. Aqueous metal nitrate solutions were prepared using high purity water (Fisher, HPLC grade) and high purity ethanol (Across, HPLC grade). Nile Red Aldehyde (NR-Al) was synthesized in house, see **Chapter 3**. Commercial Nile Red, NR, (Sigma Aldrich) was employed as control. Nanomolar concentration dye solutions were prepared from high purity ethanol. Aldol experiments employed ACS grade acetone (Fisher).

Mg-Zr-Cs/TMOS sol. The sol-gel method developed by Abdulhafiz Usman, Dept. of Chemical Engineering, was employed in the preparation of the catalyst films. The sol was comprised of TMOS, ethanol, water and 0.1 M HCl in molar ratios of 1:100:12.8:0.018 (TMOS:ethanol:water:0.1M HCl). In preparation of this sol, the components were first added to a clean glass vial in the following order: TMOS, ethanol, water. The mixture was then stirred for 30 sec, then aqueous nitrate solutions were added so that the theoretical content for Mg, Zr, and

Cs were 0.025 wt.%, 0.033 wt.% and 6 wt.% respectively. The sol was stirred for an additional 30 sec and 0.1 M HCl was added. The sol was subsequently stirred for 2 h and aged for another 24 h in a desiccator prior to use. Each catalyst film was formed by spin coating (Specialty Coating Systems, Inc., P-6000) a 150 μL volume of the sol onto the substrate (25 X 25 mm glass cover slips, or silicon) at 2500 rpm for 30 sec. The catalyst films were aged for an additional 24 h in a desiccator and calcined in flowing air at 500 °C for 3 h. When the furnace (Barnstead F1500) cooled to room temperature, the films were removed and used within 1 day. The catalyst-coated substrates were used right away or stored in a desiccator; the substrates were exposed to an air plasma for 2 min prior to use.

Isolated Aldol Products. Aldol products (i.e. aldol addition, and aldol condensation) from ensemble aldol reactions with NR-Al and either acetone or acetophenone catalyzed by Mg-Zr-Cs/SiO_2, see **Chapter 4.2.3,** were isolated and verified by analytical HPLC and HPLC-MS, see **Chapter 4.3.3**. The emission spectrum of each of the isolated aldol products was acquired in ensemble fluorescence. Some spectral information was also acquired at the ensemble level employing two-color SMS imaging.

***Ex situ* Aldol Reaction.** Two-color SMS imaging was employed to acquire the spectral emission of *ex situ* aldol reactions from each channel (572-646 nm, and 646-700 nm). Catalyst films were doped with nanomolar concentrations of NR-Al, 0.1 nM from ethanolic solution. The dye was spin coated as a 150 μL volume onto the substrate at 2500 rpm for 30 sec. Dye-doped catalyst films were dried in a vacuum desiccator overnight. *Ex situ* aldol reactions were carried out in a Plexiglas box (~19 X ~19 X ~10 cm^3) under a nitrogen atmosphere (10 mL/min). The nitrogen atmosphere prevented oxidation of the dye molecules as well as condensation of a water layer on the catalyst film; the presence of water reduces the catalytic activity.[44] Dye-doped catalyst films

were positioned near a reservoir containing acetone (22 mL) and exposed to acetone vapor for 1h. Nile Red served as a control, and it was doped at 50 pM from ethanolic solution; the same procedure above was followed. The substrates were subsequently dried in a vacuum desiccator overnight to remove weakly bound acetone. The films were then imaged with the inverted widefield fluorescence microscope, described in **Chapter 2.3.2**.

***In situ* Aldol Reaction.** Two-color SMS imaging was employed to acquire the spectral emission of *in situ* aldol reactions from each channel. Catalyst films were doped with nanomolar concentrations of NR-Al, 0.1 nM from ethanolic solution. The dye was spin coated as a 150 μL volume onto the substrate at 2500 rpm for 30 sec. Dye-doped catalyst films were dried in a vacuum desiccator overnight. *In situ* aldol reactions were carried out in a Plexiglas box (~13 X ~14 X 5 cm^3) under a nitrogen atmosphere (10 mL/min). Dye-doped catalyst films were positioned near a reservoir containing acetone (22 mL) and exposed to acetone vapor for 1h. Real-time aldol reaction events were monitored with an inverted wide-field fluorescence microscope. Control experiments with Nile Red, 5 nM, were done in a similar manner. Here, the higher NR concentration was required in order to have approximately the same spot density as in the NR-Al doped catalyst films during exposure to acetone vapor.

5.2.2 Methods

Film Thickness. The thickness of Mg-Zr-Cs/TMOS films was obtained by spectroscopic ellipsometry (α-SE, J.A. Woollam). Thickness measurements were obtained from films deposited on silicon substrates. The thickness of the SiO_2 layer on silicon was determined first prior to catalyst deposition. The sol containing the catalyst was subsequently spin coated onto the substrate, and the substrate was aged, calcined, and the thickness was remeasured. Thickness measurements

were taken at 2 mm intervals along and across the film, with measurements made at the same locations (to within ± 1 mm) before and after film deposition. The catalyst film thickness was taken as the difference between these two measurements. All measurements were made under a dry nitrogen environment. The catalyst film and silicon were modeled as a single transparent layer on silicon having refractive index n = 1.457 (at 633 nm). The Cauchy Equation was used to model optical dispersion; a smooth film was assumed (i.e. roughness parameter was turned off). The goodness of fit was characterized by the mean-square error (MSE) and all fits employed had MSE < 3.

Film Composition. The Mg, Zr, and Cs content of the catalyst films was accessed by X-ray photoelectron spectroscopy (XPS). XPS data were acquired using a PHI VersaProbe III scanning XPS microprobe. This instrument uses an Al Kα source (1486.6 eV). XPS spectra were acquired at ~5 mm spacings on each film, using a 200 μm spot size, 55 eV pass energy, and 0.100 eV step size. The binding energies were corrected for charge shifts using the C (1s) peak of adventitious carbon at 284.8 eV as a reference.[41]

Ensemble Fluorescence Spectra. Fluorescence spectra were acquired on a FluoroMax-2 spectrophotometer (Jobin Yvon Spex) using a Xenon lamp as the light source. Dye solutions were imaged in a quartz fluorimeter cell (Starna Cells) with a 10 mm pathlength. Excitation and emission spectra were acquired from 1 μM NR, 1 μM NR-Al, and ~ 1 μM aldol product solutions in DMSO. The emission spectra of all species were recorded from 578 to 800 nm, while exciting at 575 nm.

Two-color single molecule spectroscopic (SMS) Imaging. Differences in the fluorescence emission of NR, NR-Al, and aldol products, as well as real time monitoring of aldol reactions on catalyst films were assessed by two-color SMS imaging. For this purpose, catalyst

films doped with nanomolar concentrations of the above species were positioned over the objective lens of an inverted wide-field fluorescence microscope. This microscope has been described previously in detail.[186] The microscope set up and the primary components along the optical path are depicted in **Figure 2.4.** Dye-doped catalyst films were excited with a 532 nm laser. The source light was passed through a spinning optical diffuser, reflected from a dichroic mirror (Chroma 555 DCLP) and then focused into the back of a high numerical aperture (NA) oil immersion objective (Nikon APO-TIRF, 100X, 1.49 NA). The illuminated area in the samples was ~14 μm in diameter. The incident power was maintained at 0.6 ± 0.1 mW in all experiments. Fluorescence from dye molecules was collected by the same objective and separated from the excitation light by passing through the same dichroic mirror and a 570 long pass interference filter. The fluorescence was then split into two spectral bands using an image splitter (Carin Research OptoSplit II). Separation of the spectral bands was accomplished by a second dichroic mirror (Chroma 646 DCLP) and appropriate bandpass filters so that spectral bands of 572-646 nm and 646-700 nm were observed. Fluorescence in these two bands was simultaneously detected by a thermoelectrically cooled CCD camera (Andor iXon DU-897). Fluorescence videos 100 frames in length were recorded with a frame time of 0.5 sec at various positions to within ~0.5 cm radius from the center of the substrate. Fluorescence videos were analyzed using software written in house in the LabView programming environment. The software automatically located each fluorescent spot in the two channels, and subsequently fit each to a 2D Gaussian function to determine its location and peak signal. Fluorescent spots produced by the same molecule were linked into trajectories similar to those reported in the literature.[187]

5.3 Results and Discussion

5.3.1 Catalyst Film Characterization

Film Thickness. Spectroscopic ellipsometry measurements confirmed that a thin film of ~30 nm was deposited atop the silicon substrate. Three replicate measurements were performed at each position along and across the substrate, separated by 2 mm intervals to give a film thickness of 30.60 ± 0.13 nm at 95% Confidence Interval for n = 9. The reproducibility of film deposition was verified for two more catalyst films, which yielded thickness measurements of 30.34 ± 0.29 nm, and 30.80 ± 0.45 nm at 95% Confidence Interval for n = 9.

Film Composition. XPS data were acquired by Shelby Weatherbee, Dept. of Chemistry, Virginia Commonwealth University. Data were acquired at five different locations around the catalyst film ~5 mm from the edge and corners and at the center of the substrate (~1.5 X 1.5 cm^2). **Figure 5.1** depicts XPS spectra showing the Cs (3d) peaks for the Mg-Zr-Cs/TMOS catalyst film. The low Mg and Zr loadings (theoretically 0.025 wt.%, and 0.033 wt.% respectively) are below the instrument's detection limit (~ 0.1 %) and therefore not detected. The Si (2p) peak is also observed for the TMOS film, and the O (1s) peak for the catalyst and TMOS films. The binding energy for the active component in the catalyst films were 724.6 eV for suboxides of Cs (Cs_2O_2) in Mg-Zr-Cs/TMOS. The atomic concentration, wt. %, of Cs was determined from the weighted average of the measured peak areas for C (1s), Si (2p), O (1s) and Cs (3d) at five different positions around the catalyst film. Measured peak areas were scaled using the relative sensitive factor (RSF) of the instrument (85.570 for C, 115.11 for Si, 203.24 for O and 3783.4 for Cs). The Cs content of two catalyst films was 2.1 ± 0.5 wt. % and 2.4 ± 0.8 wt. % respectively, **Table 2**. A TMOS film control showed no peaks for Mg, Zr, or Cs.

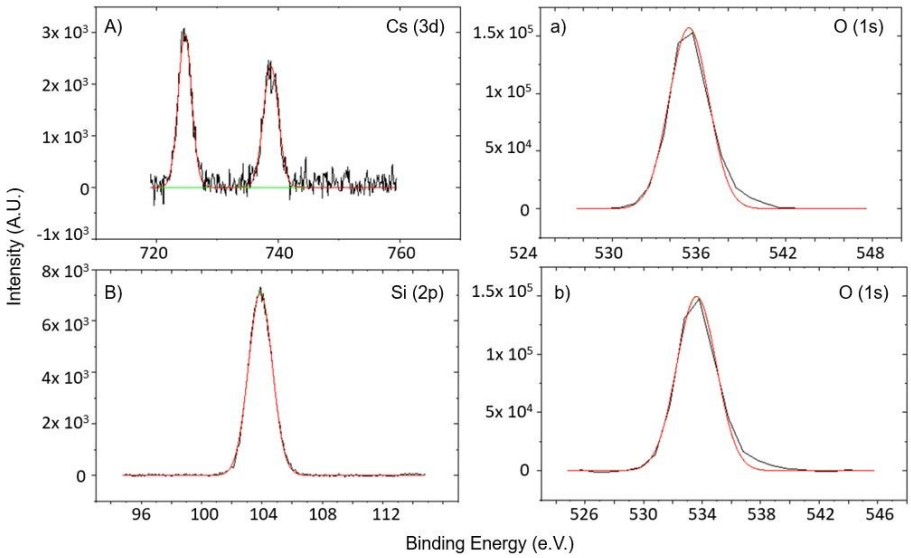

Figure 5.1 The XPS spectra of Mg-Zr-Cs/SiO_2 catalyst: The Cs (3d) peak (A), the 724.6 and 738.8 eV correspond to Cs $3d_{5/2}$ and Cs $3d_{3/2}$ from the Cs^+ ion.[154] The binding energy at 724.6 eV, can be attributed to Cs_2O_2,[155] The O (1s) peak (a), the binding energy at 533.2 eV is due to Si-O (Si-O-Si, Si-O-H) from SiO_2 support.[158] The XPS spectra of SiO_2: The Si (2p) peak (B), the 103.8 eV is due to Si-O_2.[159] The O (1s) peak (b), the binding energy at 533.2 eV is due to Si-O (Si-O-Si, Si-O-H) from SiO_2 support.[158] Data acquired by Shelby Weatherbee, Dept. of Chemistry, Virginia Commonwealth University.

Table 2 Atomic concentration, wt. %, of catalyst films

	C	O	Si	Cs
Catalyst Film 1	3.3 ± 1.9	55.3 ± 1.2	39.2 ± 1.2	2.1 ± 0.5
Catalyst Film 2	1.9 ± 0.9	55.9 ± 1.5	39.8 ± 0.4	2.4 ± 0.8

5.3.2 Optical Imaging

Ensemble Fluorescence Spectra of NR, NR-Al, and Aldol Products. Static fluorescence excitation and emission spectra of NR and NR-Al (1μM) in DMSO were shown in **Figure 3.3B**. The data showed that NR-Al is most efficiently excited near 580 nm and that its emission spectrum is shifted ~18 nm to the red compared to NR. **Figure 5.2** shows static fluorescence emission spectra

of isolated products from aldol reactions catalyzed by Mg-Zr-Cs/SiO_2 at room temperature. The products were isolated and verified by analytical HPLC and HPLC-MS, see **Chapter 4.3.3**. The data show static fluorescence emission spectra of the aldol addition (alcohol) and aldol condensation (olefin) products from the reaction with NR-Al and acetone, **Figure 5.2A**. The data also show emission spectra of the same products from the reaction with NR-Al and acetophenone, **Figure 5.2B**. It is evident that the alcohol product of both reactions is shifted to the blue compared to NR-Al, by ~13 nm. While the fluorescence emission of the olefin products is only slightly shifted to the blue, by ~2-4 nm.

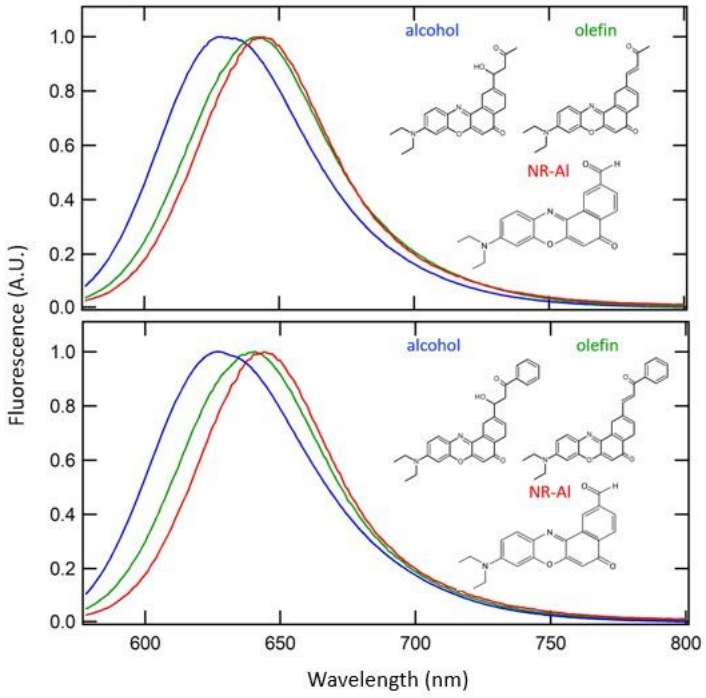

Figure 5.2 A) Normalized fluorescence emission spectra of 1 µM NR-Al (red), products from NR-Al-acetone aldol reaction: alcohol (blue), and olefin (green) in DMSO. **B)** Normalized fluorescence emission spectra of 1 µM NR-Al (red), products from NR-Al-acetophenone aldol reaction: alcohol (blue), and olefin (green) in DMSO. The emission spectra of the alcohol and olefin products in both aldol reactions are shifted ~13 nm and ~2-4 nm respectively to shorter wavelengths compared to NR-Al**.**

Single Molecule Fluorescence Imaging of NR, NR-Al, and Aldol Products. The dearth of single molecule studies of aldol reactions likely stems from the lack of suitable dyes designed to undergo aldol reactions while also remaining sufficiently fluorescent for detection at the single molecule level. To determine if NR-Al and the products of aldol reactions are fluorescent enough to be resolved at the single molecule level, catalyst films doped with nanomolar concentrations of these dyes were imaged employing an inverted wide-field microscope set up and the fluorescence emission from two spectral channels, 572-646 nm (right) and 646-700 nm (left) was analyzed.

Figure 5.3 shows representative two-color fluorescence images of the dyes adsorbed on catalyst films; NR was employed as a control. Surface-adsorbed dye molecules appeared as bright, immobile fluorescent spots that remained at the same location over several video frames. The individual fluorescent spots are attributed to adsorption of the dye molecules; control experiments performed in the absence of dyes yielded weakly fluorescent spots (< 5, per imaged area) which typically photobleached in less than 7 video frames. Nile Red shows more weakly fluorescent spots in the left channel compared to NR-Al, which correlates with the ensemble fluorescence data where the NR-Al emission is shifted to longer wavelengths. The images also show that both the aldol addition and aldol condensation products from aldol reactions with NR-Al and acetone or acetophenone are sufficiently fluorescent to be detected at the single molecule level.

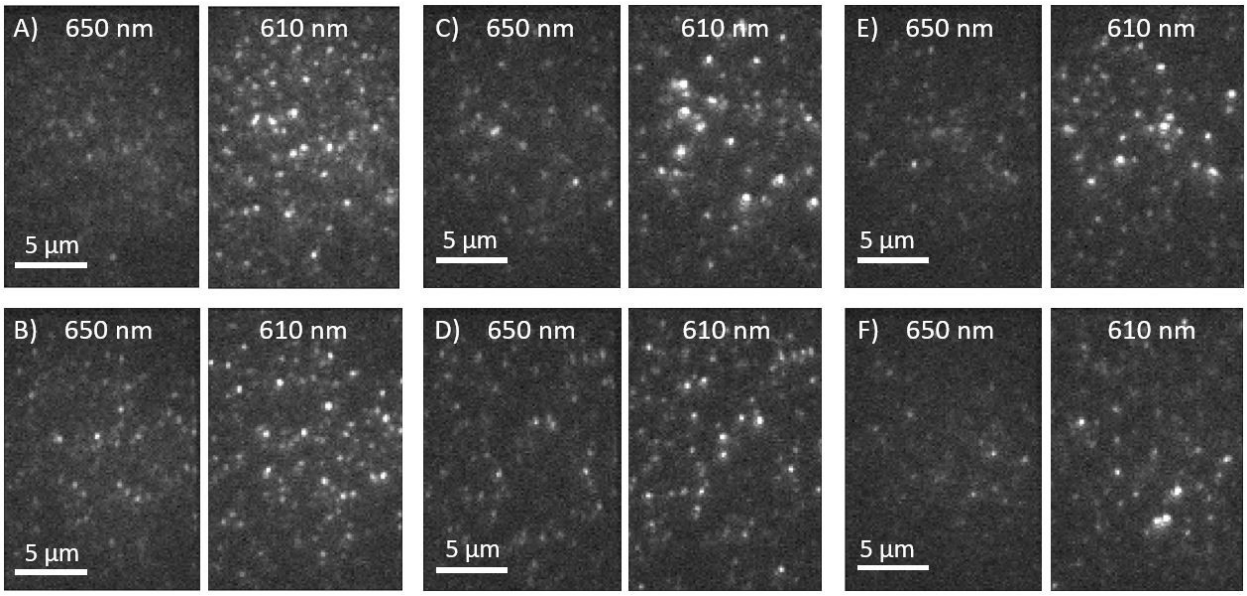

Figure 5.3 Two-color fluorescence images of dye-doped catalyst films **A)** NR, **B)** NR-Al, **C)** NR-Al-acetone alcohol product, and **D)** olefin product, **E)** NR-Al-acetophenone alcohol product, and **F)** olefin product. The color scale for all images is the same and depicts photon counts up to 500 counts/pixel.

The images depicted in **Figure 5.3** show that most of the aldol product molecules emit more strongly in the blue channel (610 nm). It also appears that a slightly higher number of aldol molecules from the NR-Al-acetone reaction appear to emit in the red channel (650 nm) compared to aldol molecules from the NR-Al-acetophenone reaction. A quantitative analysis of the fluorescence emission of the dye molecules above was performed to determine if spectral shifts can be quantified with certainty. For these analyses, the emission ratio from the two spectral channels was determined from **Equation 5.1**; where I represents the spot fluorescence amplitude in each channel.

$$E = \frac{I_{610} - I_{650}}{I_{610} + I_{650}} \qquad \textbf{Equation 5.1}$$

For the above quantitative analyses, only spot trajectories greater than 7 video frames in length were accounted for to eliminate short-lived weakly fluorescent impurity spots. Experiments were run in duplicates and a t-Test was employed to determine if the mean values measured for the different dye molecules were statistically different at 95% confidence interval (C.I.) for n = 4, t_c = 4.3, in each case. **Figure 5.4** shows the Gaussian distributions of E as well as the numerical average (Navg) of E values for the various dyes. The E value of NR-Al indicates that NR-Al is shifted to the red (longer wavelength) compared to NR, E = 0.545 ± 0.013 vs 0.654 ± 0.001, respectively (t > 4.3). In contrast, only the E value of the aldol addition product from reactions with NR-Al and acetone is shifted to the blue (shorter wavelength) compared to NR-Al, E = 0.597 ± 0.004 vs 0.545 ± 0.013, (t > 4.3). This correlates with the ensemble fluorescence spectral blue shift of ~13 nm, see **Figure 5.2**. The apparent shift in the measured spectra of other aldol products was not statistically significant (t < 4.3).

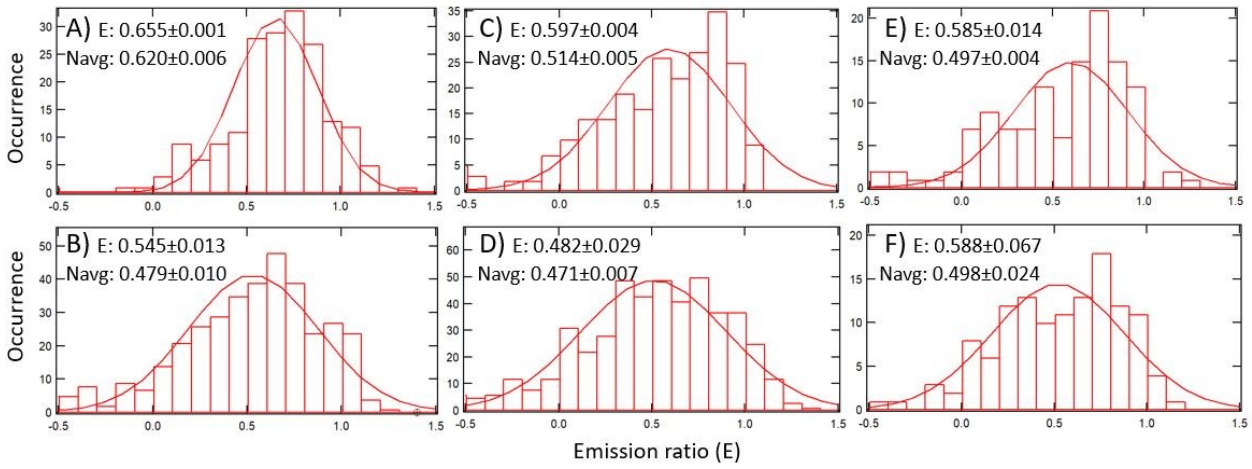

Figure 5.4 Distribution of single molecule emission ratios (E) from **Figure 5.3**. **A)** NR, **B)** NR-Al, **C)** NR-Al-acetone alcohol product, and **D)** olefin product, **E)** NR-Al-acetophenone alcohol product, and **F)** olefin product. The numerical average (Navg) is also listed as broad distributions shift the E value. The solid lines show fits of the data to Gaussian functions.

***Ex situ* Aldol reaction.** In order to determine whether Mg-Zr-Cs/TMOS films catalyze aldol reactions, *ex situ* experiments were performed with acetone vapor. Acetophenone was not employed for these experiments due to its much lower vapor pressure compared to acetone, 0.372 mm Hg vs 229 mm Hg. The higher vapor pressure allowed for saturation of acetone vapor on NR-Al-doped catalyst films within a reasonable time and facilitated *in situ* aldol reaction experiments. Nile Red was employed as a control. Catalyst films were doped with nanomolar concentrations of NR-Al and NR, 0.1 nM and 50 pM, respectively, and were exposed to acetone vapor for 1h in an otherwise dry nitrogen atmosphere (10 mL/min). In a second control experiment, dye-doped catalyst films were only exposed to a dry nitrogen atmosphere (10 mL/min) for 1h.

Two-color SMS imaging was again employed to measure the E value of the dye molecules before and after exposure to acetone vapor. Experiments were also run in duplicates and a t-Test was employed to determine if the mean values measured for *ex situ* aldol reactions were statistically different at 95% confidence interval (C.I.) for $n = 4$, $t_c = 4.3$, in each case. **Figure 5.5** shows Gaussian distributions of E values and of Navg of the above experiments employing **Equation 5.1**.NR and NR-Al controls without exposure and exposed to a dry nitrogen atmosphere, as well as NR controls exposed to acetone vapor showed no spectral shifts ($t < 4.3$ in each case). While the E value of NR-Al doped-catalyst films exposed to acetone vapor was not statistically different, the Navg value showed a blue shift. ($Navg = 0.476 \pm 0.023$, $t > 4.3$). The shift of Navg to shorter wavelengths in the aldol reaction between NR-Al and acetone is indicative of aldol product formation, based on the previous results described above.

Although the apparent red shift of E in the control reaction experiment with NR after exposure to acetone is not statistically significant ($t < 4.3$), spot counts decreased ~ 50% and may suggests the molecules may have migrated to a different micropolarity environment.[64, 66]

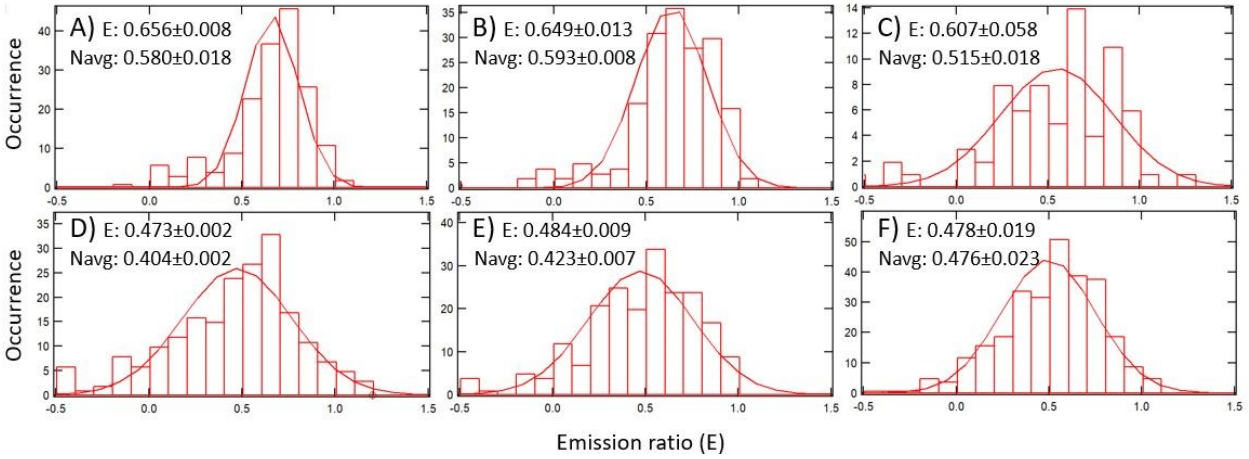

Figure 5.5 Distribution of single molecule emission ratios (E) from **NR: A)** control, **B)** in dry atmosphere (1h), **C)** exposed to acetone vapor (1h). Distribution of single molecule emission ratios (E) from **NR-Al: D)** control, **E)** in dry atmosphere (1h), **F)** exposed to acetone vapor (1h). The numerical average (Navg) is also listed as broad distributions shift the E value. The solid lines show fits of the data to Gaussian functions. NR-Al shifts to shorter wavelengths (F) when exposed to acetone vapor.

Efforts were made to confirm the products of *ex situ* aldol reactions via analytical HPLC based on the known elution times of the aldol products, see **Chapter 4.3.3**. For these sets of experiments, several catalyst films were doped with 0.25 mM NR-Al and exposed to acetone vapor for 1h or 8h. Dye molecules were re-dissolved in DMSO, concentrated, and eluted in analytical HPLC, see **Chapter 4.3.3** for column and elution parameters. However, samples were not concentrated enough to give robust results.

***In situ* Aldol Reactions.** Roeffaers and Chen showed the value of monitoring real-time transformations and chemical reactions on catalyst surfaces at the single molecule level. Nanoscale imaging of those studies revealed catalyst structure-dependent product formation and that the microkinetics of organic reactions on inorganic catalysts may be determined via formation of fluorescent products.[183, 184] This information is critical when designing and optimizing heterogeneous catalysts. In fact, similar SMS techniques have been employed to investigate the

nanoscale chemical and structural properties of solid catalysts already employed in the petrochemical industry.[52-54, 185]

This section describes work towards following *in situ* aldol reactions catalyzed by thin Mg-Zr-Cs/TMOS films in real-time. In these experiments, two-color SMS imaging was employed to monitor aldol reactions of 0.01 nM NR-Al-doped catalyst films exposed to acetone vapor in an otherwise dry nitrogen atmosphere (10 mL/min). Consecutive 100-frame videos (50 sec each) were taken at various positions within a ~0.5 cm radius from the center of the catalyst film (~1 cm diameter) during 1h exposure to acetone vapor. Here, NR (5 nM) was also employed as a control. The higher NR concentration was required in order to obtain approximately the same spot density as in the NR-Al-doped films when exposed to acetone vapor.

In order to detect spectral changes in dye molecule emission in real-time, and therefore aldol reaction events, the E value was plotted vs video frame along each single molecule trajectory, **Equation 5.1.** For these studies, spot trajectories > 11 video frames in length were analyzed. It was found that a minimum of 12 video frames was required to reveal clear temporal changes in E. Trajectories with an abrupt shift in E (> 0.25 units) and that lasted more than 5 video frames were interpreted as a possible reaction event. Fluctuations in E during imaging were small (~ 0.1 units) and are due to shot noise in the photon signal and in the background, see **Appendix C** for error analysis in E. Once a possible reaction event was identified, the fluorescent spot (molecule) and its pair was identified in the two channels based on its x-y coordinates and frame (time) of appearance and duration of the event. The fluorescent spot in each channel was manually followed on a frame by frame basis and the abrupt change in the fluorescent spot between the two channels was verified to come from the same molecule, and thus may be due to an aldol reaction event.

Based on the above criteria, 9 spot trajectories out of 313 trajectories (2.9%) that were > 11 video frames long showed a real change in E for *in situ* aldol reactions. Three reaction events were observed within the first 30 min, and six reaction events were observed within the next 30 min. It is noteworthy that reaction events displayed different behaviors: only one trajectory showed a red shift ($I_{610} < I_{650}$), six trajectories showed a blue shift ($I_{610} > I_{650}$), and two trajectories showed a red shift followed by a blue shift. **Figure 5.6** shows three different reaction events representatives of the behavior from nine spot trajectories found in *in situ* aldol reactions over NR-Al-doped catalyst films. **Figure 5.6 A** shows an abrupt red shift at frames 4 to 5 and stays constant for 6 frames until the molecule disappears, **Figure 5.6 B** shows an abrupt blue shift at frames 43 to 44 and stays constant for 7 frames until the molecule disappears, and **Figure 5.6 C** shows an abrupt red shift at frames 7 to 8 which stays constant for 23 frames and is followed by an abrupt blue shift at frames 31 to 32 that stays constant for 9 frames before the molecule disappears. **Figure 5.7** depicts two-color fluorescence images of the pairs of fluorescent spots from the plot shown in **Figure 5.6 C**. It is noteworthy that **Figures 5.6 A, B** show a blue or red shift that are one frame long. Although the shift only lasts one video frame, it is outside the noise level (~ 0.1 units). Therefore, it is likely that all three trajectories show the same behavior, red to blue shift; the possible cause will be discussed below.

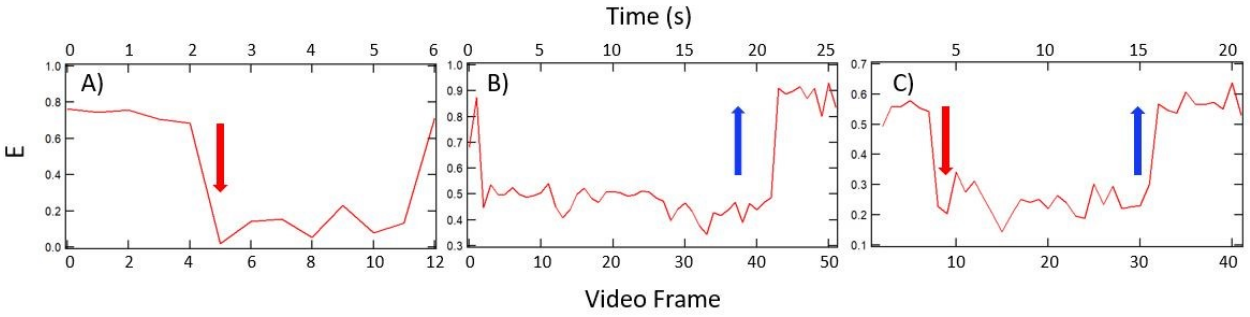

Figure 5.6 Plots of emission ratio (E) vs. video frame (Bottom) and Time (Top). **A)** A plot showing a red shift, **B)** A plot showing a blue shift, **C)** A plot showing a red shift followed by a blue shift.

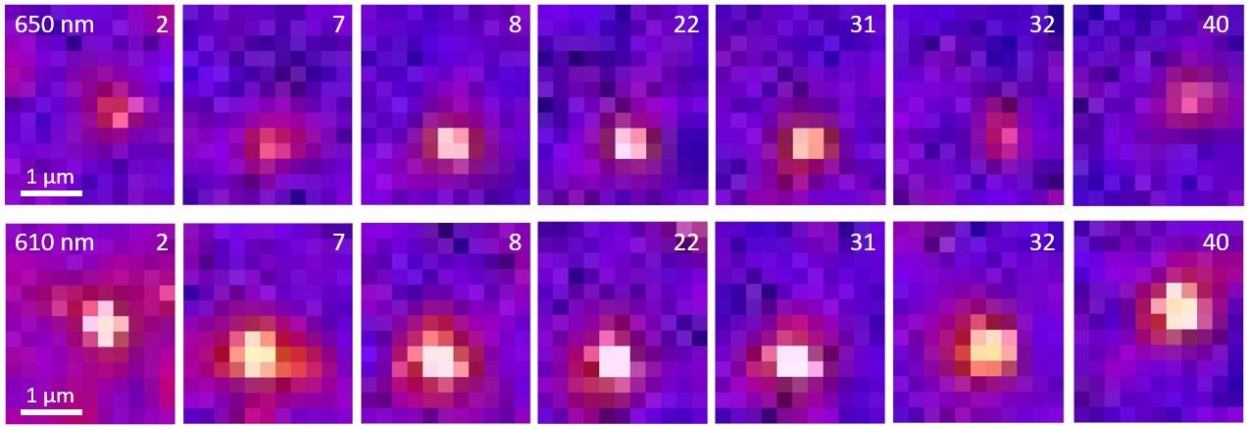

Figure 5.7 Consecutive video frames showing the fluorescence emission change in each channel (Top: 650 nm, Bottom: 610 nm) for the same NR-Al molecule during aldol reaction with acetone vapor in real time. The numbers in the upper right corner represent the video frame. The color scale for both images is the same and depicts photon counts up to 500 counts/pixel.

A compilation of ensemble fluorescence spectra, static SMS data, and *ex-situ* aldol reactions all suggest that the aldol addition product is blue shifted while the aldol condensation product has a similar fluorescence emission as NR-Al, which would make it difficult to distinguish from NR-Al without further analysis of the data (i.e. fluorescence lifetimes, or other analytical methods). Based on the above analyses of *in situ* aldol reactions, it is believed that the blue shift is due to an aldol reaction occurring in real-time, while the red shift may be due to a change in the micropolarity environment of NR-Al. Alternatively, the red shift may be due to the reversibility of the aldol reaction or conversion of the aldol addition product (alcohol) to the aldol condensation product (olefin); the possible mechanism of these aldol reactions was discussed in **Chapter 4.3.5**. However, if the latter was the case, trajectories would first show a blue shift and end at a red shift, as olefin formation is irreversible. Therefore, it is more likely that the red shift indicates a polar environment (provided by deposited acetone vapor) followed by an aldol reaction (blue shift). Alternatively, the red to blue shift may be a retro aldol reaction followed by an aldol reaction, where re-formation of NR-Al would shift the E value to the red. In order to determine the

reversibility of aldol reactions on catalyst films, SMS videos would need to be taken consecutively or intermittently at the same location. Decreasing the laser power, and frame exposure time would minimize/delay photobleaching of the product molecules and allow more information to be extracted.

The low population of spot trajectories with an abrupt E shift (i.e. aldol reaction) may indicate that a longer reaction time is necessary. This is possibly indicated by the increased number of spot trajectories apparently undergoing aldol reaction from 30 to 60 min compared to the first 30 min (6 vs. 3). A simple way to increase aldol reaction events is to increase the density of the catalyst active sites (i.e. cesium-oxide) within silica. For the above set of experiments, the catalyst loading was not optimized; systematic *in situ* aldol experiments with various catalyst loadings (confirmed by XPS) would allow for optimization of the catalyst film.

The few reaction events observed *in situ* may also indicate that aldol reactions may have already occurred prior to the time imaging was done at that particular location. XPS results showed that active species, Cs, are well dispersed around the silica film. Theoretically, the probability of aldol reaction events occurring at the same time at any given location is the same (provided that the catalyst film is homogenously coated with a thin film of acetone vapor). In the above experiments, acetone evaporation and deposition rates were not optimized. It is possible that acetone vapor saturated the catalyst film (i.e. active sites) thereby decreasing the rate of aldol reactions. Here too, systematic experiments would allow optimization of acetone vapor deposition. Perhaps acetone vapor needs to be deposited at a slower rate or intermittently.

In situ control experiments of NR-doped catalyst films exposed to acetone vapor under the same conditions as *in situ* aldol reactions only showed one spot trajectory out of 485, 0.21 %,

where the E value abruptly shifted to the blue during acetone exposure; the causes for this shift are unknown.

5.4 Conclusion

In summary, the present studies show that NR-Al and the products of aldol reactions (NR-Al with acetone or acetophenone) are fluorescent enough to be detected at the single molecule level. The development of a reactive NR-Al molecular probe allowed a breakthrough in aldol reaction studies *ex situ* and in real-time at the nanoscale. These early studies focused on aldol reactions of acetone vapor on NR-Al-doped Mg-Zr-Cs/TMOS catalyst films. Spectroscopic ellipsometry revealed a well-dispersed film of ~30 nm in thickness. XPS did not detect Mg or Zr since their theoretical loading was below the instrument's detection limit (~ 0.1 %), but Cs was well-dispersed within and around the films, 2.1 ± 0.5 wt. % and 2.4 ± 0.8 wt. % respectively.

Although the products of aldol reactions catalyzed by Mg-Zr-Cs/TMOS films were not confirmed in *ex situ* studies due to their low concentrations, experimental data showed that two-color SMS studies follow the same trend observed in ensemble fluorescence spectra of NR-Al and isolated aldol products. While the peak emission wavelength of the aldol condensation product is similar to NR-Al (~642 nm), that of the aldol addition product is shifted to shorter wavelengths (~13 nm in ensemble experiments, and E value shift ~0.04 in SMS experiments). Control SMS studies of NR and NR-Al not exposed to acetone vapor, and NR exposed to acetone vapor revealed similar E values (E = 0.634 ± 0.022 for NR, and E= 0.478 ± 0.006 for NR-Al). NR-Al doped catalyst films exposed to acetone vapor showed a red to blue shift instead of the expected blue shift from ensemble studies. This may simply reflect the complexities of interpreting the single molecule data and synchronizing aldol reactions with the recording of the video data.

The findings provide a platform for future SMS studies of aldol reactions on thin catalyst films and, in the future, structurally and chemically different heterogeneous catalysts. Such nanoscale studies will provide more insight into the specific cooperativity of various chemical environments as well as structure-dependent product formation and even on the microkinetics of aldol reactions, which are critical when designing and improving heterogeneous catalysts for economical and eco-friendly industrial processes.

Chapter 6 - Vapor Phase Plotting of Organosilane Chemical Gradients

Reprinted with permission from Judith Bautista-Gomez, Anna V. Forzano, Joshua M. Austin, Maryanne M. Collinson, and Daniel A. Higgins. Vapor-Phase Plotting of Organosilane Chemical Gradients. *Langmuir*, 2018, 34, 33, 9665-9672.

Contributions of Authors

I was in charge of sample preparation and optimizing the plotting conditions as well as data analysis. Dr. Forzano conducted all XPS experiments. Joshua Austin helped in the early stages of the project by taking water contact angles and organosilane-film thicknesses. Dr. Collinson helped interpret XPS data. Dr. Higgins guided the research and helped interpret XPS data. He and Dr. Collinson provided tremendous help for the preparation and publication of this work.

6.1 Introduction

Thin films designed to exhibit chemical and/or physical properties that gradually vary along one or more directions are known as chemical gradients.[67-70] These materials find myriad potential applications in diverse fields of research ranging from materials science to biology. They have been used previously in combinatorial materials chemistry,[73] high-throughput investigations of molecule-surface interactions,[76] catalysis,[72] chemical separations,[74, 75] molecular combing of DNA[77] and to drive the motions of liquid droplets,[82] vesicles,[188] nanoparticles,[189] macromolecules,[190] and cells.[191] Gradient fabrication has been accomplished by a variety of methods, including by vapor diffusion,[82, 192] solution diffusion,[76, 191, 193] microfluidic mixing,[194] ink jet printing,[84] photolithography,[85] contact printing,[83] electrochemical methods,[195] dip-coating,[86-88]

and controlled-rate infusion methods.[89, 90] Deposition methods that rely upon precursor diffusion alone do not afford any control over the gradient profile or steepness, which is determined by Fick's Laws. Furthermore, few such methods allow for patterning of the film. Unless masking procedures are employed to achieve gradient deposition over small regions, the gradients obtained usually cover the entire substrate surface. While photolithography[85] and contact printing[83] afford control over the gradient profile and can be used to make patterned films, changing the gradient characteristics or film pattern requires the fabrication of a new mask or stamp. Although both dip-coating[86-88] and controlled-rate infusion[89, 90] methods allow the gradient profile to be manipulated, neither allows for the deposition of patterned films. Ink jet printing[84] is a direct-write method that provides the flexibility required to produce gradients of arbitrary shape, location, and profile, but it requires careful optimization of the ink properties (e.g., surface tension, viscosity and solvent volatility) to achieve proper jetting.[91, 92] Furthermore, the printing of reactive materials by ink jet methods frequently leads to clogging of the print nozzles. Since ink jet printing relies on the deposition of liquid droplets on solid surfaces, de-wetting of the substrate and de-mixing of the ink solutions can also be problematic.

As an alternative to the aforementioned methods, this report describes the vapor phase plotting of organochlorosilanes for making patterned and chemically graded self-assembled monolayer (SAM gradient) films. To the best of our knowledge, this represents the first report of vapor phase plotting of organosilane materials. Although similar vapor jet printing methods have been employed for the deposition of organic semiconductors,[196-198] these methods have not yet been used to fabricate gradients. Vapor jet printing works by passing a heated gas through a hot organic powder or liquid source, often under reduced pressure. The gas carries the molecular

species through a nozzle and deposits them onto a cooled substrate. The printing of patterned films with ~ 4 μm spatial resolution has been reported under certain conditions.[199]

This chapter describes how organosilane vapor is delivered to a reactive silica surface using a glass capillary positioned just above the surface. The capillary is connected via a short flexible tube to a reservoir containing the precursor liquid. A carrier gas sweeps precursor vapor from the headspace above the reservoir into the tubing and delivers it to the capillary, which provides for localized exposure of the substrate. Unlike vapor jet printing, organosilane vapor phase plotting is performed at room temperature and atmospheric pressure. By raster scanning the capillary above the silica surface, patterned uniform or gradient films that cover a small region of the substrate can be produced. The amount of material deposited can be changed by varying either the raster-scanning speed or the carrier gas flow rate. The ultimate spatial resolution of vapor phase plotting is governed by diffusion and convective dispersion of the gas-phase precursors after they exit the capillary. The size of the smallest features that can be produced is limited by the capillary diameter and its distance above the substrate surface. In this initial demonstration, we have achieved millimeter scale spatial resolution using glass capillaries with millimeter inner diameters. With further development of the method, up to a 100-fold improvement in plotting resolution should be achievable. Vapor phase plotting is a direct-write method that allows for patterned uniform or gradient films to be prepared over selected substrate regions, without modifying neighboring areas. It is likely to find applications in the fabrication of SAMS for use in planar chromatography, microfluidic devices, electronics, optical devices, and to study organic reactions on thin catalyst films.

6.2 Experimental Considerations

6.2.1 Materials

SAM films and gradients were prepared from *n*-octyltrichlorosilane (97%) and 3-cyanopropyltrichlorosilane (97%) precursors. The organotrichlorosilanes were obtained from Sigma-Aldrich and were used as received. Each was dissolved in a solvent prior to being transferred to the reservoir. The solvents tested include toluene, *n*-heptane, and *n*-butanol.

Both microscope coverslips (Fisher Finest Premium, 25 mm x 25 mm) and cut, polished silicon wafers (University Wafer, boron doped, 10 mm x 20 mm) were used as substrates upon which the SAM films and gradients were deposited. Each substrate was cleaned prior to use by exposure to an air plasma for 5 min. As has been demonstrated previously, organosilane films are best formed on substrates already coated with a silica base layer.[90] The base layer provides a uniformly reactive surface with sufficient silanol sites to allow for efficient attachment of the organotrichlorosilanes.[118] Base layers were deposited from a sol comprised of tetramethoxysilane (TMOS), ethanol (200 proof), and 0.1 M HCl in volume fractions of 0.94:94.0:5.06 (TMOS:ethanol:0.1M HCl). In preparation of this sol, the components were first added to a clean glass vial. The sol was then stirred for 1 h and aged for another 23 h in a desiccator prior to use. Each base layer was formed by spin coating (Specialty Coating Systems, Inc., P-6000) a 150 μL volume of the sol onto the substrate at 5000 rpm for 30 s. Base layers prepared in this manner had thicknesses of 16 ± 5 nm on average, as determined by spectroscopic ellipsometry. The base-layer-coated substrates were stored in a desiccator for at least 24 h prior to use and were subsequently exposed to an air plasma for 2 min prior to vapor plotting.

6.2.2 Methods

Film deposition and gradient formation were verified by sessile drop water contact angle (WCA) measurements, spectroscopic ellipsometry, and X-ray photoelectron spectroscopy (XPS) mapping. The same methods also allowed for the gradient profile to be recorded. For WCA measurements, 0.1-0.5 μL droplets of pure water (18 MΩ·cm, B-pure, Barnstead) were placed on the SAM films at several locations, using a microliter syringe (Hamilton). A home-built instrument equipped with a CCD camera (ProVIDEO, CVC-140) and zoom lens (Navitar) was used to photograph the individual water droplets. A plugin for the freely available ImageJ software[119] was used to determine the contact angle from each photograph.

Silica base layer and SAM film thicknesses were measured using an α-SE spectroscopic ellipsometer (J.A. Woollam Co., Inc.). All film thickness data were acquired from samples deposited on silicon wafers. The use of silicon substrates ensured a strong optical reflection from the film-substrate interface, affording the measurement precision needed to determine the thickness of sub-monolayer films. To avoid errors in the measured thickness caused by condensed water layers, all ellipsometric measurements were made under a dry nitrogen atmosphere inside a Plexiglas chamber. The chamber was purged with nitrogen for at least 30 min prior to each set of measurements, and the purge was maintained throughout each experiment. In fitting the ellipsometry data, each film was modeled as a transparent film on silicon, having refractive index n = 1.457 (at 633 nm). The optical dispersion of both the silica base layer and organosilane films were modeled by the Cauchy Equation. In all cases (both base layer and organosilane-coated base layer), the films were treated as a single layer on the substrate, because the refractive indexes of the films are all very similar.[120] To determine the organosilane layer thickness, the base-layer thickness was first measured prior to vapor plotting of the organotrichlorosilane. The base-layer

thickness was measured at a series of positions separated by 2 mm spacings along the substrate. The SAM film was then deposited atop the base layer and the film thickness was remeasured at each of the previous locations (to within ± 1 mm). The SAM film thickness was obtained as the difference between the full film thickness and the base layer thickness.

XPS mapping experiments were employed to verify the chemical composition of the SAM films and gradients. XPS data were acquired using a Thermo Fisher ESCAlab 250 imaging spectrometer. This instrument uses an Al Kα source (1468.68 eV). XPS spectra were acquired at 1-2 mm spacings on each film, using a 500 μm spot size, 50 eV pass energy, and 0.100 eV step size. Analysis of film properties was restricted to the N(1s) region of the spectrum for the cyanopropyltrichlorosilane-derived SAM films. The presence of adventitious carbon made XPS characterization in the C(1s) region difficult. However, the C(1s) data were also collected to allow for the N(1s) data to be corrected for charge shifts. In this case, the data were all shifted so that the C(1s) peak for adventitious carbon appeared at 284.6 eV. The area under the nitrile N(1s) peak was determined by subtracting the background, fitting each spectrum with two Gaussian functions,[200] and determining the area under the appropriate peak from its amplitude and width.

6.3 Results and Discussion

6.3.1 Vapor-Phase Plotting

SAM films and gradients were prepared using a simple, inexpensive vapor phase plotter that was designed and constructed in-house. The critical working components of the vapor plotter include a precursor reservoir, a glass capillary for delivery of the precursor vapor to the substrate surface, and an X,Y plotter. **Figure 6.1** shows a schematic diagram and a photograph of the

apparatus. Briefly, vapor plotting is accomplished by first loading the precursor reservoir with organosilane solution. An inert carrier gas is then used to sweep organosilane vapor from the reservoir into the capillary, which is connected to the reservoir via flexible tubing. The capillary is mounted to the X,Y-plotter, allowing for it to be raster scanned above the substrate surface. The working end of the capillary is positioned a few tens of micrometers above the substrate, allowing for local regions to be exposed to silane vapor in a controlled manner. The entire apparatus is housed within a sealed deposition chamber that allows for the ambient atmosphere to be controlled during plotting. The entire vapor phase plotting process is described in more detail, below.

As noted above, delivery of the precursor silanes to the substrate surface requires the use of a carrier gas. Dry nitrogen was employed in these studies. The carrier gas was first passed through the precursor reservoir and then into the flexible tubing connecting the reservoir and capillary. The carrier gas flow rate was maintained at 3.3 ± 0.1 mL/min in these experiments. The volume of the headspace in the precursor reservoir was ~ 5 mL. Two types of flexible tubing were tested in this initial demonstration. They include Silastic tubing (Dow Corning, 1.57 mm ID, 3.18 mm OD) and Teflon tubing (Optimize Technologies, Inc., 1.8 mm ID, 3.2 mm OD). The Teflon tubing was concluded to be best suited for this application because it is more compatible with the solvents and silanes employed.[201] Some evidence for accumulation of residual silanes within the tubing and between runs was observed when the Silastic tubing was used, particularly at high precursor concentrations. Because Teflon tubing is less elastic, a short segment (~ 1 cm) of the Silastic tubing was used to join the Teflon tubing to the glass capillary.

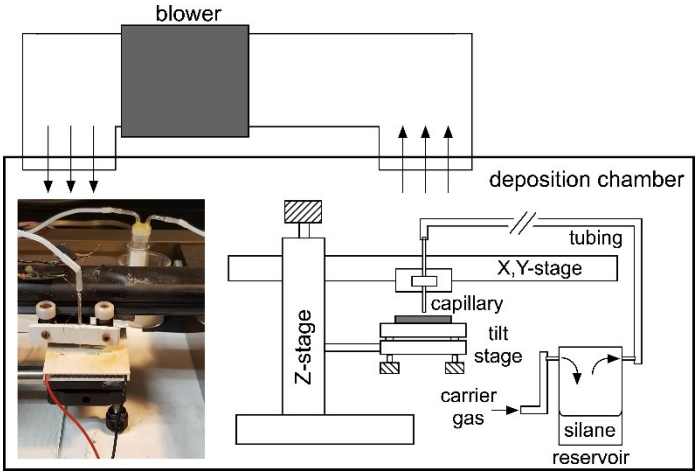

Figure 6.1 Deposition chamber for vapor phase plotting of SAM films and gradients. The inset shows a photograph of the capillary, substrate, reservoir and sample stage.

The capillaries selected for use were melting point capillaries (Kimble Chase, 1.5 mm ID, 1.8 mm OD, 4.5 cm L). Each capillary was wrapped in Nichrome wire (Omega, 0.16 mm diam., 56 Ohm/m) to allow for heating to ~ 35° C, as measured with an infrared thermometer. Heating of the capillary was required to prevent condensation of the precursor at its outlet when high precursor concentrations were employed. The glass capillary was mounted on the stepper motor driven X,Y plotter with its long axis oriented perpendicular to the substrate surface, as shown in **Figure 6.1**. The plotter stage employed was obtained from Wave Dynamics, and had a 320 mm x 240 mm total travel, with a maximum working speed of 450 and 300 mm/s in the two directions. The raster scanning speed employed during deposition ranged from 0.44 to 175 mm/min in the fast-scan direction. The substrate was positioned beneath the capillary by mounting it on a tilt stage (ThorLabs, KM100B) attached to a linear translation stage (Newport, 460A). This mounting procedure allowed for the substrate to be reproducibly positioned beneath the capillary with micrometer precision. The X,Y plotter was controlled by software written in-house in the Labview (National Instruments) programming environment. The entire apparatus was housed inside a transparent plastic box (the deposition chamber) to better control the ambient humidity. The

humidity within the box was raised when necessary either by bubbling air recirculated from within the box through a water-filled flask, or by use of a miniature ultrasonic humidifier. Strong convective air currents were required to achieve optimum spatial resolution during vapor plotting. These air currents served to rapidly remove and dilute residual unreacted precursor vapors from near the capillary/substrate junction. A blower attached to 10 cm diameter tubing was used for this purpose. The blower continuously recirculated the air back into the deposition chamber at a distance of ~ 0.35 m from the substrate. A mechanical damper was used to control the flowrate of air through the blower. A marked degradation in plotting resolution was observed if the blower was not turned on. The deposition chamber was vented into the fume hood system prior to removal of the sample, following each deposition.

6.3.2 Optimization of Plotting Conditions

The extent of surface modification was found to depend upon a number of different parameters, including the rate at which the liquid precursor evaporates into the vapor phase inside the precursor reservoir. The rate of precursor evaporation is dependent upon the boiling point of the precursor and its heat of vaporization, but it also depends on its rate of diffusion to the liquid-vapor interface (the precursor solutions were not stirred). According to the Stokes-Einstein relation, the rate of diffusion scales inversely with solution viscosity. Therefore, solvents of low viscosity were employed for diluting the precursor silane. To identify a suitable solvent, *n*-octyltrichlorosilane was alternately dissolved in toluene (η = 0.560 cP), *n*-dodecane (η = 1.383 cP) and *n*-butanol (η = 2.544 cP).[202] Square SAM "pads" 3 mm x 3 mm in size were then plotted under otherwise identical conditions. Films plotted from toluene solutions gave the highest WCAs (~ 71°) while those plotted from *n*-dodecane gave somewhat smaller values (~ 64°) and *n*-butanol

gave the lowest WCAs (~ 41º). On the basis of these results, toluene was selected for use as the diluting solvent in the remainder of the work presented below. The low WCAs obtained when *n*-butanol was employed could result from reaction of the chlorosilane with the alcohol, in addition to slow precursor diffusion in solution. The dependence on precursor evaporation rate could lead to variations in film properties with changes in the reservoir design and carrier gas flow rate. A fixed reservoir design and constant gas flow rate (see **Figure 6.1**) were employed to help avoid such difficulties.

As has been previously reported,[203] the deposition of organotrichlorosilanes from the vapor phase was found to be strongly dependent upon the relative humidity (RH) of the environment within the deposition chamber. It is believed that the moisture dependence of film growth results from the participation of surface-adsorbed water in cross-linking of the trichlorosilane precursors.[204, 205] In order to identify the optimum level of moisture required for efficient film deposition, 3 mm x 3 mm square *n*-octyltrichlorosilane pads were plotted at a series of different relative humidities, with all other factors held constant. **Figure 6.2A, B** shows the plot of the SAM film thicknesses and WCAs measured from these pads as a function of RH. These data show that the highest WCAs were obtained at humidities above ~ 30% RH. The film thickness data also provide clear evidence of humidity dependent variations in the SAM film surface coverage. The mean film thickness fell from ~ 1 nm at humidities above 50% RH to ~ 0.7 nm at a humidity of ~ 23% RH. A full monolayer of well-packed octylsilane molecules is expected to be ~ 1.1 nm thick.[203] On the basis of these results, all films described in the remainder of this report were prepared at humidities of ~ 45 ± 5% RH.

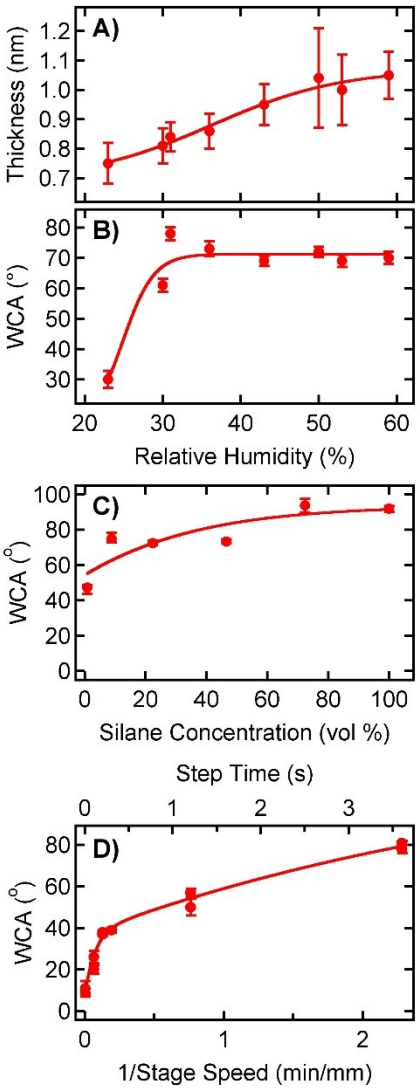

Figure 6.2 A) Film thickness for *n*-octyltrichlorosilane monolayers prepared under different relative humidities. **B)** WCAs measured for the same films. The concentration of silane in the deposition reservoir was 10 vol % in toluene solution. The capillary-substrate separation was 30 μm. The step time during raster scanning was fixed at 3.6 s. **C)** WCA measured as a function of *n*-octyltrichlorosilane concentration (vol %) in toluene. The SAM pads characterized were deposited at ~50% RH with a capillary-substrate separation of 30 μm and a stage speed ~ 0.44 mm/min. **D)** WCA as a function of stepper motor step time (top axis) and 1/stage speed (bottom axis). Both the step delay and stage speed correspond to motion along the fast raster-scanning axis. The solid lines have been added to better depict trends in the data. The fast rise in WCA at short step times is consistent with a fast-kinetic process for the initial reaction with the surface. The error bars depict the 95% confidence interval on each value for n = 12, 5, 5 and 5 in panels **A) - D)**, respectively.

The distance between the capillary and substrate was found to impact both the plotting resolution and the ultimate SAM surface coverage under otherwise identical conditions. Here, the capillary-substrate distance was adjusted using the linear stage upon which the sample was supported (see **Figure 6.1**) and was measured from magnified images of the junction obtained using a CCD camera. In these experiments, several square SAM pads (3 mm x 3 mm in size) were again plotted and the WCAs measured for each. **Figure 6.3** shows that the WCA was greatest (~ 71°) at a capillary-substrate separation of ~ 30 µm. The WCA decreased slightly (by ~ 5 – 10°) as the capillary was moved either closer to, or further away (out to ~ 90 µm) from the substrate. The decrease in WCA at shorter capillary-substrate separations is attributed to the increased velocity of the vapor exiting the capillary as it is brought closer to the surface. This effectively reduces the substrate exposure time and decreases the degree of modification. At greater distances, the effective concentration of precursor in the vapor phase is reduced by removal and dilution of the precursor by the convective air currents created by the blower, again leading to a reduction in surface coverage. On the basis of these results, a separation of 30 µm was selected for use in all experiments.

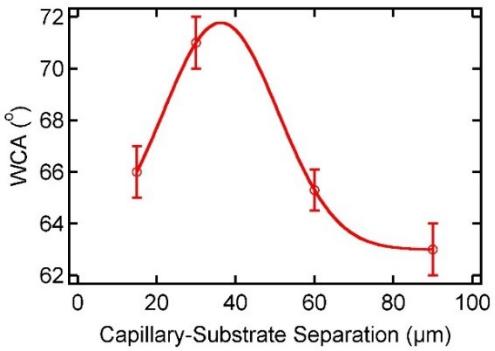

Figure 6.3 Water contact angle as a function of capillary-substrate separation. The solid line was added to better depict the trend in the data. The error bars depict the 95% confidence interval on each value for n = 3 measurements.

As noted above, the precursor silanes were diluted in a suitable solvent prior to deposition. Without dilution of the liquid precursor, its delivery to the capillary and substrate surface was frequently too rapid, leading to visible condensation of the precursor in the capillary and on the substrate surface. Therefore, the concentration of organotrichlorosilane in the toluene solution is also a critical parameter that must be optimized to obtain good films in a reasonable amount of time. **Figure 6.2C** plots the WCA values measured for a series of 3 mm x 3 mm square SAM pads printed using a range of *n*-octyltrichlorosilane concentrations. The concentration is given in volume percent, with toluene as the solvent. The WCA values were found to increase with increasing precursor concentration from ~ 1 vol % (WCA ~ 50°) to 100 vol % (WCA ~ 92°). Control experiments performed with pure toluene in the reservoir produced surfaces with WCAs of < 10°.

Finally, the reaction of the organotrichlorosilane with the substrate surface occurs at a finite rate,[118] and hence, the length of time the substrate is exposed to the vapor also plays an important role in determining the surface coverage and the WCA achieved. The influence of reaction kinetics on the surface coverage was explored by varying the rate at which the capillary was raster scanned across the surface during silane deposition. Square SAM pads 3 mm x 3 mm in size were again printed in these studies. The pads were printed as a square array on individual substrates to produce patterned surfaces. As stepper motors were used to move the plotting stage (see **Figure 6.1**), the rate of capillary motion was adjusted by simply changing the time between motor steps. The time between steps in the fast-scan direction was varied between 9 ms and 3.6 s. The WCAs obtained for SAM pads deposited from 10 vol % octyltrichlorosilane are plotted as a function of the step time in **Figure 6.2D** (top axis) and as a function of reciprocal stage speed in minutes per millimeter (bottom axis). Here, the stage speed corresponds to the rastering speed along the fast-scan

direction. Replicate measurements are included in **Figure 6.2D** to demonstrate the reproducibility of the WCA values obtained. These data reveal a biexponential rise in the WCA as the time between steps increased. This observation is consistent with an initial fast reaction of the silanes with the substrate surface, followed by a much (~ 50-fold) slower deposition occurring at longer times. Indeed, early studies of chlorosilane reaction kinetics on silica surfaces show similar behavior, with the kinetics exhibiting a ~ 1.5 order dependence on the density of reactive surface sites.[118] The complex deposition kinetics are also consistent with what has been observed for other silanes deposited in a time-dependent manner from solution.[89, 90]

It is noteworthy that the WCA values shown in **Figure 6.2** never reach the ~ 105° value reported previously for octylsilane monolayers deposited by vapor diffusion methods.[203] Rather, films that exceed a monolayer in thickness (> 1.1 nm) were found to yield WCAs of ~ 90° (see **Figure 6.2C**). The exact origins of the lower WCAs observed for films prepared by vapor-phase plotting are unknown at present but are believed to reflect molecular disorder in the films caused by the rapid delivery and removal (i.e., short residence times) of the silanes on the substrate. The kinetics of silane removal are likely similar to the surface reaction rate and this would result in the initial attachment of silanes at relatively low surface coverages. In this case, the hydrocarbon chains are likely to be oriented randomly, leading to films that are more disordered than ideal SAMs.[206]

The rate of precursor deposition was also investigated for the 3-cyanopropyltrichlorosilane precursor. For this purpose, square pads 3 mm x 3 mm in size were again plotted using a series of different raster scanning rates. **Figure 6.4** shows the WCAs obtained. In this case, they approached ~ 57°, as has been observed previously for vapor deposited cyanopropylsilane films.[203]

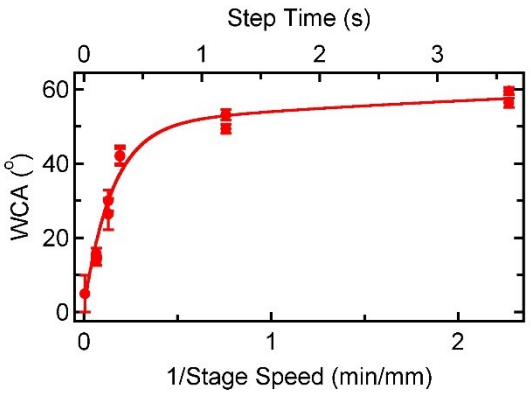

Figure 6.4 Water contact angle as a function of stepper motor step time (top axis) and 1/stage speed (bottom axis) for 3-cyanopropyltrichlorosilane monolayers. Both the step delay and stage speed correspond to motion along the fast raster scanning axis. The solid line was added to better depict the trend in the data. The fast rise in WCA at short step times is consistent with a fast-kinetic process for the initial reaction with the surface. The error bars depict the 95% confidence interval on each value for n = 5 measurements.

It should be noted that both the octylsilane and cyanopropylsilane films were characterized as deposited and were not rinsed prior to WCA, thickness, or XPS measurements. However, in each case, characterization of the films was delayed for at least 3 h after film preparation. Film stability was verified by several methods. In one set of experiments, the plotted films were sonicated in 18 MΩ·cm water for 3 min, at a temperature of 65 °C. They were subsequently rinsed with water and blown dry in a stream of nitrogen. In another case, the films were sonicated in isopropyl alcohol for 3 min, then in acetone for 3 min, then rinsed with acetone and blown dry with nitrogen. Finally, some films were soaked in room temperature water for a minimum of 16 h. In all cases, the plotted silane films yielded similar or slightly higher (increased by ~ 6°) WCAs after these treatments, while neighboring (unmodified) regions yielded WCAs of < 10°.

6.3.3 Plotting of Organosilane Gradients

Organosilane gradients were plotted using the conditions determined in the above experiments. The previous data were used to select the optimum humidity, silane concentration, and capillary-substrate separation. For both precursors, humidities of 45 ± 5% RH were used. Organotrichlorosilane precursor concentrations of 10 vol % were employed except when otherwise noted. The capillary was maintained at a distance of 30 μm above the substrate in all cases. Gradients were obtained by gradually decreasing the step time from several seconds to a few milliseconds. The step time was held constant as each line was plotted along the fast-scan (gradient width) direction and was gradually decreased along the slow-scan (gradient length) direction. The variations in step time along each gradient were determined separately for the octylsilane and cyanopropylsilane precursors, as described in Supporting Information. Gradients plotted using the *n*-octyltrichlorosilane were 7.5 mm in length and 3 mm in width, while those prepared using 3-cyanopropyltrichlorosilane were 9 mm in length and 5 mm in width. Larger area gradients were plotted in the case of the cyanopropylsilane to facilitate XPS data collection.

Figure 6.5 shows plots of film thickness and the associated WCAs for the *n*-octyltrichlorosilane and 3-cyanopropyltrichlorosilane gradients. Two replicate gradients were prepared and characterized to verify the reproducibility of vapor plotting for each precursor (see blue and red data points in **Figure 6.5**). Note that values are only shown for the gradient portion of each coated substrate. As expected, the film thickness and WCA values are greatest at the highly modified end of each gradient, with their values decreasing monotonically as a function of position along the gradient length.

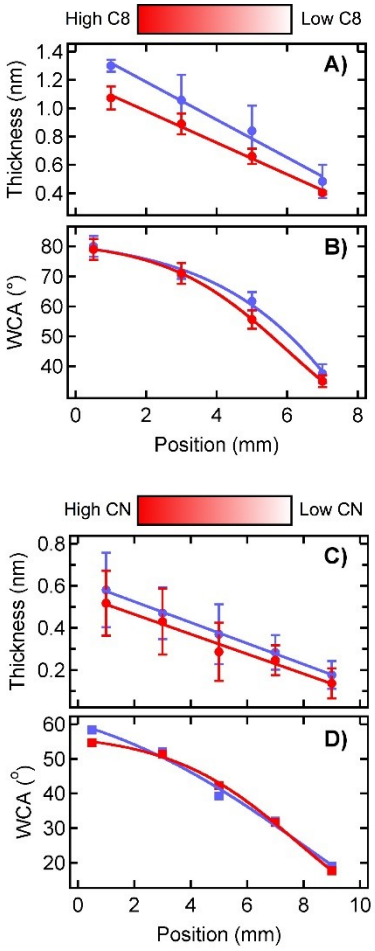

Figure 6.5 Ellipsometric film thickness and sessile drop WCA measured along the same gradient films plotted using **A)**, **B)** *n*-octyltrichlorosilane and **C)**, **D)** 3-cyanopropyltrichlorosilane precursors. The optimum plotting conditions identified above were used in preparing these films. The blue and red data points depict results from two replicate gradients in each case. All gradients shown here were plotted from 10 vol % silane in toluene. The solid lines have been added to better depict trends in the data. The error bars depict the 95% confidence intervals for n = 3 measurements in panels **A) - D)**.

Water droplets placed either at the very top of the gradient (i.e., the highly modified end) or along the two sides (i.e., the edges) of each gradient spontaneously moved away from the gradient towards unmodified substrate regions. In fact, the highly modified ends and sides (i.e., edges) of each gradient comprise gradients of their own, having very steep profiles over 1-2 mm distances (see below for a discussion of plotting resolution).

XPS mapping experiments were performed to confirm that the surfaces actually comprised gradients in the expected functional groups. XPS studies were performed only for the gradients derived from 3-cyanopropyltrichlorosilane, for which the N(1s) peak produced by the nitrile nitrogen could be detected. It was concluded that too much adventitious carbon was present to allow for mapping of the gradients prepared from *n*-octyltrichlorosilane.

Figure 6.6 plots the XPS results obtained from a gradient prepared using 100% 3-cyanopropyltrichlorsilane. **Figure 6.6A** shows the associated N(1s) XPS spectra as a function of position along the gradient. These data reveal the presence of two N(1s) peaks. The largest peak, centered at ~ 400 eV, decreased with position along the gradient, while the smaller peak, centered at ~ 402 eV, showed little variation with position. The former is attributed to the nitrile nitrogen[200, 207] while the latter is assigned to adventitious nitrogen contamination. In order to better assign the peak positions and to quantify the amount of nitrile nitrogen present, all spectra were fit to two Gaussian functions.[200] **Figure 6.6B** depicts the two components obtained by fitting the data acquired near the low nitrile end of the gradient. This analysis yielded a nitrile nitrogen binding energy of 400.2 ± 0.5 eV, with a binding energy of 402.3 ± 0.7 eV for the adventitious nitrogen.

Figure 6.6C shows a plot of the area (in arbitrary units) under the nitrile N(1s) peak (400.2 eV). This gradient was plotted so that its highly modified end was positioned at 5 mm, with the gradient extending to the 14 mm position. The gradient profile depicted in **Figure 6.6C** is different from that obtained by ellipsometry in **Figure 6.5C**. Although the causes of this difference are presently unknown, possible reasons are discussed further, below. It is noteworthy that the precursor reservoir was filled with 100 vol % cyanopropyltrichlorosilane during preparation of the film shown in **Figure 6.6C**, whereas 10 vol % silane was used for the one in **Figure 6.5C**. A

higher concentration of silane was required to produce a film that could be adequately characterized by XPS.

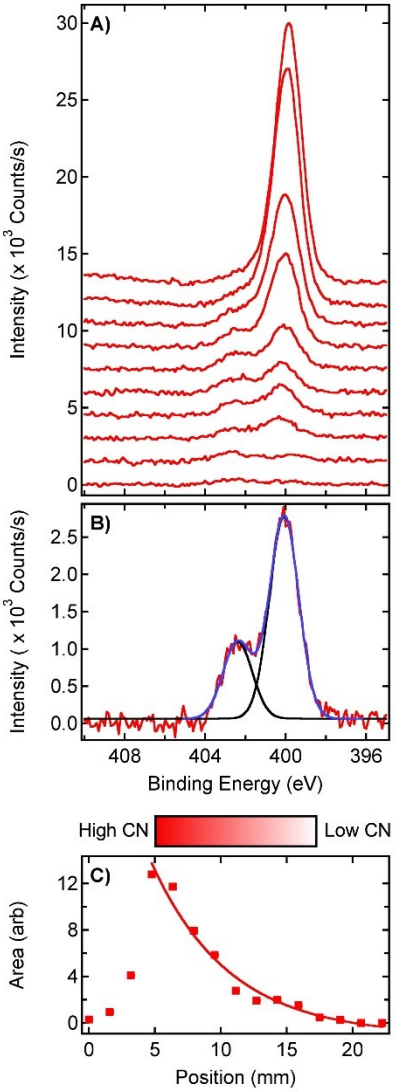

Figure 6.6 N(1s) XPS data for a vapor plotted 3-cyanopropyltrichlorosilane gradient. The reservoir was filled with 100% cyanopropylsilane during plotting. **A)** N(1s) spectra recorded along the gradient, starting from the highly modified end (top, 5 mm position). Each spectrum was fit to a two-component Gaussian. Each is shifted by 1500 counts/s from its neighbors to aid in viewing. **B)** N(1s) spectrum at the low cyanopropyl end of the gradient and its two-component fit (blue and black lines). **C)** Nitrile nitrogen (400.2 eV) peak area as a function of position along the gradient, which begins at ~ 5 mm and ends at ~ 14 mm. Error bars depict the error in peak area obtained by fitting each spectrum. The solid line and gradient model have been added to better depict the trend in the data. Data acquired by Dr**.** Anna Forzano, Dept. of Chemistry, Virginia Commonwealth University.

An initial quantitative estimate of the spatial resolution achievable by vapor-phase plotting may be obtained from the data shown in **Figure 6.6**. Positions between 0 and 4 mm correspond to the nominally unmodified silica base-layer-coated substrate. As expected, an abrupt increase in nitrile peak area was observed at ~ 5 mm, with a gradual decrease in nitrile coverage occurring from that point out to ~ 17 mm. The transition from unmodified base layer to fully modified surface at the high nitrile end of the gradient spanned ~ 4.8 mm (see **Figure 6.6C**). The spatial resolution was taken to be one half this distance, or ~ 2.4 mm. The finite resolution of vapor plotting also leads to the observed extension of the gradient beyond the predicted 14 mm position. The plotting resolution is expected to depend on capillary diameter and its distance from the substrate surface, see **Figure 6.3**. The millimeter resolution observed here represents only an initial demonstration of what might be achieved by vapor-phase plotting. Modifications to the method expected to improve the resolution are already under development. These modifications include implementation of capillaries having smaller inner diameters, and the development of methods to more quickly remove residual precursor from the capillary-substrate junction. It is expected that as much as a 100-fold improvement in resolution could be achieved in the future.

A primary advantage of vapor phase plotting is its ability to prepare gradients of arbitrary profile. For example, gradients that yield a linear decrease in WCA with position could be produced, as could gradients that instead exhibit a linear decrease in film thickness, as reflected by either the ellipsometry data or XPS peak area. Achieving the desired profile in a particular parameter requires careful calibration of the results obtained under a range of different plotting conditions (e.g., step time). An appropriate expression relating e.g., WCA to step time can then be developed and implemented during the plotting process to achieve the desired gradient profile. Indeed, the data shown in **Figure 6.5** were obtained from experiments in which this process was

tested. The exact functional form of the step time profiles employed along the slow-scan direction in preparation of the octylsilane and cyanopropylsilane gradients are shown in **Appendix D**. The curved (rather than linear) appearance of the WCA plots shown in **Figure 6.5** reflect the complexities of the calibration process. Similar problems lead to the curved appearance of the XPS data in **Figure 6.6C**. Obtaining a linear gradient here would require prior calibration of the XPS peak area with respect to step time. The different profiles observed in the ellipsometry and XPS data (compare **Figures 6.5C** and **6.6C**) for the cyanopropyl gradients may reflect the need for a different calibration at different precursor concentrations. However, it is most likely that the linear decrease in film thickness observed by ellipsometry is simply an artifact of enhanced averaging and reduced spatial resolution, as the ellipsometer employs a 2 mm x 5 mm elliptical spot of light.

6.4 Conclusions

The vapor-phase plotting of reactive organochlorosilanes was demonstrated for the first time. This method allows for patterned SAMs and chemical gradients to be prepared from organosilane precursors in a direct-write manner. The films thus prepared were characterized by spectroscopic ellipsometry, sessile drop water contact angle measurements, and by XPS mapping. The results demonstrated that monolayer-to-submonolayer films and gradients can readily be obtained. This study represents only an initial demonstration of the method. Work to improve the plotting resolution and to afford better control over gradient profiles is presently underway. A broader range of precursors will also be tested in the future. Vapor phase plotting affords a new route to producing patterned and chemically graded SAMs of arbitrary size and shape over pre-defined regions of larger substrates. The films obtained have myriad potential applications in controlling the motions and assembly of living cells, liquid droplets, vesicles, and nanoparticles. Vapor phase plotting may also be useful in the production of patterned coatings for lab-on-a-chip,

optical, and microelectronic devices as well as in the preparation of catalysts to explore organic transformations.

Chapter 7 - General Conclusions and Future Directions

7.1 General Conclusions

In this dissertation, the synthesis and use of a new Nile Red derivative incorporating a reactive aldehyde group (NR-Al) was reported (**Chapter 3**) for aldol reactions. Aldol reactions were studied at the ensemble (**Chapter 4**) and single molecule levels (**Chapter 5**) employing fluorescence spectroscopy methods.

In **Chapter 4**, the fluorescence shift in ensemble aldol reactions of NR-Al with acetone or acetophenone catalyzed by heterogeneous catalysts (MgO, and Mg-Zr-Cs/SiO_2) was followed *in situ*, while amorphous SiO_2 was employed as a control. A clear isoemissive point was observed in aldol reactions catalyzed by MgO, while a gradual fluorescence shift was observed in reactions catalyzed by Mg-Zr-Cs/SiO_2. The results of HPLC-MS experiments revealed that aldol product formation is catalyst-dependent. Commercial MgO, having strong basic sites (revealed from TPD of CO_2), catalyzed aldol addition (alcohol) product formation. The synthesized Mg-Zr-Cs/SiO_2 catalyst, incorporating both basic and acidic sites (revealed from TPD of CO_2 and NH_3), catalyzed the subsequent aldol condensation (olefin) product formation. As a control, SiO_2 did not catalyze aldol product formation due to insufficient catalytic sites.

In **Chapter 5**, SMS methods were employed to analyze spectral differences in the products of aldol reactions doped on thin catalyst films (Mg-Zr-Cs/TMOS), while NR- and NR-Al-doped films were employed as controls. As an initial test to check if aldol products display spectral differences compared to NR-Al, bulk fluorescence spectra in DMSO were taken and showed that alcohol products are shifted to the blue (~13 nm) compared to NR-Al, while olefin products are subtly shifted to the blue (~2-4 nm). In contrast, bulk spectra showed that NR-Al is shifted to the

red (~18 nm) compared to NR. It was then imperative to check if the spectral shifts exhibited by aldol products in bulk solution can be readily detected in a quantitative manner in SMS studies. This is important because it is likely that in the bulk mixture, fluorescence spectra from aldol products in solution and not on the catalyst surface is being probed. In this case, aldol product spectra may be altered by solvent effects from the ketone/DMSO mixture. On the contrary, the use of SMS methods allows for nanoscale environments to be probed in real time. In this case, distinct fluorescence spectra of single aldol product molecules on the catalyst surface may be elucidated providing important information on catalyst activity. Therefore, for the SMS studies described in this dissertation, some spectral information on the above molecules doped on catalyst films at nanomolar concentrations was assessed by two-color SMS imaging (572-646 nm, and 646-700 nm). While, the measured shift in E values was not statistically different between NR-Al and aldol products, the Navg of E was only statistically significant between NR-Al and the aldol addition product from the aldol reaction of NR-Al with acetone (at 90% C.I.). In contrast, the E value shift between NR and NR-Al was statistically significant (at 90% C.I.). A better method to quantify a spectral shift would be to employ confocal spectroscopy to measure the spectra of a single aldol product molecule and compared it to that of a single NR-Al molecule.

SMS studies were also employed to evaluate aldol reaction events by following individual NR-Al molecules doped on the catalyst film while exposed to the ketone reactant across several video frames. Films were exposed to acetone vapor in an otherwise dry nitrogen atmosphere and consecutive videos were taken for 1h around a ~0.5 cm radius from the center of the film. Preliminary SMT studies of these *in situ* aldol reactions revealed that 2.9% of spot trajectories had a real change in E based on the criteria for an aldol reaction event (spot trajectories >14 video frames long, and an abrupt E shift > 0.25 units, (signal noise is 0.1 units)). Trajectories showed a

red shift followed by a blue shift, which may be indicative of a different micropolarity environment being probed (by deposited acetone vapor) followed by an aldol reaction (blue shift).

This dissertation also introduced a new method based on vapor phase plotting (**Chapter 6**) to pattern chemical pads and gradients on glass surfaces. Plotting parameters such as ambient relative humidity, chemical concentration, raster scanning speed, and capillary-substrate separation were all found to influence surface coverage and plotting resolution. The optimized plotting parameters were employed for an initial demonstration to plot chemical pads and gradients of two organosilanes. With certain modifications to the current system, this vapor phase plotting method can likely be used in the production of patterned coatings or gradients for biological, optical, and microelectronic devices as well as in the preparation of catalysts for aldol reactions.

For example, it has been shown that cells efficiently interpret the positional information provided by biological gradients.[208, 209] The ability to control the chemical pattern/gradient on surfaces enables tuning the biological environment under study to better mimic biological processes or to aid in the development of materials used for biological applications. For example, Stefonek-Puccinelli et al. showed that quadratic and power law gradients of immobilized growth factors (GFs) consistently induced greater keratinocyte cell migration than linearly immobilized GF gradients.[209] The use of immobilized gradients of various GFs have also enabled investigations on their cooperative effects for tissue engineering applications (i.e. bone-cartilage interface in the knee).[210-212]

Another likely application for the vapor phase plotting method developed in this dissertation is for the production of organic thin films of small molecular semiconductors for molecular detection of low chemical concentrations[213] or to produce microelectronics.[214, 215] For example, Yilmaz et al. deposited a thin film of α,ω-diperfluorohexylquaterthiophene from the

vapor phase on a silicon surface and demonstrated that this superhydrophobic (150° WCA) semiconductor film enhanced the Raman signal up to 3.4 X 10^3 for the methylene blue probe molecule (10^{-5} M) without any additional plasmonic layer. This is an enhancement factor of ~100x to ~1000x compared to most inorganic semiconductor-based SERS platforms.[213] Regarding microelectronics, Forrest's and Yoo's research labs employed organic vapor jets to produce patterned thin films of light emitting diodes (OLED) and thin film transistors (OTFT) which can find applications in full-color displays and transistor circuits for consumer electronics.[214, 215]

Pertaining to employing the vapor plotter method developed in this dissertation for the preparation of patterned coatings or gradients for catalysis applications, future directions for the preparation of catalysts for aldol reactions will be discussed below.

7.2 Future Directions

The use of a new molecular probe allowed for aldol catalysis studies on heterogeneous catalysts and thin catalyst films. This dissertation provided clear evidence that the presence of basic and weakly acidic sites enhanced the subsequent aldol condensation reaction when Mg-Zr-Cs/SiO_2 was employed. Although the mechanism as to how the cooperative effect between the bifunctional catalytic sites occurs was not explored, possible reaction mechanisms were discussed according to the literature. Some new questions that were identified from the studies in this dissertation need to be addressed in the future as analytical methods evolve. Some studies that might be helpful to do are outlined below.

In **Chapter 4**, fluorescence spectra of ensemble aldol reactions catalyzed by heterogeneous catalysts were too complex to extract robust kinetic information from aldol condensation (olefin) product formation. High-resolution analytical techniques such as ^{1}H NMR will allow for this

information to be obtained. When employing this technique, characteristic proton peaks unique to NR-Al and aldol products (i.e. alcohol, and olefin) can be directly analyzed. In an aldol reaction, the proton peak from the aldehyde (in NR-Al) would decrease in time while proton peaks of the alcohol and C-C double bond in olefin would increase at a different rate. However, these experiments would need to be run *ex situ* due to the nature of the solid catalysts employed. Sample aliquots of aldol reactions would need to be removed from the reaction mixture, filtered, and run in the NMR, while keeping track of the time at which the aliquot was removed and prepared for analysis. In order to maintain the same reaction volume, the same aliquot amount from a concurrent aldol reaction (with the same catalyst) may be introduced into the reaction system. Alternatively, the use of single molecule spectroscopic methods will allow the microkinetics of catalysts to be studied *in situ*. Here, aldol reaction events occurring on a specified area at a fixed time can be counted to calculate reaction microkinetics, see below for work towards this vision.

In **Chapter 5**, possible aldol reaction events were observed by plotting the E values vs. fluorescent spot trajectories and detecting an abrupt change in E greater than the noise level (>0.1 units). Very few reactions events were observed over the course of 1h, indicating that more work needs to be done to optimize the catalyst film and perhaps the detection method. The actual Cs loading was about a third compared to the theoretical loading (2.1 ± 0.5 wt. % vs. 6 wt. %). Even though XPS showed that Cs was well dispersed, the density of active sites may be too low for effective catalysis. It is well known that desired concentrations of catalytically active sites are between 2-10% in heterogeneous inorganic catalysts.[42, 44, 45] Therefore, future studies should focus on systematically varying the loading of active sites and running *in situ* aldol reactions. By simply counting the number of aldol reaction events per area (μm^2) at a fixed time (sec), the microkinetics will provide important information for optimizing the catalyst films. Another option to increase

catalyst density is to employ SBA-15 instead of silica gel as it has a larger surface area.[41, 42, 152] Catalyst films of SBA-15 would not only allow for larger catalyst loading, but they would also introduce micropore and mesopore defects, which would allow further studies on how the catalytic activity is influenced by surface defects and diffusion barriers introduced by the micropores.

A question that was raised in *in situ* aldol reactions was whether the red to blue shift in the E value during acetone exposure, in an otherwise dry nitrogen atmosphere, was due to changes in the micropolarity environment of NR-Al (introduced by deposited acetone vapor) followed by an aldol reaction or if it was due to a retro-aldol reaction followed by an aldol reaction, where the red shift would indicate re-formation of NR-Al. In order to get more information, it would be helpful to have a concurrent program analyzing the E value in real time. In that case, when a red shift is observed, acetone vapor exposure would be stopped, solely leaving a dry nitrogen atmosphere (upon equilibration). If the E value returns to the value before the red shift was observed, it may indicate that the shift is due to the NR-Al chromophore probing acetone-induced changes in the micropolarity environment before the aldol reaction occurs (blue shift). Otherwise, if the E value remains red shifted, it would indicate that the product of the retro aldol reaction (i.e. NR-Al) or a more polar environment (silica) is being probed. However, this study may not be feasible due to the fast kinetics of aldol reaction (red to blue shift occurs in <30 sec).

In **Chapter 6**, vapor phase plotting of organosilanes was reported for the first time, and the plotting parameters were optimized for two organosilanes. The plotter employed a 1.5 mm ID glass capillary, which yielded a spatial resolution of ~2.4 mm (from XPS). One way to improve the plotting resolution (up to 80-fold) would be to employ capillaries with smaller inner diameters. For these experiments, capillaries with inner diameters between 30-100 μm can be used to plot organosilane chemical pads. The plotting resolution can be analyzed by XPS employing a smaller

X-ray spot size (30 μm). Capillaries with smaller inner diameters down to 10 μm may also be readily employed, however the lack of sensitive methods for determining spatial resolution would make it difficult to robustly measure the plotting resolution of such capillaries.

The increased plotting resolution would allow this method to be better employed in various applications including catalysis. A simple and time-efficient systematic study of how varying the catalytic site density within a thin film influences the kinetics of aldol conversion would be to plot chemical gradients on a single substrate. However, this method is limited to organic molecules with high vapor pressure that self-assemble onto the surface (i.e. glass). In this regard, aminosilanes are great candidates, where their basic functional group (i.e. NH_2) has been previously exploited for aldol catalysis studies.[37, 38, 216] However, its catalytic behavior towards aldol reactions has not yet been studied in thin films.

The vapor phase plotter introduced in this dissertation would be employed to plot amine chemical gradients at a predefined region where amine densities would gradually increase along the substrate. SMS methods such as the ones employed in this dissertation would be employed to image and track individual i*n situ* aldol reaction events. Reaction events would be counted per area (μm^2) at every 0.5-1 mm along the gradient (9 mm long) for a fixed period each time. These studies would allow for optimization of amine density for catalysis of aldol reactions in a systematic and time-efficient manner.

Unlike common vapor phase methods where the gradient profile is not easily controlled, vapor phase plotting would allow a larger region of the same aminosilane density to be plotted on the same substrate, therefore more reaction events can be analyzed in the same chemical environment. This would be achieved by simply employing the plotting parameters used to pattern the area with the optimized aminosilane density (from SMS studies of *in situ* aldol reactions on

the aminosilane gradient). For example, instead of the automated program (LabView) plotting the low amine end first (by fast raster scanning), it would be set to start plotting a mid-higher density of amine right away (by mid-slow raster scanning). This process would create a chemical pad (with adjustable length scales) in desired amine density and at virtually any location on the substrate without modifying surrounding regions.

The ease of control of the vapor plotting process can also be employed to study cooperative effects between basic and acidic catalyst sites in aldol reactions. For example, 3-aminopropyltrimethoxysilane (APTMOS) and 2-(4-chlorosulfonylphenyl)ethyl trichlorosilane can be employed as the base ($-NH_2$) and acid ($-SO_3H$) sources, where the chlorosulfonyl group may be protonated by Si-O-H groups on the silica or by exposure to water vapor. By employing these organosilanes, patterned chemical surfaces with varying functional groups and catalytic densities can be systematically formed at localized positions, opening a window for chemical and position-dependent catalysis studies.

Chapter 8 - References

1. Nielsen, A. T.; Houlihan, W. J., The Aldol Condensation. *In Organic Reactions, (Ed.).* **2011**.

2. Klein, D., *Organic Chemistry*. Second ed.; Johh Wiley and Sons: 2012.

3. Wender, P. A.; Schrier, A. J., Total Synthesis of Bryostatin 9. *Journal of the American Chemical Society* **2011,** *133* (24), 9228-9231.

4. DeLorbe, J. E.; Jabri, S. Y.; Mennen, S. M.; Overman, L. E.; Zhang, F.-L., Enantioselective Total Synthesis of (+)-Gliocladine C: Convergent Construction of Cyclotryptamine-Fused Polyoxopiperazines and a General Approach for Preparing Epidithiodioxopiperazines from Trioxopiperazine Precursors. *Journal of the American Chemical Society* **2011,** *133* (17), 6549-6552.

5. Egger, J.; Bretscher, P.; Freigang, S.; Kopf, M.; Carreira, E. M., Discovery of a Highly Potent Anti-inflammatory Epoxyisoprostane-Derived Lactone. *Journal of the American Chemical Society* **2014,** *136* (50), 17382-17385.

6. Shvartsbart, A.; Smith, A. B., The Daphniphyllum Alkaloids: Total Synthesis of (−)-Calyciphylline N. *Journal of the American Chemical Society* **2015,** *137* (10), 3510-3519.

7. Snyder, S. A.; Wespe, D. A.; von Hof, J. M., A Concise, Stereocontrolled Total Synthesis of Rippertenol. *Journal of the American Chemical Society* **2011,** *133* (23), 8850-8853.

8. Daub, M. E.; Prudhomme, J.; Le Roch, K.; Vanderwal, C. D., Synthesis and Potent Antimalarial Activity of Kalihinol B. *Journal of the American Chemical Society* **2015,** *137* (15), 4912-4915.

9. Silverman, R. B., *Organic Chemistry of Enzyme-Catalyzed Reactions, Revised Edition*. Elsevier Science: 2002.

10. Berg, J. M.; Tymoczko, J. L.; Stryer, L., The Citric Acid Cycle Oxidizes Two-Carbon Units. In *Biochemistry*, 5th ed.; W. H. Freeman: New York, 2002.

11. Berg, J. M.; Tymoczko; L., J.; Stryer, L., Glucose Can Be Synthesized from Noncarbohydrate Precursors. In *Biochemistry*, 5th ed.; W. H. Freeman: New York, 2002.

12. Berg; M., J.; Tymoczko, J. L.; Stryer, L., Glycolysis Is an Energy-Conversion Pathway in Many Organisms. In *Biochemistry*, 5th ed.; W. H. Freeman: New York, 2002.

13. Singh, P.; Anand, A.; Kumar, V., Recent developments in biological activities of chalcones: A mini review. *European Journal of Medicinal Chemistry* **2014,** *85*, 758-777.

14. Gurbuz, E. I.; Kunkes, E. L.; Dumesic, J. A., Dual-bed catalyst system for C-C coupling of biomass-derived oxygenated hydrocarbons to fuel-grade compounds. *Green Chemistry* **2010,** *12* (2), 223-227.

15. Klaus, W.; Hans-Jürgen, A., Industrial Organic Chemistry. 3rd, Completely Revised Edition ed.; Wiley: 2008; p. 481.

16. Kunkes, E. L.; Simonetti, D. A.; West, R. M.; Serrano-Ruiz, J. C.; Gärtner, C. A.; Dumesic, J. A., Catalytic Conversion of Biomass to Monofunctional Hydrocarbons and Targeted Liquid-Fuel Classes. *Science* **2008,** *322* (5900), 417.

17. Tedder, J. M.; Nechvatal, A.; Jubb, A. H., *Basic Organic Chemistry: Part 5 Industrial Products*. John Wiley and Sons: London, 1975.

18. Payne, L. S. Improvements in and Relating to Aldol Condensation. 1990.

19. Griesbeck, A. G.; Hinze, O.; Görner, H.; Huchel, U.; Kropf, C.; Sundermeier, U.; Gerke, T., Aromatic aldols and 1,5-diketones as optimized fragrance photocages. *Photochemical & Photobiological Sciences* **2012,** *11* (3), 587-592.

20. Hollis, G.; Davies, D. R.; Johnson, T. M.; Wade, L. G., *Organic Chemistry*. Pearson Prentice Hall: Upper Saddle River, NJ., 2006.

21. Smith, M. B., *March's Organic Chemistry: Reactions, Mechanisms, and Structure*. 7th ed.; New York, **2013**.

22. Weisssermel, K.; Arpe, H. J., *Industrial Organic Chemistry*. 3rd ed.; Wiley: New York, 1997.

23. Spivey, J. J.; Gogate, M. R., Pollution Prevention in Industrial Condensation Reactions. US EPA Grant: Research Triangle Institute, 1996.

24. King, F.; Kelly, G. J., Combined solid base/hydrogenation catalysts for industrial condensation reactions. *Catalysis Today* **2002,** *73* (1), 75-81.

25. Motokura, K.; Tada, M.; Iwasawa, Y., Acid–Base Bifunctional Catalytic Surfaces for Nucleophilic Addition Reactions. *Chemistry – An Asian Journal* **2008,** *3* (8-9), 1230-1236.

26. Brunelli, N. A.; Jones, C. W., Tuning acid–base cooperativity to create next generation silica-supported organocatalysts. *Journal of Catalysis* **2013,** *308*, 60-72.

27. Ye, R.; Zhao, J.; Yuan, B.; Liu, W.-C.; Rodrigues De Araujo, J.; Faucher, F. F.; Chang, M.; Deraedt, C. V.; Toste, F. D.; Somorjai, G. A., New Insights into Aldol Reactions of Methyl Isocyanoacetate Catalyzed by Heterogenized Homogeneous Catalysts. *Nano Letters* **2017,** *17* (1), 584-589.

28. Ponnuru, K.; Manayil, J. C.; Cho, H. J.; Fan, W.; Wilson, K.; Jentoft, F. C., Intraparticle Diffusional versus Site Effects on Reaction Pathways in Liquid-Phase Cross Aldol Reactions. *ChemPhysChem* **2018,** *19* (4), 386-401.

29. Bui, T. V.; Sooknoi, T.; Resasco, D. E., Simultaneous Upgrading of Furanics and Phenolics through Hydroxyalkylation/Aldol Condensation Reactions. *ChemSusChem* **2017,** *10* (7), 1631-1639.

30. Shen, W.; Tompsett, G. A.; Hammond, K. D.; Xing, R.; Dogan, F.; Grey, C. P.; Conner, W. C.; Auerbach, S. M.; Huber, G. W., Liquid phase aldol condensation reactions with MgO–ZrO2 and shape-selective nitrogen-substituted NaY. *Applied Catalysis A: General* **2011,** *392* (1), 57-68.

31. Zhang, G.; Hattori, H.; Tanabe, K., Aldol Addition of Acetone, Catalyzed by Solid Base Catalysts: Magnesium Oxide, Calcium Oxide, Strontium Oxide, Barium Oxide, Lanthanum (III) Oxide and Zirconium Oxide. *Applied Catalysis* **1988,** *36*, 189-197.

32. Izumi, Y.; Onaka, M., Liquid-phase organic reactions catalyzed by inorganic solid acids and bases. *Journal of Molecular Catalysis* **1992,** *74* (1), 35-42.

33. Corma, A.; Iborra, S., Optimization of Alkaline Earth Metal Oxide and Hydroxide Catalysts for Base-Catalyzed Reactions. In *Advances in Catalysis*, Gates, B. C.; Knözinger, H., Eds. Academic Press: 2006; Vol. 49, pp 239-302.

34. Climent, M. J.; Corma, A.; Fornés, V.; Guil-Lopez, R.; Iborra, S., Aldol Condensations on Solid Catalysts: A Cooperative Effect between Weak Acid and Base Sites. *Advanced Synthesis & Catalysis* **2002,** *344* (10), 1090-1096.

35. Li, B.; Yan, R. Y.; Wang, L.; Diao, Y. Y.; Li, Z. X.; Zhang, S. J., Synthesis of Methyl Methacrylate by Aldol Condensation of Methyl Propionate with Formaldehyde Over Acid-Base Bifunctional Catalysts. *Catalysis Letters* **2013,** *143* (8), 829-838.

36. Wang, Y. A.; Lang, X. W.; Zhao, G. Q.; Chen, H. H.; Fan, Y. W.; Yu, L. Q.; Ma, X. X.; Zhu, Z. R., Preparation of Cs-La-Sb/SiO2 catalyst and its performance for the synthesis of methyl acrylate by aldol condensation. *Rsc Advances* **2015,** *5* (41), 32826-32834.

37. Zeidan, R. K.; Hwang, S. J.; Davis, M. E., Multifunctional heterogeneous catalysts: SBA-15-containing primary amines and sulfonic acids. *Angewandte Chemie-International Edition* **2006,** *45* (38), 6332-6335.

38. Zeidan, R. K.; Davis, M. E., The effect of acid-base pairing on catalysis: An efficient acid-base functionalized catalyst for aldol condensation. *Journal of Catalysis* **2007,** *247* (2), 379-382.

39. Lewis, J. D.; Van de Vyver, S.; Román-Leshkov, Y., Acid–Base Pairs in Lewis Acidic Zeolites Promote Direct Aldol Reactions by Soft Enolization. *Angewandte Chemie International Edition* **2015,** *54* (34), 9835-9838.

40. Yadav, G. D.; Aduri, P., Aldol condensation of benzaldehyde with heptanal to jasminaldehyde over novel Mg-Al mixed oxide on hexagonal mesoporous silica. *Journal of Molecular Catalysis a-Chemical* **2012,** *355*, 142-154.

41. Yan, J. B.; Zhang, C. L.; Ning, C. L.; Tang, Y.; Zhang, Y.; Chen, L. L.; Gao, S.; Wang, Z. L.; Zhang, W. X., Vapor phase condensation of methyl acetate with formaldehyde to preparing methyl acrylate over cesium supported SBA-15 catalyst. *Journal of Industrial and Engineering Chemistry* **2015,** *25*, 344-351.

42. Li, B.; Yan, R. Y.; Wang, L.; Diao, Y. Y.; Li, Z. X.; Zhang, S. J., SBA-15 Supported Cesium Catalyst for Methyl Methacrylate Synthesis via Condensation of Methyl Propionate with Formaldehyde. *Industrial & Engineering Chemistry Research* **2014,** *53* (4), 1386-1394.

43. Bordiga, S.; Buzzoni, R.; Geobaldo, F.; Lamberti, C.; Giamello, E.; Zecchina, A.; Leofanti, G.; Petrini, G.; Tozzola, G.; Vlaic, G., Structure and Reactivity of Framework and Extraframework Iron in Fe-Silicalite as Investigated by Spectroscopic and Physicochemical Methods. *Journal of Catalysis* **1996,** *158* (2), 486-501.

44. Tai, J.; Davis, R. J., Synthesis of methacrylic acid by aldol condensation of propionic acid with formaldehyde over acid–base bifunctional catalysts. *Catalysis Today* **2007,** *123* (1), 42-49.

45. Jackson, S. D.; Johnson, D. W.; Scott, J. D.; Kelly, G. J.; Williams, B. P. Catalysts for the production of unsaturated acids or esters. 2003.

46. Copeland, G. T.; Miller, S. J., A Chemosensor-Based Approach to Catalyst Discovery in Solution and on Solid Support. *Journal of the American Chemical Society* **1999,** *121* (17), 4306-4307.

47. Jarvo, E. R.; Evans, C. A.; Copeland, G. T.; Miller, S. J., Fluorescence-Based Screening of Asymmetric Acylation Catalysts through Parallel Enantiomer Analysis. Identification of a Catalyst for Tertiary Alcohol Resolution. *The Journal of Organic Chemistry* **2001,** *66* (16), 5522-5527.

48. Lewis, W. G.; Magallon, F. G.; Fokin, V. V.; Finn, M. G., Discovery and Characterization of Catalysts for Azide−Alkyne Cycloaddition by Fluorescence Quenching. *Journal of the American Chemical Society* **2004,** *126* (30), 9152-9153.

49. List, B.; Barbas, C. F.; Lerner, R. A., Aldol sensors for the rapid generation of tunable fluorescence by antibody catalysis. *Proceedings of the National Academy of Sciences* **1998,** *95* (26), 15351.

50. Goddard, J.-P.; Reymond, J.-L., Recent advances in enzyme assays. *Trends in Biotechnology* **2004,** *22* (7), 363-370.

51. Tanaka, F., Development of protein, peptide, and small molecule catalysts using catalysis-based selection strategies. *The Chemical Record* **2005,** *5* (5), 276-285.

52. Ristanovic, Z.; Hofmann, J. P.; De Cremer, G.; Kubarev, A. V.; Rohnke, M.; Meirer, F.; Hofkens, J.; Roeffaers, M. B. J.; Weckhuysen, B. M., Quantitative 3D Fluorescence Imaging of Single Catalytic Turnovers Reveals Spatiotemporal Gradients in Reactivity of Zeolite H-ZSM-5 Crystals upon Steaming. *Journal of the American Chemical Society* **2015,** *137* (20), 6559-6568.

53. Ristanovic, Z.; Kubarev, A. V.; Hofkens, J.; Roeffaers, M. B. J.; Weckhuysen, B. M., Single Molecule Nanospectroscopy Visualizes Proton-Transfer Processes within a Zeolite Crystal. *Journal of the American Chemical Society* **2016,** *138* (41), 13586-13596.

54. Kumar, N.; Kalirai, S.; Wain, A. J.; Weckhuysen, B. M., Nanoscale Chemical Imaging of a Single Catalyst Particle with Tip-Enhanced Fluorescence Microscopy. *Chemcatchem* **2019,** *11* (1), 417-423.

55. Sklenak, S.; Dedecek, J.; Li, C. B.; Wichterlova, B.; Gabova, V.; Sierka, M.; Sauer, J., Aluminum siting in silicon-rich zeolite frameworks: A combined high-resolution Al-27 NMR spectroscopy and quantum mechanics/molecular mechanics study of ZSM-5. *Angewandte Chemie-International Edition* **2007,** *46* (38), 7286-7289.

56. van Bokhoven, J. A.; van der Eerden, A. M. J.; Koningsberger, D. C., Three-coordinate aluminum in zeolites observed with in situ X-ray absorption near-edge spectroscopy at the AlK-edge: Flexibility of aluminum coordinations in zeolites. *Journal of the American Chemical Society* **2003,** *125* (24), 7435-7442.

57. Hall, W. K.; Spiewak, B. E.; Cortright, R. D.; Dumesic, J. A.; Knozinger, H.; Pfeifer, H.; Kazansky, V. B.; Bond, G. C., Characterization of solid catalysts. In zeolites and catalysis: synthesis, reactions and applications. Wiley-VCH: Weinheim, 1997; pp 689-770.

58. Tanaka, F.; Mase, N.; Barbas, C. F., Design and use of fluorogenic aldehydes for monitoring the progress of aldehyde transformations. *Journal of the American Chemical Society* **2004,** *126* (12), 3692-3693.

59. Guo, H. M.; Tanaka, F., A Fluorogenic Aldehyde Bearing a 1,2,3-Triazole Moiety for Monitoring the Progress of Aldol Reactions. *Journal of Organic Chemistry* **2009,** *74* (6), 2417-2424.

60. Jung, H. S.; Pradhan, T.; Han, J. H.; Heo, K. J.; Lee, J. H.; Kang, C.; Kim, J. S., Molecular modulated cysteine-selective fluorescent probe. *Biomaterials* **2012,** *33* (33), 8495-8502.

61. Bongiovanni, M. N.; Godet, J.; Horrocks, M. H.; Tosatto, L.; Carr, A. R.; Wirthensohn, D. C.; Ranasinghe, R. T.; Lee, J.-E.; Ponjavic, A.; Fritz, J. V.; Dobson, C. M.; Klenerman, D.; Lee, S. F., Multi-dimensional super-resolution imaging enables surface hydrophobicity mapping. *Nature Communications* **2016,** *7* (1), 13544.

62. Dutta, A. K.; Kamada, K.; Ohta, K., Spectroscopic studies of nile red in organic solvents and polymers. *Journal of Photochemistry and Photobiology a-Chemistry* **1996,** *93* (1), 57-64.

63. Li, Z.; Kumarasinghe, R.; Collinson, M. M.; Higgins, D. A., Probing the Local Dielectric Constant of Plasmid DNA in Solution and Adsorbed on Chemically Graded Aminosilane Surfaces. *The Journal of Physical Chemistry B* **2018,** *122* (8), 2307-2313.

64. Giri, D.; Hanks, C. N.; Collinson, M. M.; Higgins, D. A., Single-Molecule Spectroscopic Imaging Studies of Polarity Gradients Prepared by Infusion-Withdrawal Dip-Coating. *The Journal of Physical Chemistry C* **2014,** *118* (12), 6423-6432.

65. Martin-Brown, S. A.; Fu, Y.; Saroja, G.; Collinson, M. M.; Higgins, D. A., Single-Molecule Studies of Diffusion by Oligomer-Bound Dyes in Organically Modified Sol−Gel-Derived Silicate Films. *Analytical Chemistry* **2005,** *77* (2), 486-494.

66. Cui, C.; Kirkeminde, A.; Kannan, B.; Collinson, M. M.; Higgins, D. A., Spatiotemporal Evolution of Fixed and Mobile Dopant Populations in Silica Thin-Film Gradients as Revealed by Single Molecule Tracking. *The Journal of Physical Chemistry C* **2011,** *115* (3), 728-735.

67. Morgenthaler, S.; Zink, C.; Spencer, N. D., Surface-Chemical and -Morphological Gradients. *Soft Matter* **2008,** *4*, 419-434.

68. Genzer, J., Surface-Bound Gradients for Studies of Soft Materials Behavior. *Annu. Rev. Mater. Res.* **2012,** *42*, 435-468.

69. Collinson, M. M.; Higgins, D. A., Organosilane Chemical Gradients: Progress, Properties, and Promise. *Langmuir* **2017,** *33*, 13719-13732.

70. Genzer, J.; Bhat, R. R., Surface-Bound Soft Matter Gradients. *Langmuir* **2008,** *24*, 2294-2317.

71. Inagi, S., Fabrication of gradient polymer surfaces using bipolar electrochemistry. *Polymer Journal* **2016,** *48* (1), 39-44.

72. Jayaraman, S.; Hillier, A. C., Construction and Reactivity Mapping of a Platinum Catalyst Gradient Using the Scanning Electrochemical Microscope. *Langmuir* **2001,** *17*, 7857-7864.

73. Fasolka, M. J.; Stafford, C. M.; Beers, K. L., Gradient and Microfluidic Library Approaches to Polymer Interfaces. In *Adv. Polym. Sci.*, Meier, M. A. R.; Webster, D. C., Eds. Springer-Verlag: Berlin, 2010; Vol. 225, pp 63-105.

74. Kannan, B.; Marin, M.; Shrestha, K.; Higgins, D. A.; Collinson, M. M., Continuous Stationary Phase Gradients for Planar Chromatographic Media. *J. Chromatog. A* **2011,** *1218*, 9406-9413.

75. Dewoolkar, V. C.; Kannan, B.; Ashraf, K. M.; Higgins, D. A.; Collinson, M. M., Amine-Phenyl Multi-Component Gradient Stationary Phases. *J. Chromatog. A* **2015,** *1410*, 190-199.

76. Elwing, H.; Welin, S.; Askendal, A.; Nilsson, U.; Lundström, I., A Wettability Gradient Method for Studies of Macromolecular Interactions at the Liquid/Solid Interface. *J. Colloid Interface Sci.* **1987,** *119*, 203-210.

77. Giri, D.; Li, Z.; Ashraf, K. M.; Collinson, M. M.; Higgins, D. A., Molecular Combing of Lambda-DNA using Self-Propelled Water Droplets on Wettability Gradient Surfaces. *ACS Appl. Mater. Interfaces* **2016,** *8*, 24265-24272.

78. Smith, J. T.; Elkin, J. T.; Reichert, W. M., Directed cell migration on fibronectin gradients: Effect of gradient slope. *Experimental Cell Research* **2006,** *312* (13), 2424-2432.

79. Singh, M.; Berkland, C.; Detamore, M. S., Strategies and Applications for Incorporating Physical and Chemical Signal Gradients in Tissue Engineering. *Tissue Engineering Part B-Reviews* **2008,** *14* (4), 341-366.

80. Ueda-Yukoshi, T.; Matsuda, T., Cellular Responses on a Wettability Gradient Surface with Continuous Variations in Surface Compositions of Carbonate and Hydroxyl Groups. *Langmuir* **1995,** *11* (10), 4135-4140.

81. Lee, J. H.; Kim, H. G.; Khang, G. S.; Lee, H. B.; Jhon, M. S., Characterization of wettability gradient surfaces prepared by corona discharge treatment. *Journal of Colloid and Interface Science* **1992,** *151* (2), 563-570.

82. Chaudhury, M. K.; Whitesides, G. M., How to Make Water Run Uphill. *Science* **1992,** *256*, 1539-1541.

83. Choi, S.-H.; Newby, B. Z., Micrometer-Scaled Gradient Surfaces Generated Using Contact Printing of Octadecyltrichlorosilane. *Langmuir* **2003,** *19*, 7427-7435.

84. Pardo, L.; Wilson, W. C.; Boland, T., Characterization of Patterned Self-Assembled Monolayers and Protein Arrays Generated by the Ink-Jet Method. *Langmuir* **2003,** *19*, 1462-1466.

85. Blondiaux, N.; Zürcher, S.; Liley, M.; Spencer, N. D., Fabrication of Multiscale Surface-Chemical Gradients by Means of Photocatalytic Lithography. *Langmuir* **2007,** *23*, 3489-3494.

86. Morgenthaler, S.; Lee, S.; Zürcher, S.; Spencer, N. D., A Simple, Reproducible Approach to the Preparation of Surface-Chemical Gradients. *Langmuir* **2003,** *19*, 10459-10462.

87. Ye, F.; Cui, C.; Kirkeminde, A.; Dong, D.; Collinson, M. M.; Higgins, D. A., Fluorescence Spectroscopy Studies of Silica Film Polarity Gradients Prepared by Infusion-Withdrawal Dip-Coating. *Chem. Mater.* **2010,** *22*, 2970-2977.

88. Cui, C.; Kirkeminde, A.; Kannan, B.; Collinson, M. M.; Higgins, D. A., Spatiotemporal Evolution of Fixed and Mobile Dopant Populations in Silica Thin-Film Gradients as Revealed by Single Molecule Tracking. *J. Phys. Chem. C* **2011,** *115*, 728-735.

89. Kannan, B.; Higgins, D. A.; Collinson, M. M., Aminoalkoxysilane Reactivity in Surface Amine Gradients Prepared by Controlled-Rate Infusion. *Langmuir* **2012,** *28*, 16091-16098.

90. Kannan, B.; Dong, D.; Higgins, D. A.; Collinson, M. M., Profile Control in Surface Amine Gradients Prepared by Controlled-Rate Infusion. *Langmuir* **2011,** *27*, 1867-1873.

91. Calvert, P., Inkjet Printing for Materials and Devices. *Chem. Mater.* **2001,** *13*, 3299-3305.

92. de Gans, B. J.; Duineveld, P. C.; Schubert, U. S., Inkjet Printing of Polymers: State of the Art and Future Developments. *Adv. Mater.* **2004,** *16* (3), 203-213.

93. Livage, J., Sol–gel synthesis of heterogeneous catalysts from aqueous solutions. *Catalysis Today* **1998,** *41* (1), 3-19.

94. Wrobleski, J. T.; Boudart, M., Preparation of solid catalysts: an appraisal. *Catalysis Today* **1992,** *15* (3), 349-360.

95. Livage, J.; Henry, M.; Sanchez, C., Sol-gel chemistry of transition metal oxides. *Progress in Solid State Chemistry* **1988,** *18* (4), 259-341.

96. Park, S.; Kim, C.-H.; Lee, W.-J.; Sung, S.; Yoon, M.-H., Sol-gel metal oxide dielectrics for all-solution-processed electronics. *Materials Science and Engineering: R: Reports* **2017,** *114*, 1-22.

97. Haber, J.; Block, J. H.; Delmon, B., Methods and Procedures for Catalyst Characterization. **2008,** *In Handbook of Heterogeneous Catalysis (eds G. Ertl, H. Knözinger, F. Schüth and J. Weitkamp).*

98. Austermann, R. L.; Denley, D. R.; Hart, D. W.; Himelfarb, P. B.; Irwin, R. M.; Narayana, M.; Szentirmay, R.; Tang, S. C.; Yeates, R. C., Catalyst characterization. *Analytical Chemistry* **1987,** *59* (12), 68-102.

99. Imelik, B.; Vedrine, J. C., *Catalyst Characterization: Physical Techniques for Solid Materials*. Springer US: 2013.

100. Che, M.; Vedrine, J. C., *Characterization of Solid Materials and Heterogeneous Catalysts: From Structure to Surface Reactivity*. Wiley: 2012.

101. Chatterjee, A. K., 8 - X-Ray Diffraction. In *Handbook of Analytical Techniques in Concrete Science and Technology*, Ramachandran, V. S.; Beaudoin, J. J., Eds. William Andrew Publishing: Norwich, NY, 2001; pp 275-332.

102. Inkson, B. J., 2 - Scanning electron microscopy (SEM) and transmission electron microscopy (TEM) for materials characterization. In *Materials Characterization Using Nondestructive Evaluation (NDE) Methods*, Hübschen, G.; Altpeter, I.; Tschuncky, R.; Herrmann, H.-G., Eds. Woodhead Publishing: 2016; pp 17-43.

103. Brunauer, S.; Emmett, P. H.; Teller, E., Adsorption of Gases in Multimolecular Layers. *Journal of the American Chemical Society* **1938,** *60* (2), 309-319.

104. Barrett, E. P.; Joyner, L. G.; Halenda, P. P., The Determination of Pore Volume and Area Distributions in Porous Substances-Computations from Nitrogen Isotherms. *Journal of the American Chemical Society* **1951,** *73* (1), 373-380.

105. Winge, R. K.; Peterson, V. J.; Fassel, V. A., Inductively Coupled Plasma-Atomic Emission Spectroscopy: Prominent Lines. *Applied Spectroscopy* **1979,** *33* (3), 206-219.

106. Fadley, C. S., Angle-resolved x-ray photoelectron spectroscopy. *Progress in Surface Science* **1984,** *16* (3), 275-388.

107. Falconer, J. L.; Schwarz, J. A., Temperature-Programmed Desorption and Reaction: Applications to Supported Catalysts. *Catalysis Reviews* **1983,** *25* (2), 141-227.

108. Ingle, J. D. J.; Crouch, S. T., *Spectrochemical Analysis*. Prentice-Hall, Inc.: Upper Saddle River, New York, 1988; p 337.

109. Moerner, W. E.; Fromm, D. P., Methods of single-molecule fluorescence spectroscopy and microscopy. *Review of Scientific Instruments* **2003,** *74* (8), 3597-3619.

110. Klar, T. A.; Hell, S. W., Subdiffraction resolution in far-field fluorescence microscopy. *Optics Letters* **1999,** *24* (14), 954-956.

111. Hell, S. W.; Wichmann, J., Breaking the diffraction resolution limit by stimulated emission: stimulated-emission-depletion fluorescence microscopy. *Optics Letters* **1994,** *19* (11), 780-782.

112. Abbe, E., Beiträge zur Theorie des Mikroskops und der mikroskopischen Wahrnehmung. *Archiv für Mikroskopische Anatomie* **1873,** *9* (1), 413-468.

113. Betzig, E.; Patterson, G. H.; Sougrat, R.; Lindwasser, O. W.; Olenych, S.; Bonifacino, J. S.; Davidson, M. W.; Lippincott-Schwartz, J.; Hess, H. F., Imaging intracellular fluorescent proteins at nanometer resolution. *Science (New York, N.Y.)* **2006,** *313* (5793), 1642-1645.

114. Rust, M. J.; Bates, M.; Zhuang, X., Sub-diffraction-limit imaging by stochastic optical reconstruction microscopy (STORM). *Nature Methods* **2006,** *3* (10), 793-796.

115. Thompson, R. E.; Larson, D. R.; Webb, W. W., Precise Nanometer Localization Analysis for Individual Fluorescent Probes. *Biophysical Journal* **2002,** *82* (5), 2775-2783.

116. Moerner, W. E., Microscopy beyond the diffraction limit using actively controlled single molecules. *Journal of Microscopy* **2012,** *246* (3), 213-220.

117. Bautista-Gomez, J.; Forzano, A. V.; Austin, J. M.; Collinson, M. M.; Higgins, D. A., Vapor-Phase Plotting of Organosilane Chemical Gradients. *Langmuir* **2018,** *34* (33), 9665-9672.

118. Hair, M. L.; Hertl, W., Reactions of Chlorosilanes with Silica Surfaces. *J. Phys. Chem.* **1969,** *73*, 2372-2378.

119. Stadler, A. F.; Melchior, T.; Mueller, M.; Sage, D.; Blu, T.; Unser, M., Low-Bond Axisymmetric Drop Shape Analysis for Surface Tension and Contact Angle Measurements of Sessile Drops. *Colloids Surf., A* **2010,** *364*, 72-81.

120. Ashraf, K. M.; Giri, D.; Wynne, K. J.; Higgins, D. A.; Collinson, M. M., Cooperative Effects in Aligned and Opposed Multi-Component Charge Gradients Containing Strongly Acidic, Weakly Acidic and Basic Functional Groups. *Langmuir* **2016,** *32*, 3836-3847.

121. Stambuli, J. P.; Stauffer, S. R.; Shaughnessy, K. H.; Hartwig, J. F., Screening of Homogeneous Catalysts by Fluorescence Resonance Energy Transfer. Identification of Catalysts for Room-Temperature Heck Reactions. *Journal of the American Chemical Society* **2001,** *123* (11), 2677-2678.

122. El-Rayyes, A. A.; Al-Betar, A.; Htun, T.; Klein, U. K. A., Fluorescence emission from rhodamine-B lactone adsorbed at solid catalysts. *Chemical Physics Letters* **2005,** *414* (4-6), 287-291.

123. Tang, Y.; Ma, Y.; Yin, J.; Lin, W., Strategies for designing organic fluorescent probes for biological imaging of reactive carbonyl species. *Chemical Society Reviews* **2019,** *48* (15), 4036-4048.

124. Tanaka, F.; Thayumanavan, R.; Mase, N.; Barbas, C. F., Rapid analysis of solvent effects on enamine formation by fluorescence: how might enzymes facilitate enamine chemistry with primary amines? *Tetrahedron Letters* **2004,** *45* (2), 325-328.

125. Das, A.; Anbu, N.; Sk, M.; Dhakshinamoorthy, A.; Biswas, S., A functionalized UiO-66 MOF for turn-on fluorescence sensing of superoxide in water and efficient catalysis for Knoevenagel condensation. *Dalton Transactions* **2019,** *48* (46), 17371-17380.

126. Katsuyama, I.; Chouthaiwale, P. V.; Akama, H.; Cui, H.-L.; Tanaka, F., Fluorogenic probes for aldol reactions: tuning of fluorescence using π-conjugation systems. *Tetrahedron Letters* **2014,** *55* (1), 74-78.

127. Jagtap, A. R.; Satam, V. S.; Rajule, R. N.; Kanetkar, V. R., Synthesis of highly fluorescent coumarinyl chalcones derived from 8-acetyl-1,4-diethyl-1,2,3,4-tetrahydro-7H-pyrano[2,3-g]quinoxalin-7-one and their spectral characteristics. *Dyes and Pigments* **2011,** *91* (1), 20-25.

128. Fu, Y.; Ye, F.; Sanders, W. G.; Collinson, M. M.; Higgins, D. A., Single Molecule Spectroscopy Studies of Diffusion in Mesoporous Silica Thin Films. *The Journal of Physical Chemistry B* **2006,** *110* (18), 9164-9170.

129. Hou, Y.; Bardo, A. M.; Martinez, C.; Higgins, D. A., Characterization of Molecular Scale Environments in Polymer Films by Single Molecule Spectroscopy. *The Journal of Physical Chemistry B* **2000,** *104* (2), 212-219.

130. Kumarasinghe, R.; Higgins, E. D.; Ito, T.; Higgins, D. A., Spectroscopic and Polarization-Dependent Single-Molecule Tracking Reveal the One-Dimensional Diffusion Pathways in Surfactant-Templated Mesoporous Silica. *The Journal of Physical Chemistry C* **2016,** *120* (1), 715-723.

131. Sarkar, N.; Das, K.; Nath, D. N.; Bhattacharyya, K., Twisted Charge-Transfer Process of Nile Red in Homogenous Solution and in Faujasite Zeolite. *Langmuir* **1994,** *10* (1), 326-329.

132. Guido, C. A.; Mennucci, B.; Jacquemin, D.; Adamo, C., Planar vs. twisted intramolecular charge transfer mechanism in Nile Red: new hints from theory. *Physical Chemistry Chemical Physics* **2010,** *12* (28), 8016-8023.

133. Martinez, V.; Henary, M., Nile Red and Nile Blue: Applications and Syntheses of Structural Analogues. *Chemistry-a European Journal* **2016,** *22* (39), 13764-13782.

134. Hess, C. M.; Riley, E. A.; Palos-Chávez, J.; Reid, P. J., Measuring the Spatial Distribution of Dielectric Constants in Polymers through Quasi-Single Molecule Microscopy. *The Journal of Physical Chemistry B* **2013,** *117* (23), 7106-7112.

135. Briggs, M. S. J.; Bruce, I.; Miller, J. N.; Moody, C. J.; Simmonds, A. C.; Swann, E., Synthesis of functionalised fluorescent dyes and their coupling to amines and amino acids. *Journal of the Chemical Society-Perkin Transactions 1* **1997,** (7), 1051-1058.

136. Wang, Y. X.; Zhou, C. S.; Wang, R. H., Copper-catalyzed hydroxylation of aryl halides: efficient synthesis of phenols, alkyl aryl ethers and benzofuran derivatives in neat water. *Green Chemistry* **2015,** *17* (7), 3910-3915.

137. Ramm, J. H.; Gartmann, N.; Bruhwiler, D., Direct synthesis and fluorescent imaging of bifunctionalized mesoporous iodopropyl-silica. *Journal of Colloid and Interface Science* **2010,** *345* (2), 200-205.

138. Lippert, S.; Baumann, W.; Thomke, K., Secondary Reactions of the Base-Catalyzed Aldol Condensation of Acetone. *Journal of Molecular Catalysis* **1991,** *69* (2), 199-214.

139. Shylesh, S.; Thiel, W. R., Bifunctional Acid–Base Cooperativity in Heterogeneous Catalytic Reactions: Advances in Silica Supported Organic Functional Groups. *ChemCatChem* **2011,** *3* (2), 278-287.

140. Hruby, S. L.; Shanks, B. H., Acid–base cooperativity in condensation reactions with functionalized mesoporous silica catalysts. *Journal of Catalysis* **2009,** *263* (1), 181-188.

141. Huh, S.; Chen, H.-T.; Wiench, J. W.; Pruski, M.; Lin, V. S. Y., Cooperative Catalysis by General Acid and Base Bifunctionalized Mesoporous Silica Nanospheres. *Angewandte Chemie International Edition* **2005,** *44* (12), 1826-1830.

142. Dumitriu, E.; Hulea, V.; Fechete, I.; Auroux, A.; Lacaze, J. F.; Guimon, C., The aldol condensation of lower aldehydes over MFI zeolites with different acidic properties. *Microporous and Mesoporous Materials* **2001,** *43* (3), 341-359.

143. Hattori, H., Heterogeneous Basic Catalysis. *Chemical Reviews* **1995,** *95* (3), 537-558.

144. Luo, M.-F.; Zhong, Y.-J.; Yuan, X.-X.; Zheng, X.-M., TPR and TPD studies of CuOCeO2 catalysts for low temperature CO oxidation. *Applied Catalysis A: General* **1997,** *162* (1), 121-131.

145. Ge, Q.; Huang, Y.; Qiu, F.; Li, S., Bifunctional catalysts for conversion of synthesis gas to dimethyl ether. *Applied Catalysis A: General* **1998,** *167* (1), 23-30.

146. Martins, G. V. A.; Berlier, G.; Bisio, C.; Coluccia, S.; Pastore, H. O.; Marchese, L., Quantification of Brønsted Acid Sites in Microporous Catalysts by a Combined FTIR and NH3-TPD Study. *The Journal of Physical Chemistry C* **2008,** *112* (18), 7193-7200.

147. Berteau, P.; Delmon, B., Modified Aluminas : Relationship between activity in 1-butanol dehydration and acidity measured by NH3 TPD. *Catalysis Today* **1989,** *5* (2), 121-137.

148. Tachikawa, T.; Majima, T., Single-Molecule, Single-Particle Approaches for Exploring the Structure and Kinetics of Nanocatalysts. *Langmuir* **2012,** *28* (24), 8933-8943.

149. Dutta, A. K.; Kamada, K.; Ohta, K., Langmuir-Blodgett films of nile red: A steady-state and time-resolved fluorescence study. *Chemical Physics Letters* **1996,** *258* (3-4), 369-375.

150. Barrett, E. P.; Joyner, L. G.; Halenda, P. P., The Determination of Pore Volume and Area Distributions in Porous Substances- Computations from Nitrogen Isotherms. *Journal of the American Chemical Society* **1951,** *73* (1), 373-380.

151. Sakthivel, K.; Notz, W.; Bui, T.; Barbas, C. F., Amino acid catalyzed direct asymmetric aldol reactions: A bioorganic approach to catalytic asymmetric carbon-carbon bond-forming reactions. *Journal of the American Chemical Society* **2001,** *123* (22), 5260-5267.

152. Wang, Y.; Yan, R.; Lv, Z.; Wang, H.; Wang, L.; Li, Z.; Zhang, S., Lanthanum and Cesium-Loaded SBA-15 Catalysts for MMA Synthesis by Aldol Condensation of Methyl Propionate and Formaldehyde. *Catalysis Letters* **2016,** *146* (9), 1808-1818.

153. Aramendía, M. A.; Benítez, J. A.; Borau, V.; Jiménez, C.; Marinas, J. M.; Ruiz, J. R.; Urbano, F., Study of MgO and Pt/MgO Systems by XRD, TPR, and 1H MAS NMR. *Langmuir* **1999,** *15* (4), 1192-1197.

154. Podgornov, E. A.; Prosvirin, I. P.; Bukhtiyarov, V. I., XPS, TPD and TPR studies of Cs-O complexes on silver: their role in ethylene epoxidation. *Journal of Molecular Catalysis a-Chemical* **2000,** *158* (1), 337-343.

155. van der Heide, P. A. W., Cesium-induced transient effects on the Si+ and Si- secondary ion emissions from Si and SiO2. *Surface Science* **2000,** *447* (1-3), 62-72.

156. Phillips, C. C.; Hughes, A. E.; Sibbett, W., Quantitative XPS Surface Chemical-Analysis and Direct Measurement of the Temporal Response-Times of Glass-Bonded NEA GAAS Transmission Photocathodes. *Journal of Physics D-Applied Physics* **1984,** *17* (8), 1713-1725.

157. Ebbinghaus, G.; Simon, A., Electronic-Structure of Rb, Cs and some of their Metallic Oxides Studied by Photoelectron-Spectroscopy. *Chemical Physics* **1979,** *43* (1), 117-133.

158. Beketov, G.; Heinrichs, B.; Pirard, J. P.; Chenakin, S.; Kruse, N., XPS structural characterization of Pd/SiO2 catalysts prepared by cogelation. *Applied Surface Science* **2013,** *287*, 293-298.

159. Arezzo, F.; Severini, E.; Zacchetti, N., An XPS Study of Diamond Films Grown on Differently Pretreated Silicon Substrates. *Surface and Interface Analysis* **1994,** *22* (1-12), 218-223.

160. Wu, M. Z.; Fu, Y.; Zhan, W. C.; Guo, Y. L.; Guo, Y.; Wang, Y. S.; Lu, G. Z., Catalytic Performance of MgO-Supported Co Catalyst for the Liquid Phase Oxidation of Cyclohexane with Molecular Oxygen. *Catalysts* **2017,** *7* (5).

161. Wang, X. Y.; Kang, Q.; Li, D., Low-temperature catalytic combustion of chlorobenzene over MnOx-CeO2 mixed oxide catalysts. *Catalysis Communications* **2008,** *9* (13), 2158-2162.

162. Yao, H. C.; Yao, Y. F. Y., Ceria in automotive exhaust catalysts: I. Oxygen storage. *Journal of Catalysis* **1984,** *86* (2), 254-265.

163. Faba, L.; Diaz, E.; Ordonez, S., Aqueous-phase furfural-acetone aldol condensation over basic mixed oxides. *Applied Catalysis B-Environmental* **2012,** *113*, 201-211.

164. Denmark, S. E.; Bui, T., Lewis base catalyzed enantioselective aldol addition of acetaldehyde-derived silyl enol ether to aldehydes. *Journal of Organic Chemistry* **2005,** *70* (24), 10190-10193.

165. Corma, A.; García, H., Lewis Acids: From Conventional Homogeneous to Green Homogeneous and Heterogeneous Catalysis. *Chemical Reviews* **2003,** *103* (11), 4307-4366.

166. Calvino-Casilda, V.; Martin-Aranda, R.; Sobczak, I.; Ziolek, M., Modification of acid–base properties of alkali metals containing catalysts by the application of various supports. *Applied Catalysis A: General* **2006,** *303* (1), 121-130.

167. Perrin, C. L.; Chang, K.-L., The Complete Mechanism of an Aldol Condensation. *The Journal of Organic Chemistry* **2016,** *81* (13), 5631-5635.

168. Niemantsverdriet, J. W., *Spectroscopy in Catalysis: An Introduction*. 3rd, Completely Revised and Enlarged Edition ed.; Wiley-VCH: Weinheim, 2007.

169. Thomas, J. M., Reflections on the value of electron microscopy in the study of heterogeneous catalysts. *Proceedings of the Royal Society a-Mathematical Physical and Engineering Sciences* **2017,** *473* (2197).

170. Frenken, J.; Groot, I., Live Observations of Catalysts Using High-Pressure Scanning Probe Microscopy. In *Operando Research in Heterogeneous Catalysis*, Frenken, J.; Groot, I., Eds. Springer International Publishing: Cham, 2017; pp 1-30.

171. Herbschleb, C. T.; van der Tuijn, P. C.; Roobol, S. B.; Navarro, V.; Bakker, J. W.; Liu, Q.; Stoltz, D.; Cañas-Ventura, M. E.; Verdoes, G.; van Spronsen, M. A.; Bergman, M.; Crama, L.; Taminiau, I.; Ofitserov, A.; van Baarle, G. J. C.; Frenken, J. W. M., The ReactorSTM: Atomically resolved scanning tunneling microscopy under high-pressure, high-temperature catalytic reaction conditions. *Review of Scientific Instruments* **2014,** *85* (8), 083703.

172. Grunwaldt, J.-D.; Schroer, C. G., Hard and soft X-ray microscopy and tomography in catalysis: bridging the different time and length scales. *Chemical Society Reviews* **2010,** *39* (12), 4741-4753.

173. Iwamoto, M.; Yoda, Y.; Yamazoe, N.; Seiyama, T., Study of metal oxide catalysts by temperature programmed desorption. 4. Oxygen adsorption on various metal oxides. *The Journal of Physical Chemistry* **1978,** *82* (24), 2564-2570.

174. Nguyen, L.; Tao, F. F.; Tang, Y.; Dou, J.; Bao, X.-J., Understanding Catalyst Surfaces during Catalysis through Near Ambient Pressure X-ray Photoelectron Spectroscopy. *Chemical Reviews* **2019,** *119* (12), 6822-6905.

175. Zhong, L. P.; Chen, D. K.; Zafeiratos, S., A mini review of in situ near-ambient pressure XPS studies on non-noble, late transition metal catalysts. *Catalysis Science & Technology* **2019,** *9* (15), 3851-3867.

176. De Cremer, G.; Sels, B. F.; De Vos, D. E.; Hofkens, J.; Roeffaers, M. B. J., Fluorescence micro(spectro)scopy as a tool to study catalytic materials in action. *Chemical Society Reviews* **2010,** *39* (12), 4703-4717.

177. Park, S.; Kang, W.; Kwon, Y.-D.; Shim, J.; Kim, S.; Kaang, B.-K.; Hohng, S., Superresolution fluorescence microscopy for 3D reconstruction of thick samples. *Molecular Brain* **2018,** *11* (1), 17.

178. Zhu, J.-L.; Xu, Z.; Yang, Y.; Xu, L., Small-molecule fluorescent probes for specific detection and imaging of chemical species inside lysosomes. *Chemical Communications* **2019,** *55* (47), 6629-6671.

179. Shashkova, S.; Leake, M. C., Single-molecule fluorescence microscopy review: shedding new light on old problems. *Bioscience Reports* **2017,** *37*.

180. Liu, Z.; Lavis, Luke D.; Betzig, E., Imaging Live-Cell Dynamics and Structure at the Single-Molecule Level. *Molecular Cell* **2015,** *58* (4), 644-659.

181. Imai, M.; Mihashi, A.; Imai, T.; Kimura, S.; Matsuzawa, T.; Yaoi, K.; Shibata, N.; Kakeshita, H.; Igarashi, K.; Kobayashi, Y.; Sugiyama, J., Selective fluorescence labeling: time-lapse enzyme visualization during sugarcane hydrolysis. *Journal of Wood Science* **2019,** *65* (1), 17.

182. Layek, A.; Van Loon, J.; Roeffaers, M. B. J.; Kubarev, A. V., Correlated super-resolution fluorescence and electron microscopy reveals the catalytically active nanorods within individual H-ZSM-22 zeolite particles. *Catalysis Science & Technology* **2019,** *9* (17), 4645-4650.

183. Roeffaers, M. B. J.; Sels, B. F.; Uji-i, H.; De Schryver, F. C.; Jacobs, P. A.; De Vos, D. E.; Hofkens, J., Spatially resolved observation of crystal-face-dependent catalysis by single turnover counting. *Nature* **2006,** *439* (7076), 572-575.

184. Xu, W.; Kong, J. S.; Yeh, Y.-T. E.; Chen, P., Single-molecule nanocatalysis reveals heterogeneous reaction pathways and catalytic dynamics. *Nature Materials* **2008,** *7* (12), 992-996.

185. Hendriks, F. C.; Mohammadian, S.; Ristanović, Z.; Kalirai, S.; Meirer, F.; Vogt, E. T. C.; Bruijnincx, P. C. A.; Gerritsen, H. C.; Weckhuysen, B. M., Integrated Transmission Electron and Single-Molecule Fluorescence Microscopy Correlates Reactivity with Ultrastructure in a Single Catalyst Particle. *Angewandte Chemie International Edition* **2018,** *57* (1), 257-261.

186. Ba, K. H. T.; Everett, T. A.; Ito, T.; Higgins, D. A., Trajectory angle determination in one dimensional single molecule tracking data by orthogonal regression analysis. *Physical Chemistry Chemical Physics* **2011,** *13* (5), 1827-1835.

187. Sbalzarini, I. F.; Koumoutsakos, P., Feature point tracking and trajectory analysis for video imaging in cell biology. *Journal of Structural Biology* **2005,** *151* (2), 182-195.

188. Solon, J.; Streicher, P.; Richter, R.; Brochard-Wyart, F.; Bassereau, P., Vesicles Surfing on a Lipid Bilayer: Self-Induced Haptotactic Motion. *Proc. Natl. Acad. Sci. USA* **2006,** *103*, 12382-12387.

189. Walder, R.; Honciuc, A.; Schwartz, D. K., Directed Nanoparticle Motion on an Interfacial Free Energy Gradient. *Langmuir* **2010,** *26*, 1501-1503.

190. Chang, T.; Rozkiewicz, D. I.; Ravoo, B. J.; Meijer, E. W.; Reinhoudt, D. N., Directional Movement of Dendritic Macromolecules on Gradient Surfaces. *Nano Lett.* **2007,** *7*, 978-980.

191. Smith, J. T.; Tomfohr, J. K.; Wells, M. C.; Beebe, T. P.; Kepler, T. B.; Reichert, W. M., Measurement of Cell Migration on Surface-Bound Fibronectin Gradients. *Langmuir* **2004,** *20*, 8279-8286.

192. Bhat, R. R.; Fischer, D. A.; Genzer, J., Fabricating Planar Nanoparticle Assemblies with Number Density Gradients. *Langmuir* **2002,** *18*, 5640-5643.

193. Liedberg, B.; Tengvall, P., Molecular Gradients of omega-Substituted Alkanethiols on Gold: Preparation and Characterization. *Langmuir* **1995,** *11*, 3821-3827.

194. Jeon, N. L.; Dertinger, K. W.; Chiu, D. T.; Choi, I. S.; Stroock, A. D.; Whitesides, G. M., Generation of Solution and Surface Gradients Using Microfluidic Systems. *Langmuir* **2000,** *16*, 8311-8316.

195. Terrill, R. H.; Balss, K. M.; Zhang, Y.; Bohn, P. W., Dynamic Monolayer Gradients: Active Spatiotemporal Control of Alkanethiol Coatings on Thin Gold Films. *J. Am. Chem. Soc.* **2000,** *122*, 988-989.

196. Biswas, S.; Pipe, K. P.; Shtein, M., Solvent-Free, Direct Printing of Organic Semiconductors in Atmosphere. *Appl. Phys. Lett.* **2010,** *96*, 263301.

197. Shtein, M.; Peumans, P.; Benziger, J. B.; Forrest, S. R., Direct, Mask- and Solvent-Free Printing of Molecular Organic Semiconductors. *Adv. Mater.* **2004,** *16*, 1615-1620.

198. Sun, Y.; Shtein, M.; Forrest, S. R., Direct Patterning of Organic Light-Emitting Devices by Organic-Vapor Jet Printing. *Appl. Phys. Lett.* **2005,** *86*, 113504.

199. McGraw, G. J.; Peters, D. L.; Forrest, S. R., Organic Vapor Jet Printing at Micrometer Resolution using Microfluidic Nozzle Arrays. *Appl. Phys. Lett.* **2011,** *98*, 013302.

200. Gulino, a.; Lupo, F.; Condorelli, G.; Fragala, M. E.; Amato, M. E.; Scarlata, G., Reversible Photoswitching of Stimuli-Responsive Si(100) Surfaces Engineered with an Assembled 1-cyano-1-phenyl-2-[4'-(10-undecenyloxy)phenyl]-ethylene monolayer. *J. Mater. Chem.* **2008,** *18*, 5011-5018.

201. Technologies, H. A. Tubing Chemical Compatibility. www.hollandapt.com/Documents/Ctrl_Hyperlink/Masterflex_Tubing_Chemical_Compatibility_uid172010827381.pdf.

202. Lide, D. R., *CRC Handbook of Chemistry and Physics*. CRC Press LLC: Boca Raton, 2001-2002.

203. Giri, D.; Ashraf, K. M.; Collinson, M. M.; Higgins, D. A., Single-Molecule Perspective on Mass Transport in Condensed Water Layers over Gradient Self-Assembled Monolayers. *J. Phys. Chem. C* **2015,** *119*, 9418-9428.

204. Silberzan, P.; Léger, L.; Ausserré, D.; Benattar, J. J., Silantion of Silica Surfaces. A New Method of Constructing Pure Mixed Monolayers. *Langmuir* **1991,** *7*, 1647-1651.

205. Angst, D. L.; Simmons, G. W., Moisture Absorption Characteristics of Organosiloxane Self-Assembled Monolayers. *Langmuir* **1991,** *7*, 2236-2242.

206. Schwartz, D. K., Mechanisms and Kinetics of Self-Assembled Monolayer Formation. *Annu. Rev. Phys. Chem.* **2001,** *52*, 107-137.

207. Tao, F.; Sim, W. S.; Xu, G. Q.; Qiao, M. H., Selective Binding of the Cyano Group in Acrylonitrile Adsorption on Si(100)-2X1. *J. Am. Chem. Soc.* **2001,** *123*, 9397-9403.

208. Barkefors, I.; Le Jan, S.; Jakobsson, L.; Hejll, E.; Carlson, G.; Johansson, H.; Jarvius, J.; Park, J. W.; Jeon, N. L.; Kreuger, J., Endothelial cell migration in stable gradients of vascular endothelial growth factor a and fibroblast growth factor 2 - Effects on chemotaxis and chemokinesis. *Journal of Biological Chemistry* **2008,** *283* (20), 13905-13912.

209. Stefonek-Puccinelli, T. J.; Masters, K. S., Co-Immobilization of Gradient-Patterned Growth Factors for Directed Cell Migration. *Annals of Biomedical Engineering* **2008,** *36* (12), 2121-2133.

210. Guo, X.; Liao, J.; Park, H.; Saraf, A.; Raphael, R. M.; Tabata, Y.; Kasper, F. K.; Mikos, A. G., Effects of TGF-beta 3 and preculture period of osteogenic cells on the chondrogenic differentiation of rabbit marrow mesenchymal stem cells encapsulated in a bilayered hydrogel composite. *Acta Biomaterialia* **2010,** *6* (8), 2920-2931.

211. Mohan, N.; Dormer, N. H.; Caldwell, K. L.; Key, V. H.; Berkland, C. J.; Detamore, M. S., Continuous Gradients of Material Composition and Growth Factors for Effective Regeneration of the Osteochondral Interface. *Tissue Engineering Part A* **2011,** *17* (21-22), 2845-2855.

212. Erisken, C.; Kalyon, D. M.; Wang, H. J.; Ornek-Ballanco, C.; Xu, J. H., Osteochondral Tissue Formation Through Adipose-Derived Stromal Cell Differentiation on Biomimetic Polycaprolactone Nanofibrous Scaffolds with Graded Insulin and Beta-Glycerophosphate Concentrations. *Tissue Engineering Part A* **2011,** *17* (9-10), 1239-1252.

213. Yilmaz, M.; Babur, E.; Ozdemir, M.; Gieseking, R. L.; Dede, Y.; Tamer, U.; Schatz, G. C.; Facchetti, A.; Usta, H.; Demirel, G., Nanostructured organic semiconductor films for

molecular detection with surface-enhanced Raman spectroscopy. *Nature Materials* **2017,** *16* (9), 918-924.

214. Shtein, M.; Peumans, P.; Benziger, J. B.; Forrest, S. R., Direct mask-free patterning of molecular organic semiconductors using organic vapor jet printing. *Journal of Applied Physics* **2004,** *96* (8), 4500-4507.

215. Yun, C.; Choi, J.; Kang, H. W.; Kim, M.; Moon, H.; Sung, H. J.; Yoo, S., Digital-Mode Organic Vapor-Jet Printing (D-OVJP): Advanced Jet-on-Demand Control of Organic Thin-Film Deposition. *Advanced Materials* **2012,** *24* (21), 2857-2862.

216. Lauwaert, J.; Moschetta, E. G.; Van Der Voort, P.; Thybaut, J. W.; Jones, C. W.; Marin, G. B., Spatial arrangement and acid strength effects on acid-base cooperatively catalyzed aldol condensation on aminosilica materials. *Journal of Catalysis* **2015,** *325*, 19-25.

217. Hagen, N.; Dereniak, E. L., Gaussian profile estimation in two dimensions. *Applied Optics* **2008,** *47* (36), 6842-6851.

Appendix A - Supplementary Information for Chapter 3

1. Characterization of 5-hydroxy-2-naphthoic acid (1):

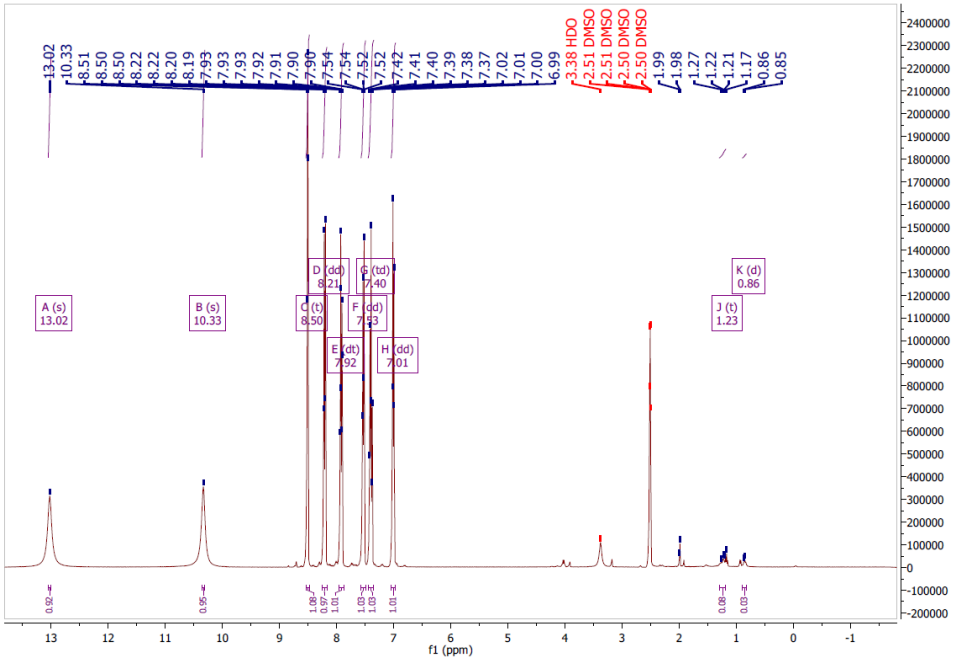

Figure A.1.1. [1]H NMR, 400 MHz, DMSO-d6.

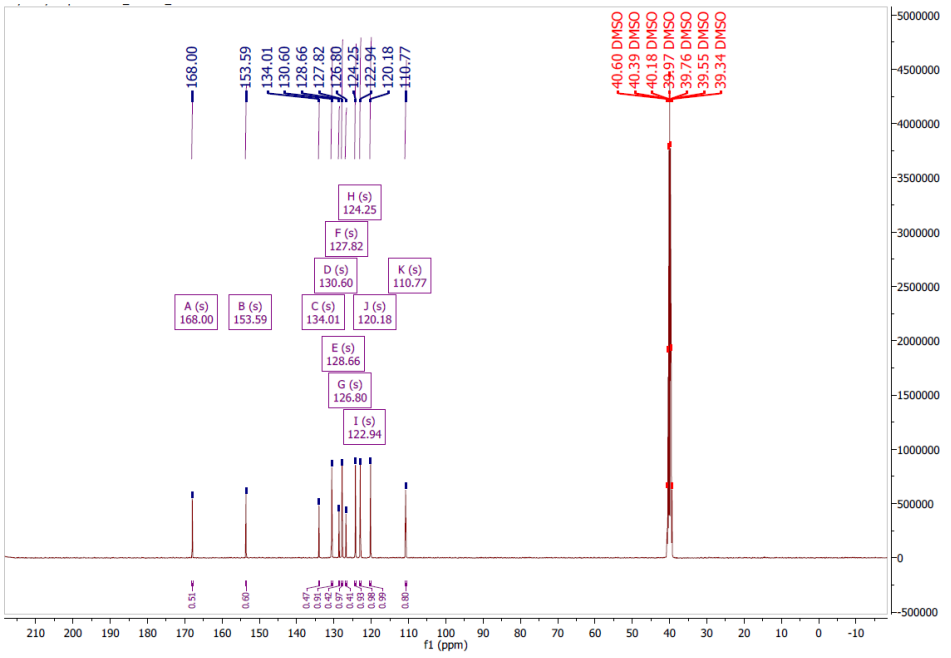

Figure A.1.2. [13]C NMR, 400 MHz, DMSO-d6.

2. Characterization of 5-hydroxy-2-naphthoic acid methyl ester (2):

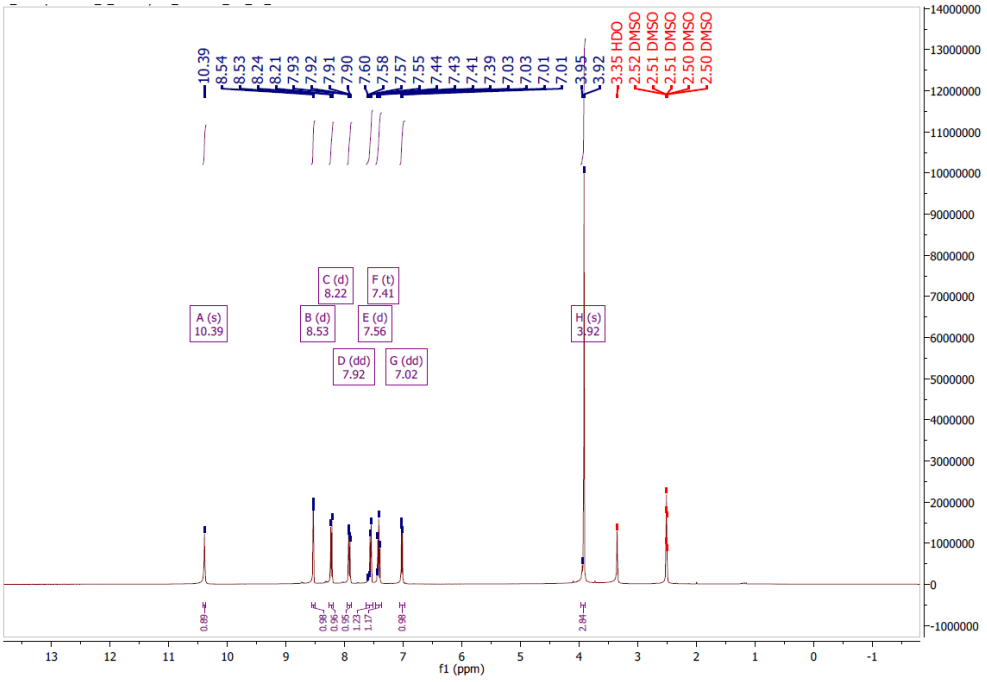

Figure A.2.1. ^{1}H NMR, 400 MHz, DMSO-d6.

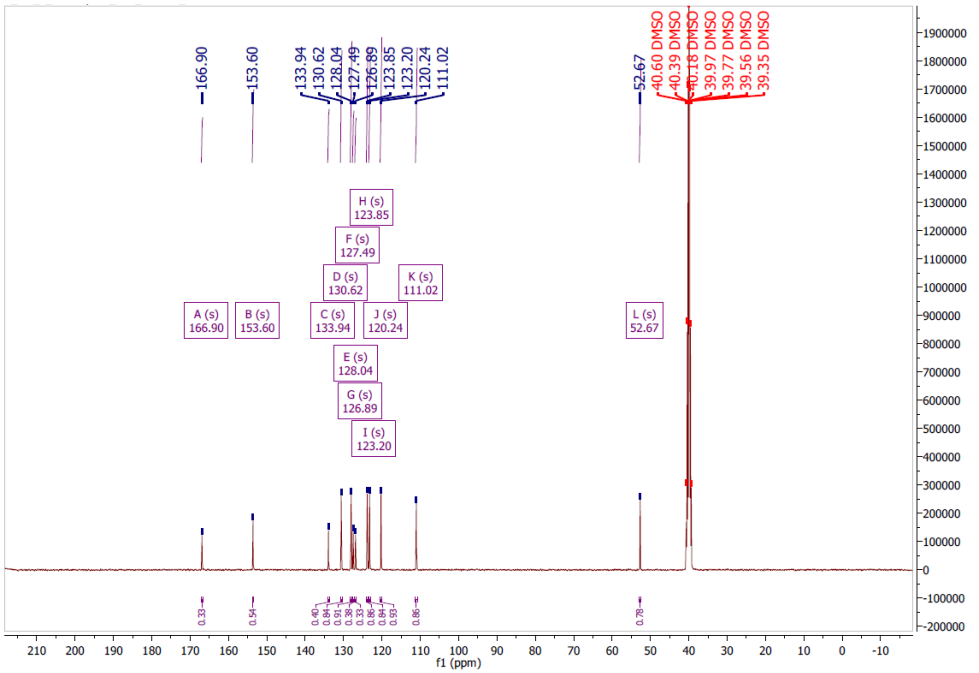

Figure A.2.2. ^{13}C NMR, 400 MHz, DMSO-d6.

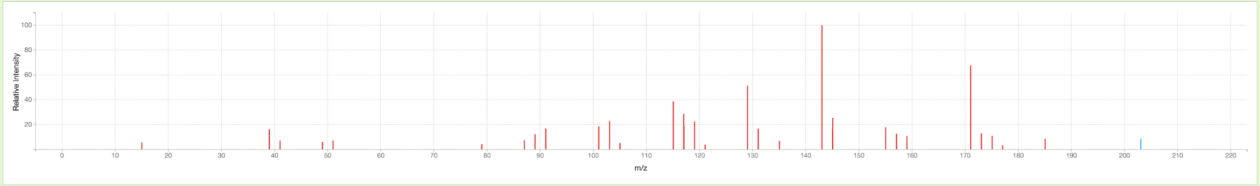

Figure A.2.3. EI-MS (M + 1): $C_{12}H_{11}O_3$: 203, $C_{12}H_9O_2$: 185, $C_{11}H_7O_2$: 171, $C_{10}H_7O$: 143. EI-MS was acquired in the Analytical Core Laboratory, University of Kansas Medical Center.

3. Characterization of 5-(Hydroxymethyl)naphthalen-2-ol (3):

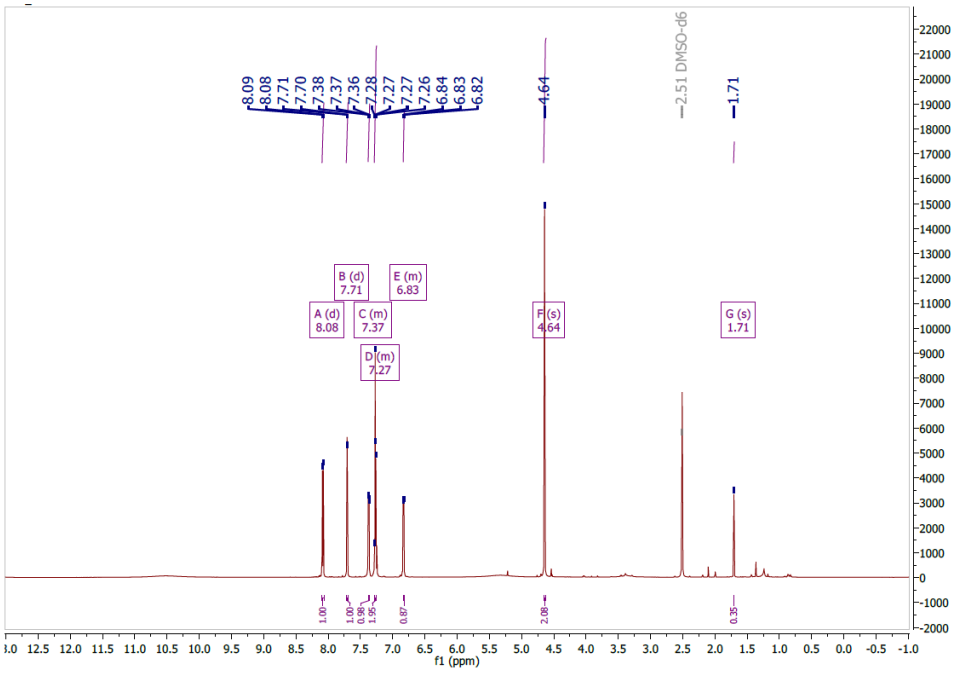

Figure A.3.1. ^{1}H NMR, 600 MHz, DMSO-d6.

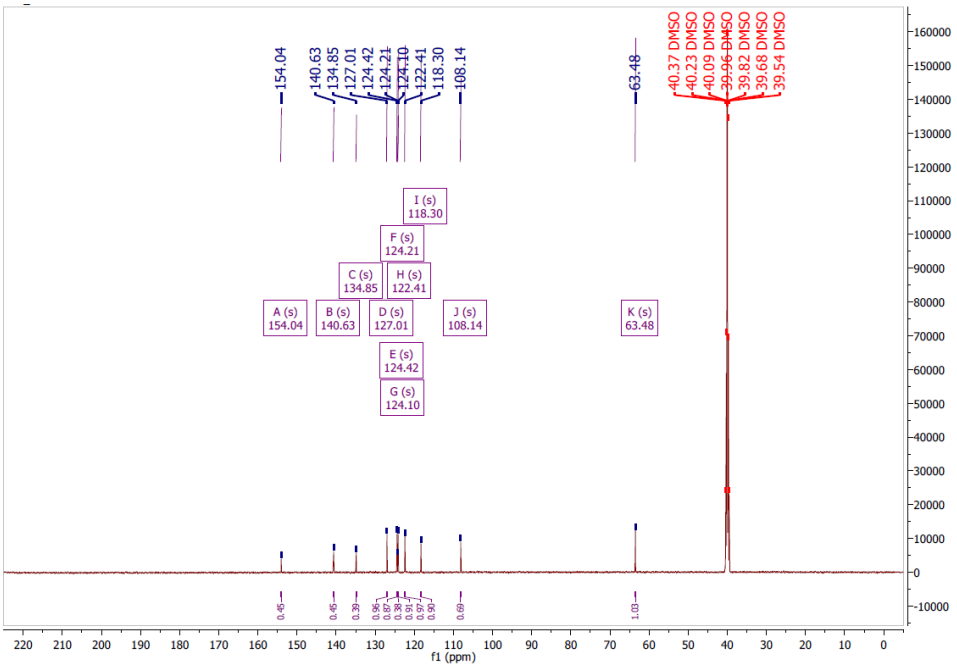

Figure A.3.2. ^{13}C NMR, 600 MHz, DMSO-d6.

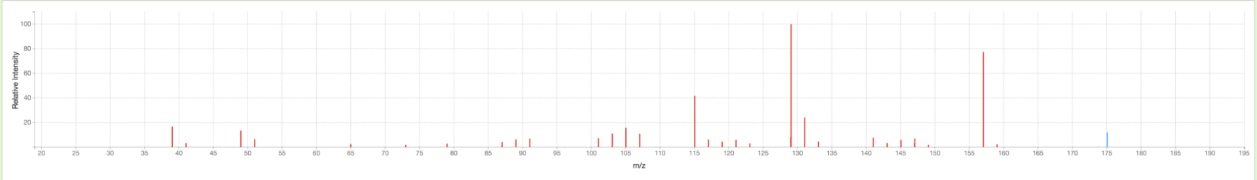

Figure A.3.3. EI-MS (M + 1): $C_{11}H_{11}O_2$: 175, $C_{11}H_9O$: 157, $C_{10}H_9O$: 145, $C_{10}H_9O$: 129.

EI-MS was acquired in the Analytical Core Laboratory, University of Kansas Medical Center.

4. Characterization of 5-Diethylamino-2-nitrosophenol (4):

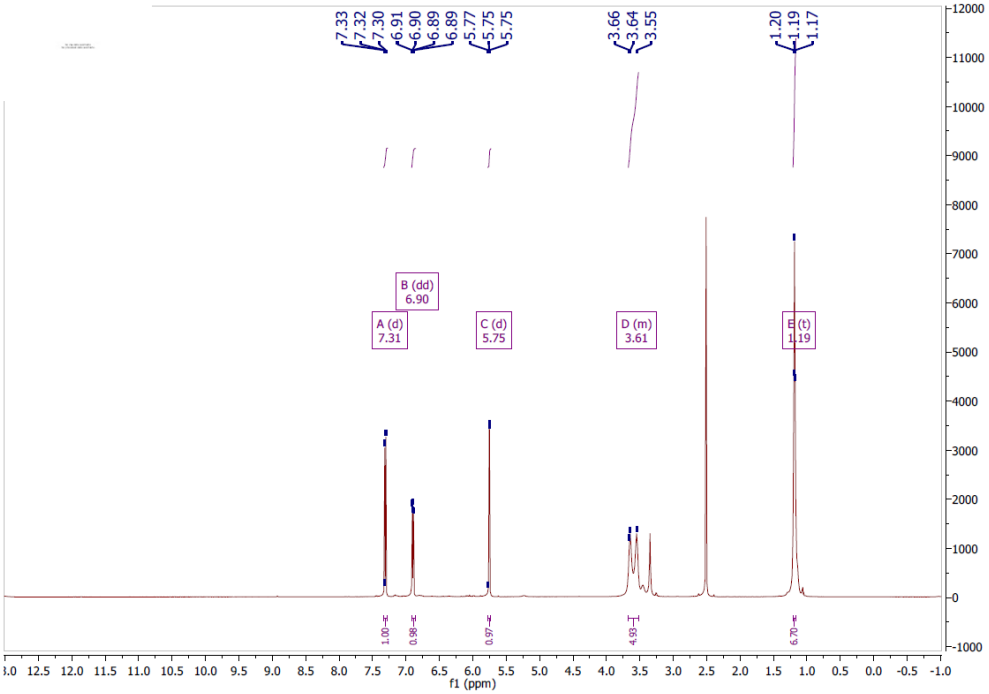

Figure A.4.1. [1]H NMR, 600 MHz, DMSO-d6.

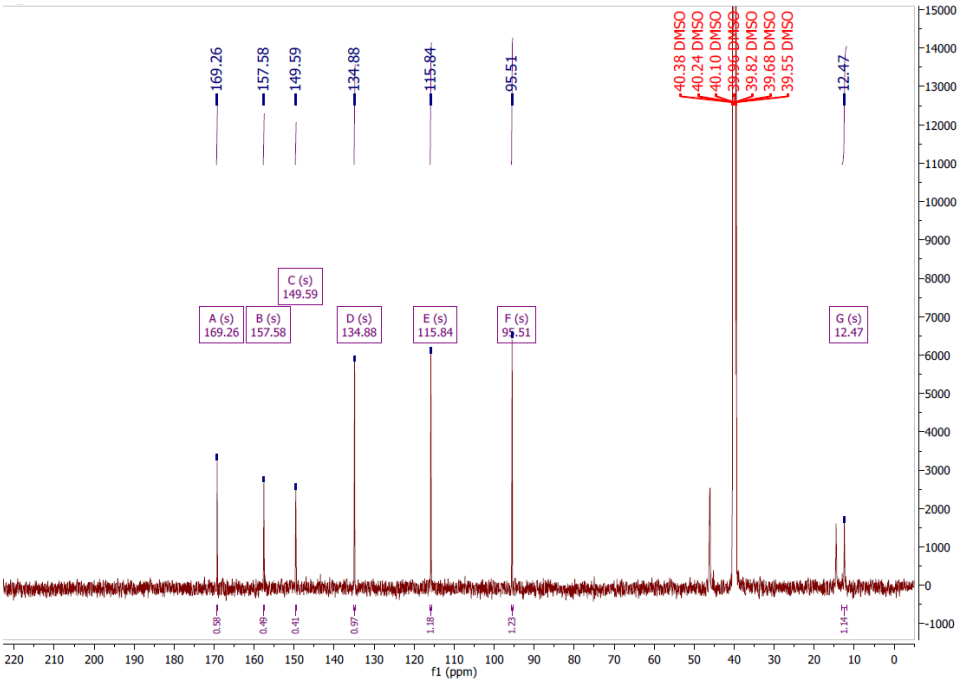

Figure A.4.2. [13]C NMR, 600 MHz, DMSO-d6.

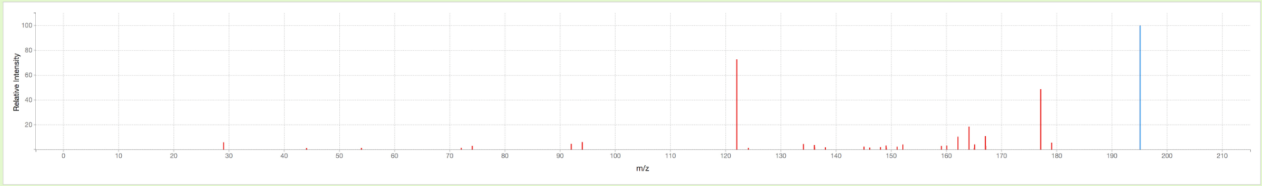

Figure A.4.3. EI-MS (M + 1): $C_{10}H_{15}O_2N_2$: 195, $C_{10}H_{13}ON_2$: 177, $C_{10}H_{15}O_2N_2$: 195, $C_6H_4O_2N_2$: 122. EI-MS was acquired in the Analytical Core Laboratory, University of Kansas Medical Center.

5. Characterization of 9-Diethylamino-2-hydroxymethyl-5H-benzo[a]phenoxazine-5-one (5):

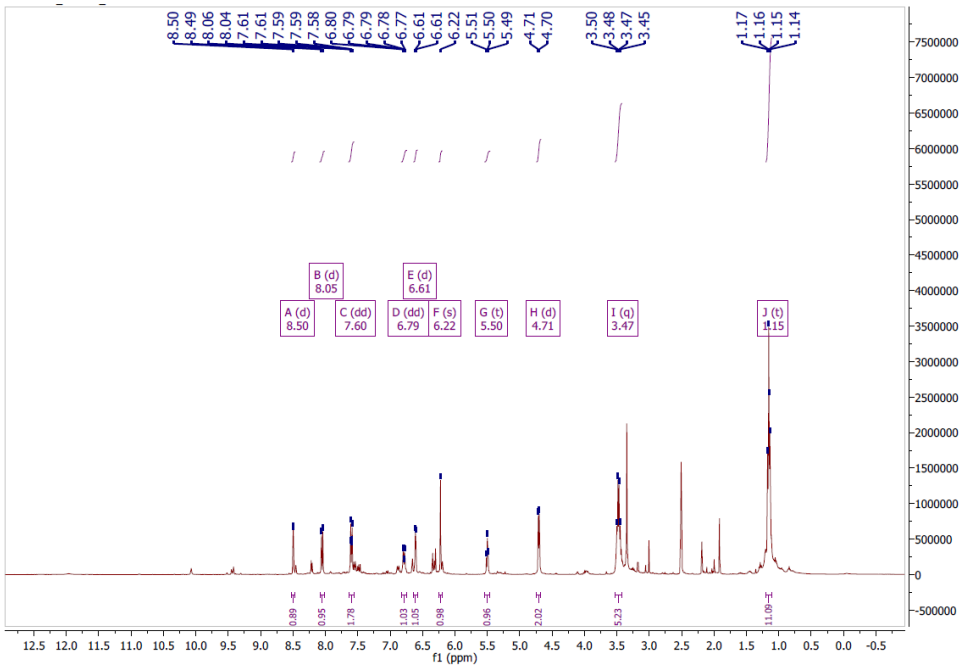

Figure A.5.1. ^{1}H NMR, 400 MHz, DMSO-d6.

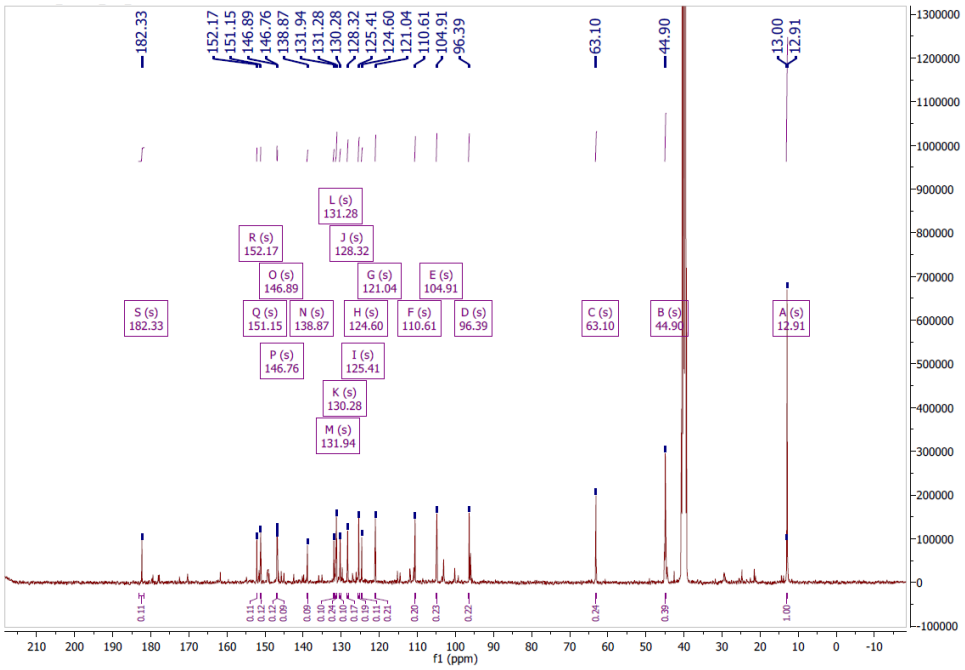

Figure A.5.2. ^{13}C NMR, 400 MHz, DMSO-d6**.**

6. Characterization of 9-Diethylamino-5-oxo-5H-benzo[a]phenoxazine-2-carboxaldehyde (6):

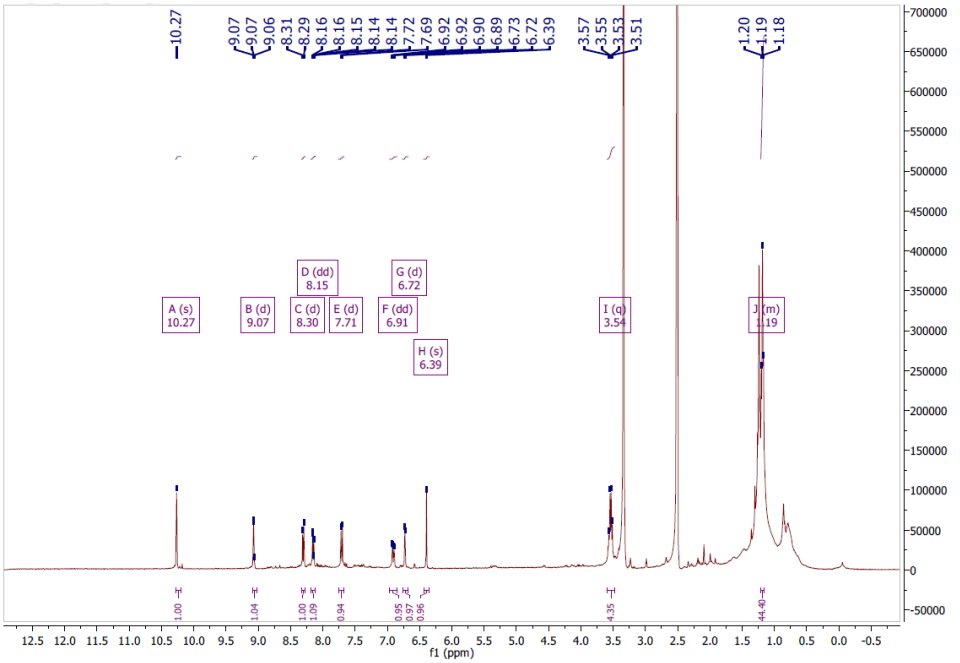

Figure A.6.1. ^{1}H NMR, 400 MHz, DMSO-d6.

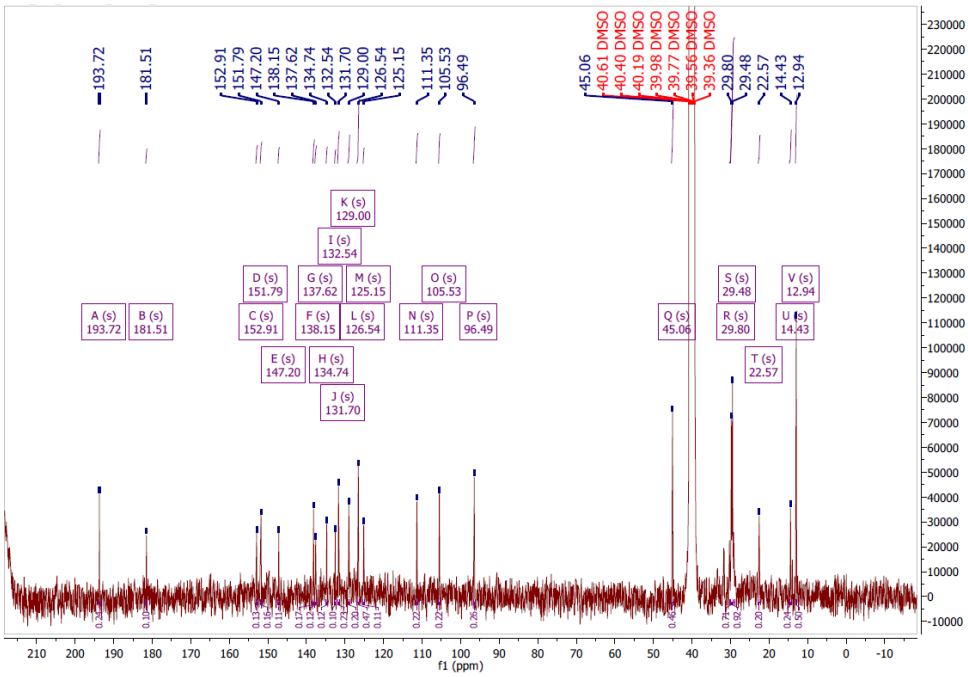

Figure A.6.2 ^{13}C NMR, 400 MHz, DMSO-d6.

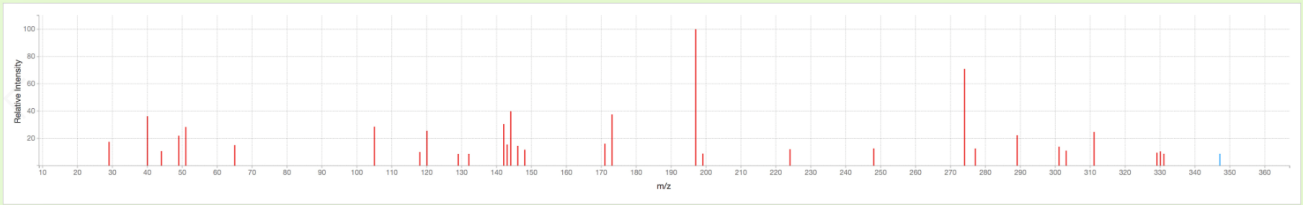

Figure A.6.3. EI-MS (M + 1): $C_{21}H_{19}O_3N_2$: 347, $C_{17}H_8O_3N$: 274, $C_{11}H_7O_2$: 171.

EI-MS was acquired in the Analytical Core Laboratory, University of Kansas Medical Center.

Appendix B - Supplementary Information for Chapter 4

1. Aldol Reaction Product Mass Spectra

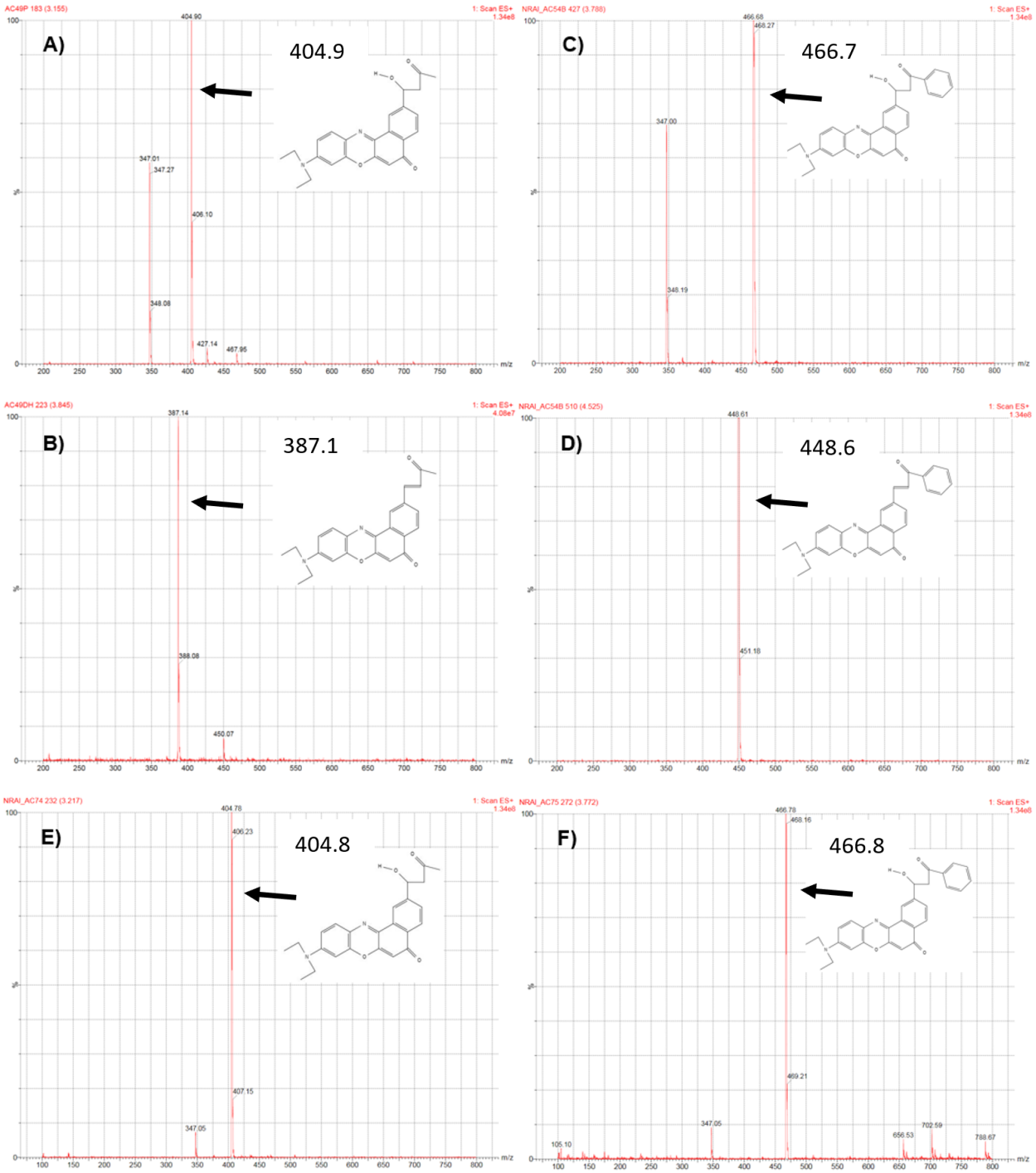

Figure B.1. HPLC-MS data from aldol addition and condensation products obtained after 3-day reactions of **(A, B)** NR-Al and acetone and **(C, D)** NR-Al with acetophenone using the Mg-Zr-

Cs/SiO_2 catalyst stirred at RT. **(A)** Aldol addition product, 405 amu; **(B)** aldol condensation product, 387 amu; **(C)** aldol addition product, 467 amu; **(D)** aldol condensation product, 449 amu. HPLC-MS of aldol addition products from 3-day reactions of **(E)** NR-Al with acetone and **(F)** NR-Al with acetophenone using the MgO catalyst stirred at RT. **(E)** aldol addition product, 405 amu; **(F)** aldol addition product, 467 amu. Note that the mass resolution in the instrument employed is ±1 amu.

2. Aldol Reaction Kinetics and Product Formation

Based on kinetic data from **Figure 4.5**, it appears the Mg-Zr-Cs/SiO_2 catalyzed reactions with acetone and acetophenone were nearly complete at ~ 2 h and ~ 24 h, respectively. Analytical HPLC was again used to confirm completeness of the reactions and to further characterize the products formed. These reactions were again run at high NR-Al concentration (1 mM) and under identical reaction conditions to those described in the main body. Product mixtures obtained from the acetone and acetophenone reactions after arbitrarily selected times of 8 h and 17 h, respectively, were compared to those obtained after 3 days. The HPLC data showed that the product mixtures obtained from the acetone reaction after 8h and 3 days were very similar. **Figures B.2.A, B** show these results. Only a small amount of NR-Al remained after 8h and that amount was significantly lower after 3 days. Greater conversion of the aldol addition product to the condensation product was also observed after 3 days. The acetophenone reaction was once again found to be much slower. **Figures B.2.C, D** show that after 17 h, a significant amount NR-Al remained in the mixture. After 3 days, more NR-Al had been converted to the aldol addition product. However, the longer reaction time did not appear to result in higher conversion of aldol addition product to the condensation product. It is uncertain why more condensation product was not found in the reaction mixture after 3 days.

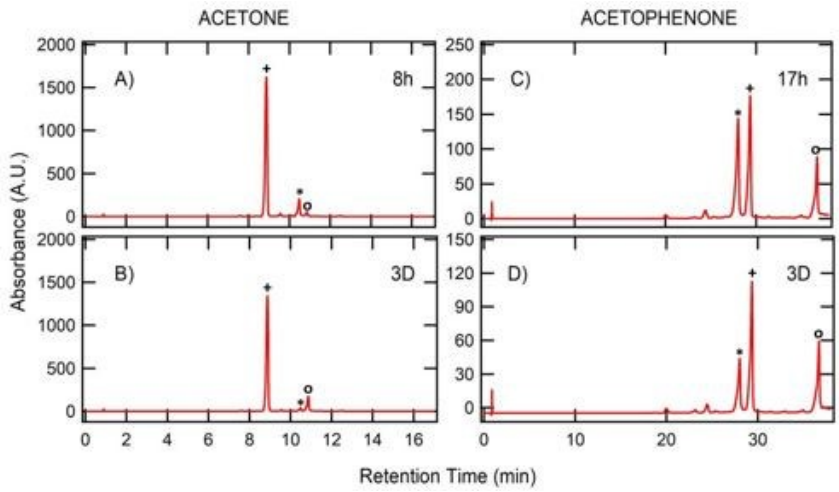

Figure B.2. HPLC chromatograms (575 nm absorbance) of aldol products for the NR-Al (1mM) reaction with acetone at 8h and 3D **(A, B)**, and acetophenone at 17h and 3D **(C, D)** in the presence of $MgZrCs/SiO_2$ at room temperature. The chromatograms show unreacted NR-Al **(*)**, the aldol addition product **(+)**, and the aldol condensation product **(o)**. Aldol reactions at 8h and 17h had a higher amount of unreacted NR-Al than 3-day reactions. The peak area ratio of unreacted NR-Al to aldol condensation product was ~ 4 and ~ 1.5 for acetone and acetophenone 8h and 17h reactions, respectively. While that peak area ratio was ~ 0.2 and ~ 0.8 for acetone and acetophenone 3-day reactions, respectively. Note that aldol reactions with acetone are faster than those with acetophenone due to the greater number of acidic hydrogens on the former. Allowing the NR-Al-acetone reaction to run for 3 days yielded a higher conversion of aldol addition to aldol condensation products, yielding peak area ratios of ~ 31 and ~ 7 in 8h and 3-day reactions, respectively. However, in the NR-Al-acetophenone reaction, the peak area ratio of aldol addition to aldol condensation products remained the same (~2) even after 3-days. Note that the peak area ratio of unreacted NR-Al to aldol addition product was lower after 3-days (i.e, ~ 0.5 compared to ~ 0.8 in the 17h reaction). For **A, B,** the mobile phase gradient comprised H_2O and acetonitrile mixtures at 0.800 mL/min flow rate with the following compositions: 0-10 min: 95-40% H_2O; 10-15 min: 40-20% H_2O; 15-17 min: 20% H_2O. For **C, D** the mobile phase compositions were: 0-35 min: 95-45% H_2O; 35-36 min: 45-20% H_2O; 36-38 min: 20% H_2O. A Thermo Scientific Hypersil GOLD C18 column (100 X 3 mm^2, 3 µm particle size) was employed.

3. Perylene Carboxaldehyde Fluorescence Spectra and Aldol Reaction

Results

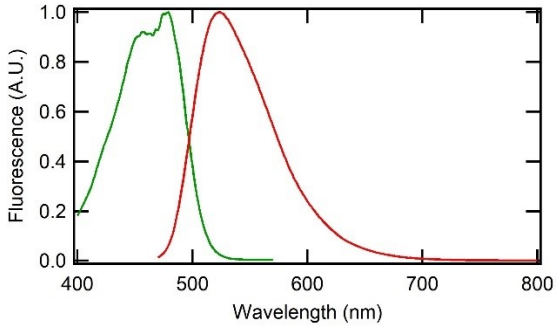

Figure B.3. Normalized fluorescence excitation (green) and emission (red) spectra of 1 μM 3-perylene carboxaldehyde in DMSO. The excitation spectrum is peaked at 476 nm with a vibronic band appearing at 456 nm respectively. The emission spectrum is centered at 523 nm.

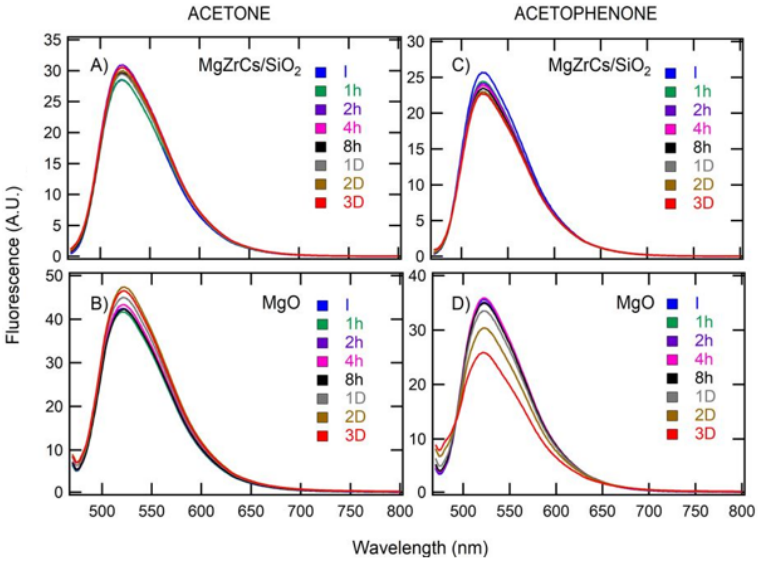

Figure B.4. A) -B) Fluorescence from 3-perylene carboxaldehyde as a function of time in the presence of the catalysts listed with acetone employed as the ketone. **C) - D)** Fluorescence from 3-perylene carboxaldehyde as a function of time in the presence of the catalysts listed with acetophenone employed as the ketone. The fluorescence was excited at 465 nm in each experiment. DMSO was employed as the solvent. All reactions were stirred at room temperature. Aldol reactions with acetone yielded nearly identical fluorescence spectra for the two different catalysts. While aldol reactions of the dye with acetophenone and MgO catalyst gave slightly different fluorescence spectra where it appeared that a very small shoulder peak centered at ~480 nm arose after 2 days. In contrast, very distinct fluorescence spectra were observed after only a few hours in aldol reactions with the reactive NR-Al dye and the same catalysts, **Figure 4.8**. ESI-MS confirmed the formation of aldol products under the above experimental conditions employing a higher concentration of 3-perylene carboxaldehyde (1 mM), see below.

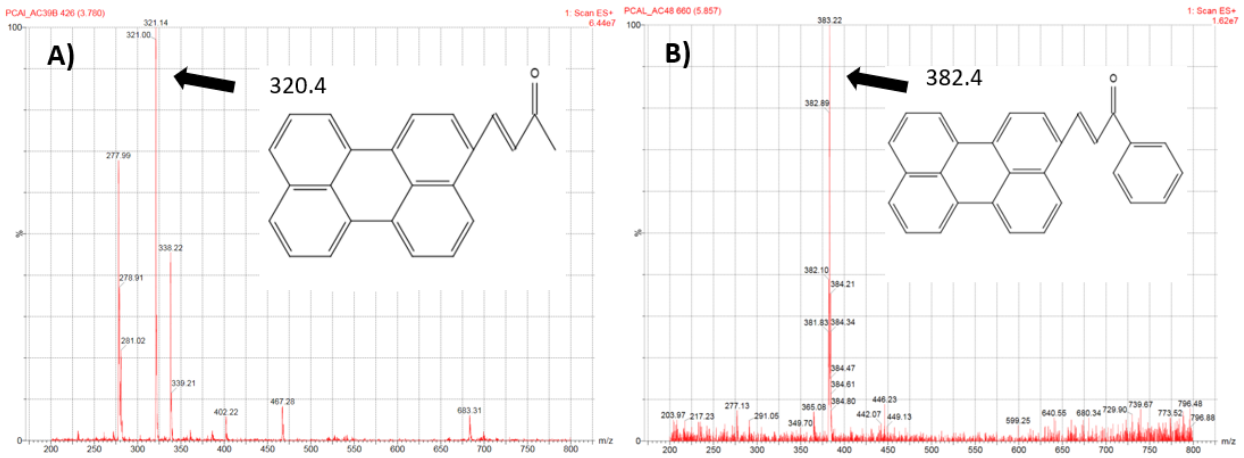

Figure B.5. HPLC-MS data from aldol products obtained after 3-day reactions of **(A)** NR-Al and acetone and **(B)** NR-Al with acetophenone using the Mg-Zr-Cs/SiO_2 catalyst stirred at RT. **(A)** Aldol condensation product, 321 amu; **(B)** aldol condensation product, 383 amu. Note that the mass resolution in the instrument employed is ±1 amu.

Appendix C - Supplementary Information for Chapter 5

1. Error Analysis for Single Molecule Emission Ratio Data

The individual fluorescent spots produced by single molecule emission are fit to Gaussian intensity profiles to determine the location of each molecule, the spot width, and its peak emission. The fits yield the signal amplitude for each spot and these values are used directly as I_{650} and I_{610} to calculate the emission ratio, E. The width of the spot is obtained as the standard deviation and is designated as ω, below. Accounting for shot noise in the photon signal and in the background, *b*, the variance in the fitted amplitude, σ^2_I , can be estimated for each channel as follows-[217]

$$\sigma^2_I \approx \frac{2(I+b)}{\pi\omega^2} \tag{C1}$$

Assuming the noise in the 650 nm and 610 nm channels is uncorrelated, the variance in E value is then estimated as-[217]

$$\sigma^2_E = \frac{4}{(I_{650}+ I_{610})^4} \left(I^2_{610}\sigma^2_{I_{610}} + I^2_{650}\sigma^2_{I_{650}}\right) \tag{C2}$$

The average background, *b*, was estimated to be 100 counts. The spot width, ω, is ~ 1.3 pixels. Given the above values, the standard deviation in E is estimated to be σ_E ~ 0.062, for nominal peak signals, I_{610} and I_{650} of ~ 100 and ~ 54 counts respectively. The 0.1 unit fluctuation in E during a spot trajectory is within the noise level, whereas an abrupt E shift of > 0.25 units is statistically significant.

Appendix D - Supplementary Information for Chapter 6

1. Predicting Stepper Motor Step Time

Vapor phase plotting potentially allows for the gradient profile to be preprogrammed by simply altering the raster scanning rate of the capillary above the substrate surface. As an initial demonstration of the process required, the step times needed to achieve a linear WCA gradient were calculated and employed in plotting the gradients shown in **Figure 6.5B, D**. In making this determination, the data shown in **Figure 6.2D** and in **Figure 6.4** were fit to double exponential functions. The step times expected to produce a linear WCA gradient were then numerically determined from the double exponential fit. The step time profiles are plotted in **Figures D.1.** and **D.2.** for *n*-octyltrichlorosilane and 3-cyanopropyltrichlorosilane, respectively.

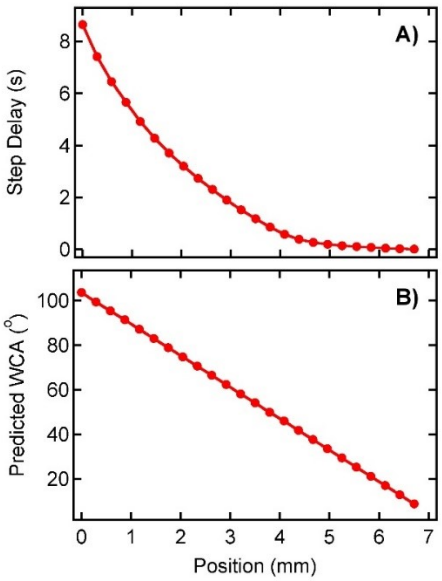

Figure D.1. A) Stepper motor step time predicted to yield an n-octyltrichlorosilane gradient exhibiting a linear decrease in the water contact angle. The step time was predicted from the data shown in Figure 6.2D. **B)** Linear water contact angle gradient predicted from the step times in A) and from the data shown in Figure 6.2D. The actual water contact angles obtained from gradients plotted using the step time profile in panel A are shown in Figure 6.5B. Reprinted with permission. **Copyright © 2018 American Chemical Society.**[117]

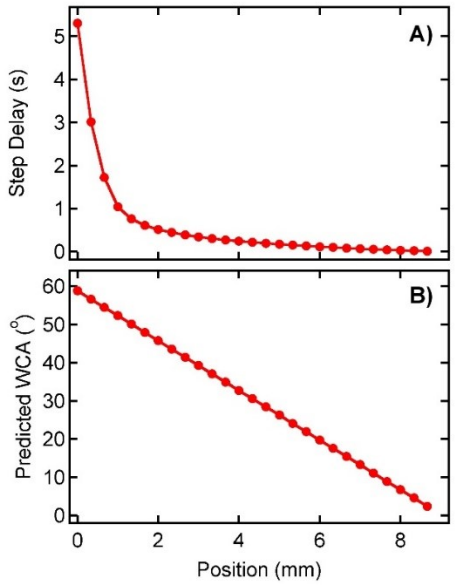

Figure D.2. A) Stepper motor step time predicted to yield a 3-cyanopropylsilane gradient exhibiting a linear decrease in the water contact angle. The step time was predicted from the data shown in Figure 6.4. **B)** Linear water contact angle gradient predicted from the step times in A) and from the data shown in Figure 6.4. The actual water contact angles obtained from a representative gradient are shown in Figure 6.5D. Reprinted with permission. **Copyright © 2018 American Chemical Society.**[117]